3D Printing Bioinspired, Bacteria-Embedded Ceramic Composites

Towards manufacturing shaped, strong, tough, and eco-friendly materials

W. J. (Wouter) van der Sluis

MSc Thesis

Delft University of Technology

TU Delft

SHAPING MATTER LAB

This page has been intentionally left blank.

3D Printing Bioinspired Bacteria-Embedded Ceramic Composites

Towards manufacturing shaped, strong, tough, and eco-friendly materials

Master of Science Thesis

by

W.J. (Wouter) van der Sluis

in partial fulfilment of the requirements for the degree of

Master of Science
in Aerospace Engineering

at the Delft University of Technology

To be defended on 28/11/2024 at 10:30

Student number:	4783476	
Date:	November 28, 2024	
Assessment committee:	Dr. K. (Kunal) Masania	Delft University of Technology
	Dr. ir. O.K. (Otto) Bergsma	Delft University of Technology
	Dr. B. (Baris) Kumru	Delft University of Technology
Daily supervisor:	Ir. I.H.M.S. (Ingo) Nettersheim	Delft University of Technology

This thesis is confidential and cannot be made public until 28 November 2025.

TU Delft

Delft University of Technology

Faculty of Aerospace Engineering
Department of Aerospace Structures and Materials

The undersigned hereby certify that they have read and recommend to the Faculty of Aerospace Engineering for acceptance the thesis entitled **3D Printing Bioinspired, Bacteria-Embedded Ceramic Composites: Towards manufacturing shaped, strong, tough, and eco-friendly materials** by **W. J. (Wouter) van der Sluis** in partial fulfilment of the requirements for the degree of **Master of Science** in **Aerospace Engineering**.

Dated: November 28, 2024

Chair of assessment committee:

Dr.ir. O.K. (Otto) Bergsma

Responsible supervisor:

Dr. K. (Kunal) Masania

Daily supervisor:

Ir. I.H.M.S. (Ingo) Nettersheim

External examiner:

Dr. B. (Baris) Kumru

This page has been intentionally left blank.

Preface

This thesis represents a significant milestone in my academic and personal journey. Over the past nine months, I have gained a deeper understanding of the complexities underlying seemingly simple phenomena and the practical challenges involved in studying them. One of the most valuable lessons I've learnt is that even well-planned efforts can encounter setbacks. Though often frustrating, these challenges are an integral part of the process, making research an equally humbling and empowering field. I hope this thesis contributes to future work in this field, providing insights and directions for others to build upon.

I want to express my sincere gratitude to Dr. Kunal Masania for entrusting me with this challenging and engaging research topic and for ensuring I received constructive guidance. My deepest thanks then go to Ingo Nettersheim, PhD candidate and my daily supervisor, whose feedback and support were invaluable to the progress of this project. Ingo, your practical advice and encouragement during difficult moments were greatly appreciated.

I am also grateful to Dr. Kathrin (Momo) Weiland and Dr. Sarah Schyck for their assistance with various practical challenges, from navigating lab equipment to troubleshooting experimental setups. Special thanks to Christopher Lankhof, PhD candidate, for his expertise in rheology, which was essential to my understanding of the results. I extend my appreciation to the entire Shaping Matter Lab team for fostering a collaborative and supportive research environment, and I wish you all success in your work.

Additionally, I would like to thank the Delft Aerospace Structures and Materials Laboratory staff for their technical support throughout my experiments, particularly Ing. Dave Ruijtenbeek, Dr. ir. Chantal de Zeeuw, Dr. Pietro Marchese, and Caitlin van den Hondel, B.Sc.

Finally, I am deeply thankful to my family, friends, fellow thesis students, and my girlfriend for their steadfast encouragement throughout this journey. Your support has been instrumental in helping me maintain focus and perspective during this process.

W.J. (Wouter) van der Sluis
Delft, November 28, 2024

This page has been intentionally left blank.

Abstract

Our reliance on synthetic structural materials has contributed extensively to environmental degradation, resource depletion, and pollution. The urgent need for sustainable alternatives has sparked interest in bio-based materials that align with Nature's cycles while maintaining high performance. However, finding such alternatives has remained challenging, especially for ceramics, which typically require high-temperature processes to achieve structural integrity. Yet Nature offers a promising blueprint: the nacreous layer, "mother of pearl", found in molluscan shells. Millions of years have allowed these invertebrates to evolve remarkable defect tolerance, achieving strength, stiffness, and toughness - a combination elusive in most conventional ceramics.

Despite extensive efforts, mimicking the intricate microstructure of nacre to achieve new, advanced materials remains challenging. Recent studies have leveraged the outstanding shaping freedom and microstructural control offered by additive manufacturing to provide new opportunities. However, these approaches continue to rely on sintering to improve mechanical properties, thereby undermining their ecological potential. The underlying printing process also remains largely unexplored. This thesis confronts both challenges by exploring a novel bacterial stiffening approach in direct ink writing using various material compositions. For the first time, mineral-depositing bacteria are incorporated into a ceramic-biopolymer suspension in an attempt to achieve sinter-like stiffening of the structure at reduced energy expenditure.

Direct ink writing ceramic-polymer bioinks is challenging due to the sensitivity of colloidal dispersions to changes in electrostatic and steric interactions, further complicated by strongly time-dependent rheology. These aspects hindered exploring the effects of biomineralisation on material performance. A 'printing window' is identified, beyond which bacteria-induced coagulation disrupts extrusion, establishing an essential constraint. Printability may be improved by controlling pH, performing more appropriate rheological experiments, and tuning rheology. Nutrient and bacterial content reduced material strength, meaning that any positive effect of biomineralisation must at least overcome this negative influence to provide a net benefit. Excessively high void content highlights the need to maximise compaction and solid content. Crucially, biomineralisation was achieved in preliminary tests, suggesting that the approach is fundamentally promising. These findings provide critical insights and guidelines for developing shaped, strong, tough, and sustainable ceramic materials, paving the way towards eco-friendly materials inspired and built by Nature.

Keywords
Ceramic composites; bioinspired; additive manufacturing; biomineralisation

This page has been intentionally left blank.

Table of Contents

List of Figures xi

List of Tables xiii

Nomenclature xv

1 Introduction 1
- 1.1 Addressing our planet's needs . . . 1
- 1.2 Mimicking Nature . . . 1
- 1.3 The structure of the molluscan shell . . . 2
- 1.4 Deformation and toughening mechanisms in nacre . . . 3
- 1.5 Fabrication methods for synthetic nacre . . . 4
- 1.6 To rule them all: additive manufacturing . . . 8
- 1.7 A key novel ingredient: bacteria . . . 9
- 1.8 Research definition . . . 10
- 1.9 Project planning . . . 11
- 1.10 Report overview . . . 11

2 Background 13
- 2.1 Microbially-induced calcite precipitation . . . 13
- 2.2 Rheology . . . 15
- 2.3 Shear-induced alignment in direct ink writing . . . 16
- 2.4 Design principles of artificial nacre . . . 17

3 Ink formulation 19
- 3.1 Preliminary: phyllosilicates and powdered chitosan . . . 19
- 3.2 Nacre-inspired: alumina and high molecular weight chitosan . . . 25
- 3.3 Nacre-inspired: alumina and cellulose nanofibres . . . 33
- 3.4 Chapter summary . . . 35

4 Material characterization 37
- 4.1 Methods . . . 37
- 4.2 Results and discussion . . . 42
- 4.3 Chapter summary . . . 51

5 Discussion 53
- 5.1 Overview of key findings . . . 53
- 5.2 Rheology and the differences across compositions . . . 54
- 5.3 Lack of platelet alignment . . . 58
- 5.4 Bacterial activity . . . 59
- 5.5 Key hypotheses . . . 60
- 5.6 Limitations of the current experimental approach . . . 60
- 5.7 Implications for theory and practice . . . 61

6 Conclusions and perspectives 63
- 6.1 Conclusions . . . 63
- 6.2 Recommendations for future work . . . 64
- 6.3 Significance of this work . . . 65

A Project & resource management **73**
B Literature search queries **77**
C Practical details and remarks **81**
D Raw rheology data **87**
E Flexural testing **101**

List of Figures

1.1 Schematic representation of the bivalve molluscan anatomy and the two stacking arrangements found in nacre . . . 2
1.2 Scanning electron micrographs of natural nacre showing conformal non-uniform thickness, surface asperities, and mineral bridges. . . . 3
1.3 Overview of the hierarchical structure and properties of nacre . . . 4
1.4 Schematic representation of freeze casting and resulting microstructure . . . 5
1.5 Schematic representation of hot-press assisted slip casting . . . 6
1.6 Schematic representation of layer-by-layer deposition and resulting microstructure . . . 7
1.7 Schematic representation of the paper-making approach of Walther et al. (2010a,b) . . . 7
1.8 Schematic representation of direct ink writing or 'robocasting' . . . 9

2.1 Schematic representation of microbially-induced calcite precipitation by *S. pasteurii* . . . 14
2.2 Scanning electron micrograph of typical MICP precipitate morphology . . . 14
2.3 Effects of pH on MICP as measured by Stocks-Fischer et al. (1999). . . . 15
2.4 Example rheological plots demonstrating shear thinning and measurement of stiffness and yield point . . . 16
2.5 Detailed illustration of the shear-induced alignment mechanism . . . 17
2.6 Filament micrographs and degrees of shear-induced alignment observed by Feilden et al. (2017) and comparison to theoretical velocity distribution . . . 18

3.1 Ultimaker UM2+ printer fitted with custom syringe extruder for preliminary printing experiments . . . 20
3.2 Sample preparation for rheological analysis. A small excess is added to the bottom plate **(a)**, after which the gap size is set **(b)**, and the excess is trimmed off **(c)**. The exposed surface is covered with silicone oil to reduce drying **(d)**. Scale bars are 20 mm (at the focal point). . . . 21
3.3 Print results of preliminary ink formulation . . . 22
3.4 Results of rheological measurements performed on the phyllosilicate/chitosan ink showing only partial satisfaction of the rheological requirements set by Feilden et al. (2017) despite demonstrating excellent printability. . . . 22
3.5 False-coloured SEM images of freeze-dried samples printed using preliminary ink formulation 23
3.6 False-coloured SEM images of a sample obtained from the second ink formulation containing 1 mL of concentrated inoculate . . . 24
3.7 Scanning electron micrographs depicting geometrical differences between platelet types. . . . 25
3.8 Creality Ender-3 V2 with custom print module for direct ink writing. Build plate is 235 × 235 mm. 26
3.9 Model of raster print as generated using the FullControl package showing primer or 'lead-in' lines followed by a cubic grid structure. . . . 26
3.10 Raster print result for Al_2O_3/HMWC mixture using the same volume-wise composition as the PS/PC mixture, showing significantly reduced print fidelity. 50 % print speed (500 mm/min). Image size is approximately 10 × 10 mm. . . . 26
3.11 Rheology of Al_2O_3/high molecular weight chitosan (HMWC) ink compared to phyllosilicate/powdered chitosan (PS/PC) ink. . . . 27
3.12 Raster print fidelity for varying chitosan content and print speed in Al_2O_3/HMWC chitosan inks. 28
3.13 Raster print fidelity for varying platelet content and print speed in Al_2O_3/HMWC inks. . . . 29
3.14 Influence of chitosan content on ink yield shear stress and storage modulus. . . . 30
3.15 Influence of platelet content on ink yield shear stress and storage modulus. . . . 30
3.16 Flow sweep responses for varying alumina and high molecular weight chitosan contents. . . . 31
3.17 Raster print fidelity for aqueous colloidal suspensions with varying alumina platelet content and print speed . . . 32
3.18 Raster print fidelity for varying fumed silica content . . . 33

3.19 Raster print fidelity for varying solid content and with the addition of biomineralisation nutrient solution . . . 34
3.20 Amplitude and flow sweep curves comparing PS/PC, Al_2O_3/HMWC, and Al_2O_3/CNF rheology. 35

4.1 Illustrated overview of characterisation process showing workflow. . . . 37
4.2 Views of sterile printing process inside a biosafety cabinet. . . . 39
4.3 Photos of coupon geometries directly after printing and after drying in air. . . . 39
4.4 Loading diagram of a four-point flexural test. . . . 40
4.5 Coupon height profiles in width-wise direction . . . 42
4.6 Coupon height profiles in length-wise direction . . . 43
4.7 Flexural strength statistics evaluated for each coupon batch. . . . 46
4.8 Flexural work of fracture statistics evaluated for each coupon batch. . . . 46
4.9 Scanning electron micrographs of coupon fracture surfaces . . . 48
4.10 Scanning electron micrographs of filament cross-sections for varying nozzle lengths . . . 49
4.11 Scanning electron micrographs of filament cross-sections for varying print speed . . . 50
4.12 Sample thermal decomposition curves obtained via thermogravimetric analysis. . . . 51

5.1 Differences in zeta potentials for phyllosilicate and alumina suspensions. . . . 55
5.3 Expected shear stress responses for time-independent viscoelasticity models. . . . 56
5.4 Comparison of shear stresses versus shear rates experienced by different ink compositions during flow sweep measurements. . . . 56
5.5 Hysteresis loops (shear rate ramp up and ramp down) for highly concentrated colloidal Al_2O_3 inks containing varying amounts of poly(ethylenimine) (PEI) flocculant. . . . 57
5.6 Stress stress and shear rate distributions across a nozzle demonstrating plug flow regime as determined by Hausmann et al. (2018). . . . 58
5.7 Nozzle velocity profiles for varying flow behaviour indices showing a widening of the critical radius. . . . 59

List of Tables

3.1 Preliminary ink formulation containing 40.4 wt% phyllosilicate platelets 25

4.1 Overview of Al_2O_3/CNF compositions prepared for material characterization 38
4.2 Shrinkage statistics obtained for each coupon batch. 44
4.3 Coupon densities measured via Archimedes' method immediately after immersion 44
4.4 Coupon densities measured via Archimedes' method after reaching equilibrium. 44
4.5 Computed theoretical densities and estimated void content using Archimedes' method on mechanically tested coupons and via coupon geometry. 45

This page has been intentionally left blank.

Nomenclature

Acronyms and Abbreviations

γ-PGA	Poly(γ-glutamic acid)
AM	Additive Manufacturing
CNC	Cellulose Nanocrystal(s)
CNF	Cellulose Nanofibre(s)
DIW	Direct Ink Writing
HMWC	High Molecular Weight Chitosan
MICP	Microbially-Induced Calcite Precipitation
MTM	Montmorillonite
PC	Powdered Chitosan
PDDA	Poly(diallylmethylammonium chloride)
PEI	Polyethyleneimine
PGA	Polyglutamic acid
PMMA	Poly(methyl methacrylate)
PS	Phyllosilicate
PTFE	Poly(tetrafluoroethylene)
SEM	Scanning Electron Microscope
SLA	Stereolithography

Greek Symbols

α	Failure mode factor
ΔP	Pressure drop across channel
δ	Phase lag
$\dot{\gamma}$	Shear rate
η	Viscosity
γ	Shear strain
γ_a	Shear strain amplitude
λ	Structural parameter
σ_c	Ultimate tensile strength
σ_m	Matrix tensile strength
σ_p	Platelet tensile strength
τ	Shear stress
τ_a	Shear stress amplitude
τ_i	Interface shear strength
τ_w	Wall shear stress
τ_y	Yield shear stress

Latin Symbols

G'	Storage modulus
G''	Loss modulus
G^*	Complex modulus
K	Fracture toughness, flow consistency parameter
K_{Ic}	Plane strain fracture toughness
K_{Jc}	Fracture toughness obtained via J-integral method
n	Flow behaviour index
R	Channel radius (geometric)
r	Channel radius (integration variable)
s	Platelet aspect ratio
s_c	Critical threshold s for change of failure mode
V	Tangential flow velocity in channel
V_p	Platelet volume fraction

This page has been intentionally left blank.

1 Introduction

When we think of strength and toughness, molluscs are rarely the first thing that comes to mind. Yet, nearly fifty years ago, Currey and Taylor (1974) revealed that molluscan shells possess exceptional strength and toughness despite being composed of weak base materials, a feat that remains challenging to replicate using synthetic materials (Ritchie, 2011). Similarly, bacteria might seem an unlikely ally in materials science, yet mineral-depositing strains can enhance material strength and even enable self-healing (Jonkers et al., 2010; Anbu et al., 2016). This thesis aims to explore the synergy between these two unlikely sources of inspiration, aiming to harness their mechanisms to develop advanced and sustainable structural materials.

1.1. Addressing our planet's needs

Before the industrial era, human-made structures primarily relied on naturally abundant materials: stone, clay, wood, hemp, flax, bone, shells, and, to a lesser degree, metals, formed the objects of daily life. However, the onset of the industrial era set in motion a relentless pursuit of better-performing materials, triggering a decisive shift towards synthetic alternatives known for their strength and durability. While these innovations have arguably improved the quality of life and fuelled economic growth, they have undeniably contributed to our current, pressing environmental challenges, particularly in climate change, resource depletion, pollution, and ecosystem destruction (IPCC, 2022).

The industrial sector alone is responsible for over 25% of annual global anthropogenic greenhouse gas emissions, with the majority stemming from the production of basic synthetic materials such as iron, steel, cement, plastics, chemicals, and non-ferrous metals like aluminium (Rissman et al., 2020; Hertwich, 2021; IPCC, 2022). Plastics, in particular, present a significant challenge: 92% of global plastics production is attributed to just seven groups of (semi-)synthetic polymers. Of all plastic waste, only 9% is recycled, while 12% is incinerated, and a staggering 79% is either landfilled or mismanaged, often ending up in unsanitary landfills, open pits, or the ocean (Geyer et al., 2017; Ritchie et al., 2023).

The need for sustainable alternatives to these environmentally harmful materials is evident. However, to encourage widespread adoption, these alternatives must match current materials' mechanical performance and cost-effectiveness. Developing such materials is a complex and open-ended challenge, but fortunately, there is a well-established source of inspiration to guide us: Nature.

1.2. Mimicking Nature

Industry demands don't often overlap with those of plants and animals, which optimise for functions like reproduction, nutrient transport, mobility, and signalling. In contrast, engineering settings typically push low-cost and lightweight solutions. Yet, there are surprising parallels. For instance, in plants, mass represents a metabolic investment, so evolutionary pressure favours structures that maximise stiffness and strength whilst minimising weight (Wegst et al., 2015). Similarly, the limited availability of chemical building blocks forces living organisms to develop innovative solutions using abundant elements, which tend to be cheap (Hurd et al., 2012). Crucially, whereas human-made materials typically embody relatively simple microstructures, plants and animals have evolved multifunctional materials that combine strength, damage tolerance, adaptability, self-healing ability, and low weight by harnessing complex interactions and structures spanning multiple length scales (Meyers et al., 2013; Wegst et al., 2015; Libonati and Buehler, 2017). Ample research

demonstrates that replicating these intricate biological strategies can significantly advance material design (Ball, 2001; Bhushan, 2009; Wegst et al., 2015).

This thesis seeks to pave the way for harnessing such complexity in biological systems to expand the capabilities of sustainable materials. Specifically, materials that are both tough (resistant to fracture) and strong (capable of bearing high loads before failure) are essential for safety-critical applications but remain challenging to replicate synthetically (Ritchie, 2011). This challenge has already been mastered by an unexpected source in the animal kingdom, which serves as the muse of this thesis: the mollusc.

1.3. The structure of the molluscan shell

Certain molluscs, like oysters and abalone, produce shells with an inner nacreous layer, "mother-of-pearl", that is not only visually striking but has also captivated materials scientists for a remarkable reason: despite being composed almost entirely (95 vol%) of ceramic material, the layer is both strong and tough under tension. To place into perspective, the toughness of pure aragonite is approximately 0.25 MPa m$^{1/2}$, while nacre exhibits a toughness up to 10 MPa m$^{1/2}$: a 40-fold increase (Wegst et al., 2015). More impressively, the work of fracture is 3000 times greater (Jackson et al., 1988). To understand the underlying mechanisms of this remarkable behaviour, this section and the next briefly review the structure and mechanics of nacre, drawing primarily from the reviews by Wang and Gupta (2011) and Wegst et al. (2015) unless otherwise stated.

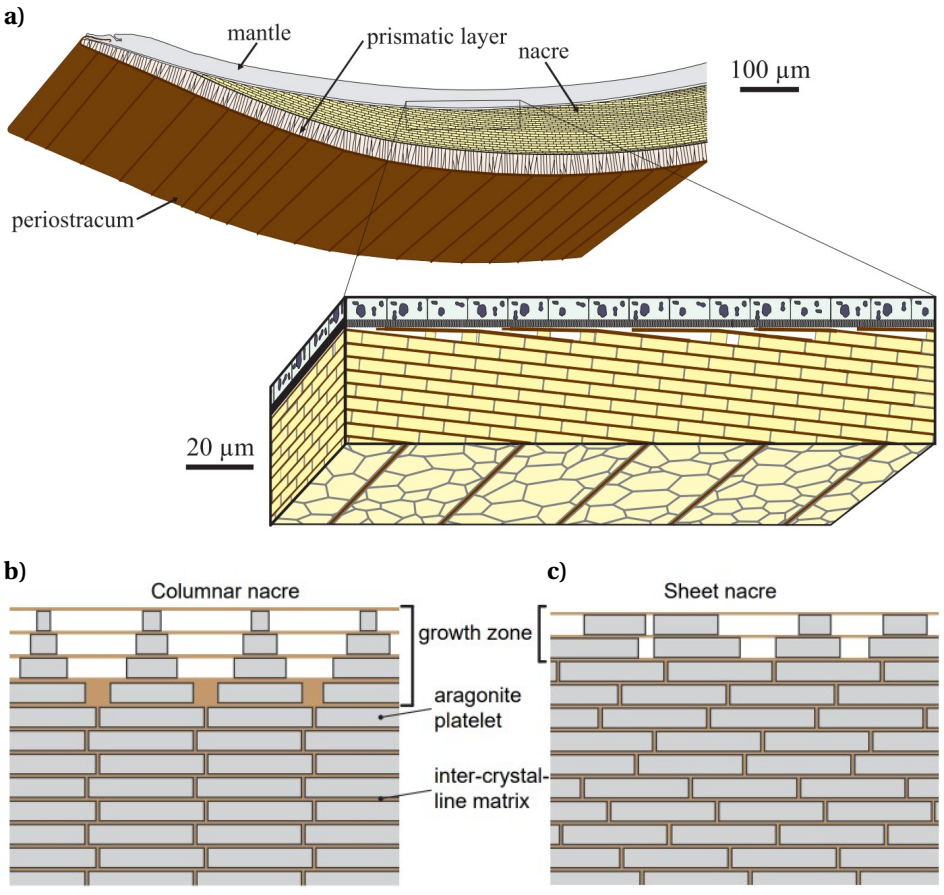

Figure 1.1: Schematic representation of the bivalve molluscan anatomy **(a)**, the two stacking arrangements found in nacre: the highly tessellated columnar nacre **(b)** and the randomly arranged sheet nacre **(c)**. Adapted from Cartwright et al. (2009) and Schmieden (2019).

Depicted in fig. 1.1, nacre is composed of alternating layers of thick (200–900 nm) mineral tablets and a thin (~30 nm) biopolymer matrix. These tablets, approximately 5–9 µm in diameter and polygonal in shape, consist mainly of aragonite, a mineral form of calcium carbonate ($CaCO_3$). When viewed from the side (fig. 1.2a), they contain a degree of non-uniformity in thickness, with edges being slightly thicker than the centre ("wavy" or "dovetail-like") in a highly conformal manner, i.e. remaining tightly stacked with adjacent layers (Barthelat et al., 2007; Espinosa et al., 2009). Early work using transmission electron microscopy

suggested that the tablets are monocrystalline, but later work proved that they are composed of millions of nanometre-sized (30–40 nm) grains bound together by a soft, amorphous biopolymer. Xie et al. (2010) and Oaki and Imai (2005) have also identified nanolayered structures within the tablets themselves. Although not completely understood, these nanograins and metalayers contribute to a tablet that is both more deformable and stronger than monolithic aragonite (Wang and Gupta, 2011).

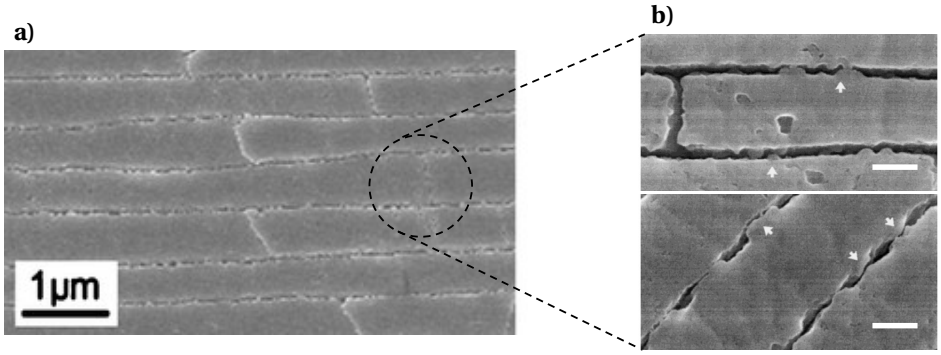

Figure 1.2: Scanning electron micrographs of natural nacre showing conformal non-uniform thickness ("waviness") **(a)**, and surface asperities and mineral bridges **(b)**. Scale bars in **b** are 200 nm. Adapted from Barthelat and Espinosa (2007).

The interlayer between tablets is filled mainly by the biopolymer matrix, which consists primarily of a well-ordered network of fibrous β-chitin, a polysaccharide, alongside various proteins, predominantly gel-like silk fibroin. However, the tablets are not smooth, and small mineral grains or 'asperities' 30–100 nm in diameter and ~10 nm in amplitude cover the tablet surfaces randomly with a spacing in the order of 60–120 nm, protruding into the interlayer and interposing with asperities of neighbouring tablets (fig. 1.2b). Some of these asperities form direct connections, 'mineral bridges', 5–50 nm in diameter between adjacent tablets. Crucially, this particular element of the microstructure forms the driving incentive of this thesis.

1.4. Deformation and toughening mechanisms in nacre

The structural arrangement described in section 1.3 gives rise to a captivating array of physical mechanisms. Under a quasi-static predatory load, the mollusc shell experiences a bending moment. Since the nacreous layer always exists under a harder, outside layer of prismatic calcite (fig. 1.1a), it is predominantly in tension and yields before the outside layer fails in compression. A shift in the neutral axis occurs, leading to a higher compressive stress in the prismatic layer and a higher tensile strain in the nacreous layer. This stress-strain asymmetry results in a flexural strength that is compression-dominated rather than tension-dominated, as typically expected for ceramics.

Early pioneering work by Currey (1977) showed that straining in nacre is accompanied by large-scale whitening of the sample, which was later associated with scattering of light due to widespread separation ('dilatation') between tablet ends. Later work showed that nacre indeed deforms primarily through shearing of the biopolymer and tablet sliding, as opposed to, for example, elongation of the tablets (Jackson et al., 1988; Sarikaya and Aksay, 1995; Wang et al., 2001).

The toughness of nacre, on the other hand, is driven by an impressive number of intrinsic and extrinsic mechanisms working synergistically to prevent crack propagation. At an abstract level, nacre not only has a high crack initiation toughness but also displays so-called "rising R-curve behaviour", i.e. its resistance to fracture increases with increasing crack extension. This behaviour is critical for inhibiting crack propagation as it means the material strengthens locally, drawing strain away from the crack.

The mechanisms behind this high and rising fracture resistance are a topic of extensive research but can be distilled into three principles. First, at the micrometre scale, crack deflection at the matrix-tablet interface leads to a highly tortuous crack path, requiring higher work of fracture to propagate. Second, behind the crack tip, tablets and matrix material bridging the crack wake continue to provide traction, shielding the crack tip from the applied load. Third, stress concentrations at the crack tip lead to the creation of a large 'process zone' where widespread inelastic deformation occurs, dissipating much of the energy that would otherwise go into propagating the main crack.

Various mechanisms have been proposed to explain the formation of this process zone, some of which are depicted in fig. 1.3b. Essentially, for strain redistribution to occur, hardening must take place locally at

peak stress locations. The key component for this behaviour in nacre was suggested by Barthelat and Espinosa (2007) and Barthelat et al. (2007): at large strains, the irregular thickness of the tablets causes physical interlocking, transferring stress to adjacent, non-locked regions. This locking behaviour agrees well with experimental measurements of the distances tablets slide before significant hardening occurs.

Additionally, at a smaller scale, Wang et al. (2001) and Evans et al. (2001) propose that the interposing asperities on tablet surfaces hinder sliding and provide increasing strain resistance. Similarly, mineral bridges formed between tablets require energy to break and subsequently function as additional asperities. At the nanoscale, individual macromolecules of the organic matrix have been measured to extend with a sawtooth-like force-extension curve, indicating the successive release of inter- and intramolecular interactions such as folded domains, loops, or sacrificial bonds, and were found to be reversible (Smith et al., 1999). Lastly, the nanograins comprising the tablets have been observed to rotate and deform, contributing to energy dissipation within the tablets themselves (Li et al., 2006).

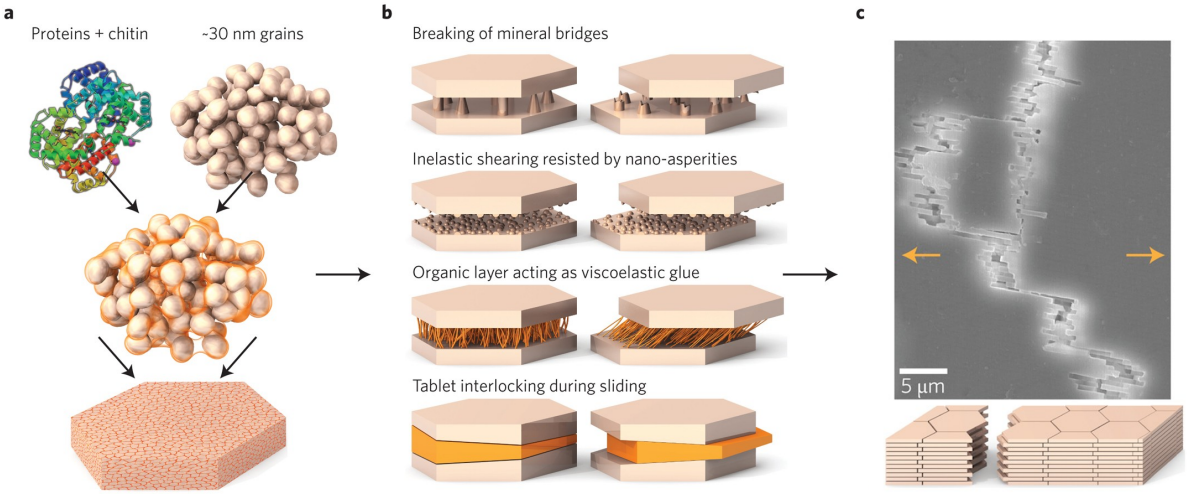

Figure 1.3: Overview of the hierarchical structure and properties of nacre. Adapted from Wegst et al. (2015).

This vast array of mechanisms contributes to the remarkable behaviour of nacre in differing amounts. However, other than tablet interlocking being the primary contributor to the rising toughness of nacre, the extent to which the remaining mechanisms contribute remains unclear from literature. It should also be noted that whereas much mechanical testing on nacre has been carried out in quasi-static conditions, under high strain rates, which more closely resembles the natural loading conditions, nacre shows even superior strength and toughness next to additional intra-tablet toughening mechanisms as demonstrated by Huang et al. (2011). The balance between mechanisms may shift with increasing loading rates, meaning more minor contributors should not be neglected. Future work may illuminate this and, more importantly, how to effectively replicate them. For the purpose of this report, the current depth of understanding will suffice. Instead, we shift our focus to the arduous efforts directed at replicating this complex behaviour.

1.5. Fabrication methods for synthetic nacre

Nacre's impressive performance has provoked a vast amount of research directed at replicating its structure using synthetic pathways, many aimed at finding combinations outperforming natural nacre using different base components (Corni et al., 2012; Wang et al., 2012; Wegst et al., 2015). As a consequence, a multitude of fabrication approaches has been reported in literature. In this section, those most promising from the perspective of scalability, mechanical properties, and ability to reproduce nacre's microstructure (Corni et al., 2012; Wegst et al., 2015) are briefly summarised and exemplified to provide context and reference for subsequent discussion. As a bare minimum, I consider only materials with layered microstructures in the micrometre range, with additional preference for those showing other nacre-like features such as segmented ceramic layers (i.e., tablets), surface asperities, and mineral bridges. For a more extensive description of synthetic fabrication approaches for nacre, the reader is referred to the reviews by Corni et al. (2012) and Wang et al. (2012). As far as I am aware, a more recent overview is not available at this time.

1.5.1. Freeze-casting

From a microstructure perspective, freeze-casting or 'ice templation' has been the most successful method for replicating nacre (Corni et al., 2012). The process and its resulting microstructure are exemplified in fig. 1.4. Developed by Deville et al. (2006), freeze casting involves freezing a ceramic suspension in a controlled manner to produce homogeneous, layered, porous scaffolds with lamellae ranging between 1–200 µm in thickness. Specifically, as a suspension of ceramic particles freezes, the particles are expelled from the growing ice crystals, concentrating in regions between them. Different microstructures can be obtained depending on factors such as particle size, cooling conditions, and solvent, including some resembling nacre (Deville, 2008). Freeze drying then removes the solvent, leaving only the ceramic scaffold, which can be infiltrated to produce dense, layered composites.

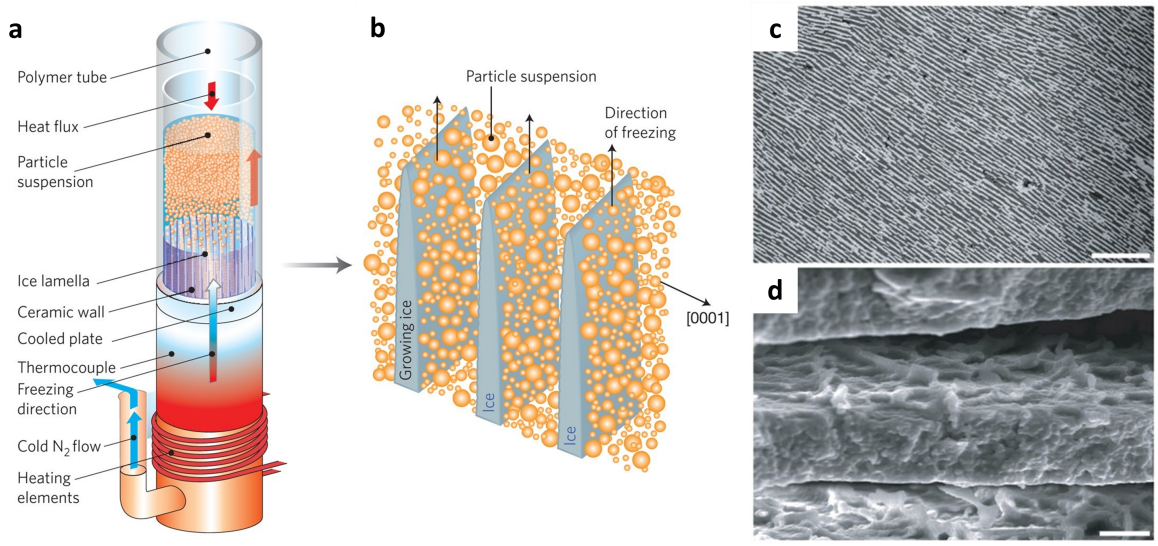

Figure 1.4: Schematic representation of freeze casting and resulting microstructure. Controlled, directional freezing **(a)** causes suspended ceramic particles to be expelled from growing ice crystals (**b**), resulting in lamellar microstructures (**c**) with surface roughness (**d**) resembling that of nacre. Scale bars are 300 µm (**c**) and 10 µm (**d**). Adapted from Wegst et al. (2015) **(a-b)** and Deville et al. (2006) **(c-d)**.

Munch et al. (2008) used this method to produce a hybrid consisting of poly(methyl methacrylate) (PMMA) and alumina (Al_2O_3). Mechanical properties vastly exceeding those of nacre were obtained: the composite reached a flexural strength of approximately 200 MPa and fracture toughness exceeding 30 MPa $m^{1/2}$, comparable to some aluminium alloys.

Bouville et al. (2014) froze a suspension containing alumina platelets, alumina nanoparticles, and glass-phase precursors, causing the platelets to self-assemble into aligned structures with the nanoparticles and precursors dispersed between them. Upon pressing and sintering, the glass precursor melts, and the porous scaffold collapses, forming a dense (<2% void content) composite. Because of the high surface area and curvature, the alumina nanoparticles sinter at lower temperatures than the platelets, forming mineral bridges and surface asperities similar to those characteristic of nacre (Bouville et al., 2014). Despite being entirely composed of ceramic material, the composite showed remarkable toughening and mechanical properties with a flexural modulus of 290 GPa, a flexural strength of 470 MPa, and a fracture toughness (K_{IC}) of 17.3 MPa $m^{1/2}$.

Despite its relative success, freeze-casting has yet to achieve the characteristic waviness of nacre's tablets, a feature essential for its toughening behaviour. While advances in freeze-casting techniques may address these challenges in the future (Shao et al., 2020), the high energy demands for freezing, vacuum drying, and sintering involved make it unlikely to be either a cost-effective or environmentally sustainable process for replicating nacre's microstructure at an industrial scale (Launey et al., 2009).

1.5.2. Hot-press assisted slip casting

An alternative approach was introduced by Ekiz et al. (2009), who combined slip casting with hot-pressing to produce nacre-like composites. This method, illustrated in fig. 1.5, enabled the fabrication of composites containing up to 60 vol% inorganic content, with flexural stiffness and strength values ranging from 19–23 GPa

and 133–155 MPa, respectively, similar to those of natural nacre.

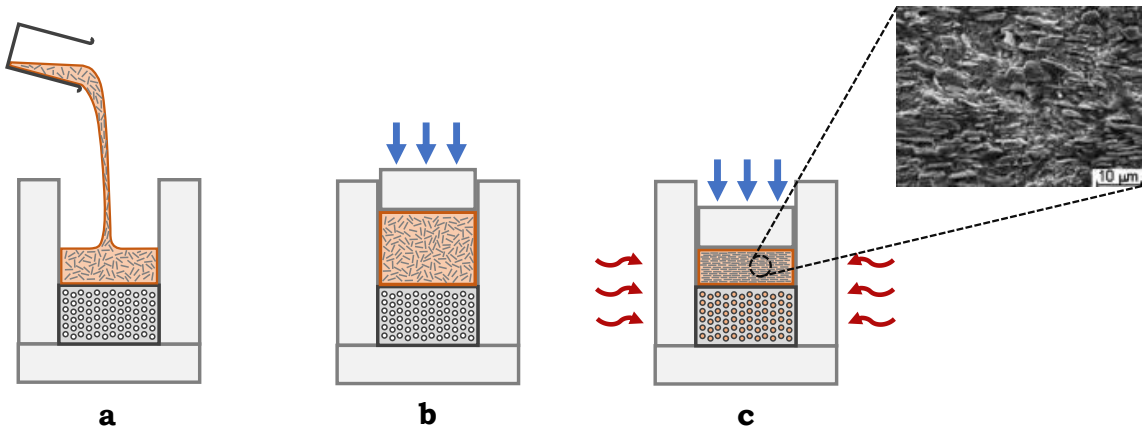

Figure 1.5: Schematic representation of hot-press assisted slip casting. A mixture of a fluid phase (e.g. resin or precursor particles) and platelets is poured into a die containing a porous mould (**a**), after which the contents are pressed, squeezing the excess fluid out of the mixture and into the porous mould **(b)**. The system is then heated to develop the matrix (i.e., cure the resin, sinter the precursor), producing a dense, segmented, and layered composite **(c)**. Own work based on illustrations from Ekiz et al. (2009) and Guner and Dericioglu (2016).

Ferrand et al. (2015) used magnetic orientation during the casting process to align alumina platelets, fabricating a range of heterogeneous composites with nacre-like characteristics. In addition to alumina/polymer and alumina/metal combinations, they prepared a ceramic/ceramic slurry comprising alumina platelets, alumina nanoparticles, and silica, akin to the method used by Bouville et al. (2014). After sintering under pressure at 1500 °C[1], they achieved a dense composite with 95.5 vol% alumina content, featuring both surface asperities and bridges. This structure resulted in the highest mechanical performance observed in their study, with a flexural strength of 650 MPa and a fracture toughness (K_{JC}) of 14 MPa m$^{1/2}$. While this 'bulk' approach avoids freezing and vacuum drying, it compromises both shaping flexibility and microstructural precision and still requires sintering to form mineral bridges and asperities.

1.5.3. Layer-by-layer deposition

In contrast, layer-by-layer deposition, or layer-by-layer (self-)assembly, provides much finer microstructural control. The method enables fabricating thin layered films by sequentially adsorbing complementary multivalent molecules onto a substrate. Initially proposed by Iler (1966) and later pioneered by Decher et al. (1992) and colleagues, the method was first based on electrostatic interactions between layers, as shown in fig. 1.6a, but has since expanded to include various non-electrostatic interactions, such as coordination chemistry and stereocomplexation (Borges and Mano, 2014). Deposition can be performed using well-established methods such as dip-coating, spin-coating, spraying, and perfusion, allowing for highly controlled monolayer compositions (Wang et al., 2012).

Tang et al. (2003) employed this method to fabricate wavy, segmented layered composites resembling nacre by stacking montmorillonite (MTM) clay nanoplatelets (0.9 nm thick) with poly(diallyldimethylammonium chloride) (PDDA) as shown in fig. 1.6b, resulting in tensile strength and stiffness values of 106 MPa and 11 GPa, respectively. Building on this, variations of MTM-based layer-by-layer assembled composites, for example, using different polymers or cross-linking agents, have significantly enhanced tensile properties, reaching strengths as high as 400 MPa and stiffness values up to 106 GPa as reported by Podsiadlo et al. (2007). In a related approach, Bonderer et al. (2008, 2009) fabricated layered alumina/chitosan films with a 15% volume fraction, achieving tensile strength and stiffness values of 315 MPa and 9.6 GPa, respectively, at a fracture strain of 21%.

Despite these impressive mechanical properties, current layer-by-layer approaches are limited by the significant time required, often several minutes for each micro- or nanometre-thick layer, which remains a considerable barrier to practical application.

[1] Although the authors refer to this as 'hot-pressing,' 'sintering' may be more accurate here, especially given the lower 150 °C temperature used by Ekiz et al. (2009) for 'hot-pressing'.

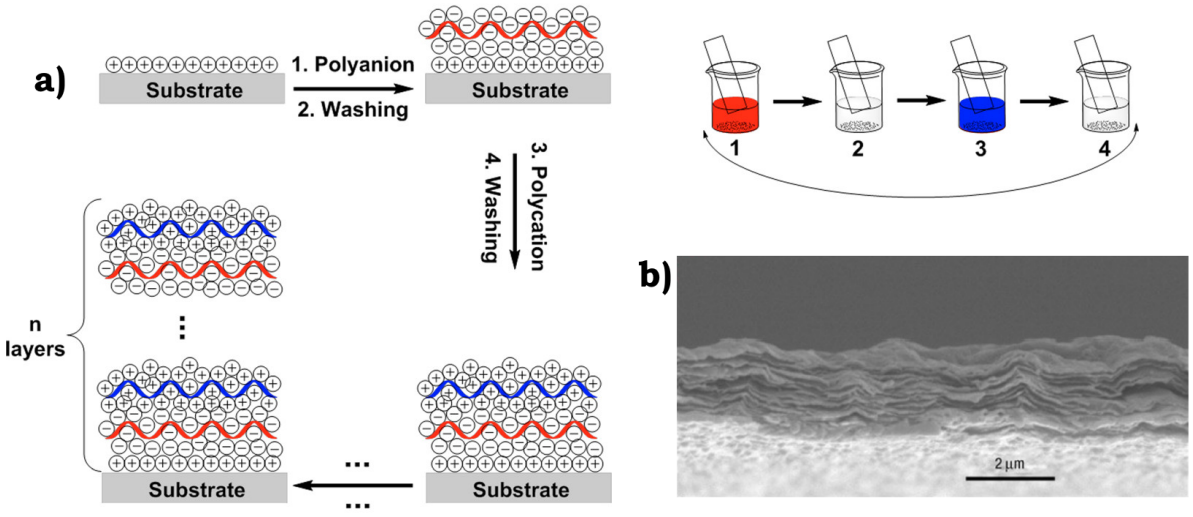

Figure 1.6: Schematic representation of layer-by-layer deposition **(a)** and resulting microstructure **(b)**. (Non-)electrostatic interactions between multivalent molecules are leveraged to generate thin layered materials to achieve a certain function or microstructure. Adapted from Borges and Mano (2014) and Tang et al. (2003).

1.5.4. Paper-making method

To address these scalability challenges, Walther et al. (2010a,b) developed nacre-like composites using a method inspired by paper production, shown in fig. 1.7. In this approach, clay (MTM) nanoplatelets are dispersed in a dilute aqueous solution of polyvinyl alcohol (PVA), allowing the PVA to adsorb onto the platelets in thin 1 nm layers. The platelets are then layered by vacuum filtration and dried at 80 °C to produce compact composites with a 70% volume fraction. This method yielded a borate cross-linked composite with a maximum Young's modulus of 45.6 GPa and tensile strength of 248 MPa.

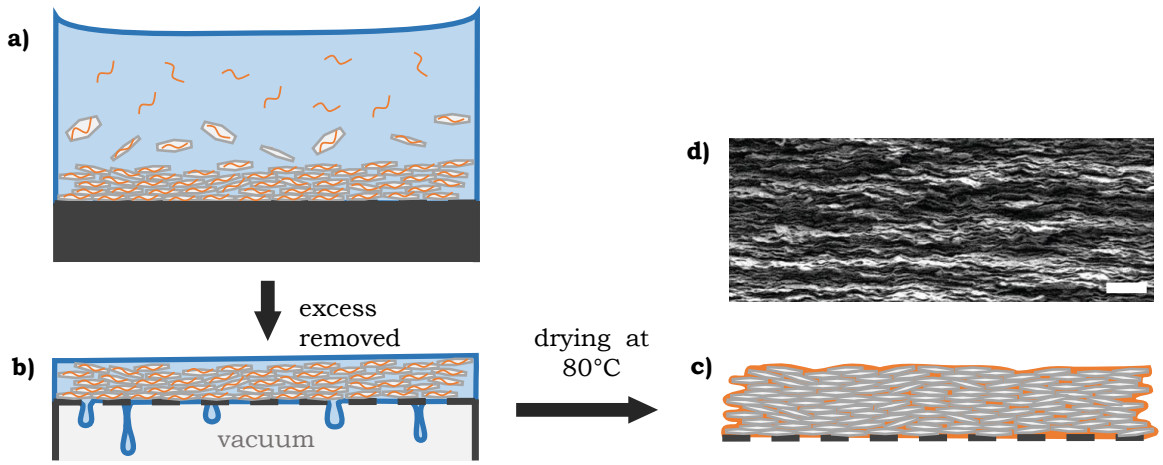

Figure 1.7: Schematic representation of the paper-making approach of Walther et al. (2010a,b). A solution containing polymer-adsorbed platelets **(a)** is centrifuged or sedimented, after which the excess polymer solution is decanted. The solution is further organised via vacuum filtration **(b)** followed by drying at 80 °C to produce a dense composite **(c)**. SEM image of resulting PVA/MTM composite **(d)** as obtained by Walther et al. (2010b). Own work based on the description of Walther et al. (2010b).

This method strikes a balance between the simplicity of bulk approaches and the precision of layer-by-layer techniques. However, it is constrained to flat or mildly curved samples, leaving the fabrication of larger, more complex shapes a significant challenge.

1.5.5. Other methods

In addition to the methods discussed so far, a few other techniques and single experiments are worth mentioning briefly. Despite the poor mechanical results reported by Almqvist et al. (1999) and Chen et al. (2008), centrifugation has demonstrated a very short production time while simultaneously achieving similar detail as layer-by-layer deposition. Mechanical properties can be improved by decreasing the organic content (of 20 vol%) or by using different materials (Corni et al., 2012). Extrusion and roll compaction, on the other hand, a bulk method used by Wang et al. (2000), can partly reproduce the fracture mechanisms in nacre and exhibited impressive mechanical properties with a bending strength of 750 MPa at a fracture toughness (K_{Ic}) of 28.90 MPa m$^{1/2}$. So far Wang et al. (2000) seem to be the only group to publish on the method.

More recently, Gao et al. (2017) fabricated bulk artificial nacre by stacking nacre-like bushite/sodium alginate thin films produced via an evaporation-induced self-assembly technique. Following binding of the layers with chitosan, cross-linking with Ca^{2+} ions, and hot-pressing at 80 °C and 100 MPa, a flexural strength up to 267 MPa was achieved with corresponding stiffness and fracture toughness (K_{Ic}) of 18.6 GPa and 1.9 MPa m$^{1/2}$, respectively.

Similarly, Grossman et al. (2017, 2018) stacked discs of alumina platelets produced using a vacuum-assisted magnetic alignment process, sintering under pressure, and infiltrating with epoxy. Maximum flexural strength of the resulting composite exceeded 350 MPa at a corresponding stiffness of about 150 GPa and toughness (K_{Ic}) above 6 MPa m$^{1/2}$. Shortly after, Grossman et al. (2019) investigated the same material stacked with polyethyleneimine (PEI) films in between, producing a laminate with alternating full-polymer and nacre-like layers. In this case, flexural stiffness, strength, and fracture toughness (K_{Ic}) values were about 100 GPa, 250 MPa, and 5–6 MPa m$^{1/2}$, respectively.

Zhao et al. (2020) developed a continuous shear-flow-induced alignment technique based on what they refer to as the 'superspreading' of liquid droplets containing alginate, graphene oxide nanosheets, clay nanoplatelets and carbon nanotubes onto a hydrogel substrate. After cross-linking the alginate with calcium, the resulting thin films reached a remarkable strength of up to 1200 MPa and toughness up to 36.7 MJm^{-3}, more than 20 times that of natural nacre. Although lamination is required to obtain 'bulk' material, dropped the tensile strength down to 518 MPa and toughness down to 3.3 MJm^{-3}, the method still exceeds the strength and toughness of nacre by factors of 4 and 2 respectively.

1.5.6. In summary

Despite the relatively successful results, each method described so far fails to demonstrate the complete combination of nacre-like features, high mechanical properties, industrial scalability, environmental sustainability, and shaping freedom. For many bulk approaches, there seems to be a trade-off between macroscopic speed and microscopic control. All methods requiring sintering involve inherently high energy expenditures, and layering techniques have remained limited to thin films or flat bulk samples.

1.6. To rule them all: additive manufacturing

Recently, additive manufacturing (AM) technologies have provided new opportunities for microstructure control in bulk materials while retaining high production rates and offering unprecedented shape control (Wegst et al., 2015; Feilden et al., 2017; Yang et al., 2018). AM's inherently low-energy, decentralised, and highly scalable nature adds immense environmental and economic attractiveness, which may be leveraged to combat the range of issues hampering the widespread adoption of previous methods. Among the AM methods available, such as sub-µm printing (Jang et al., 2013) and magnetic orientation in stereolithography (Martin et al., 2015), direct ink writing (DIW) has presented itself as a strong candidate for replicating the complex microstructure of nacre (Studart, 2016; Feilden et al., 2017).

Illustrated in fig. 1.8, DIW or 'robocasting' is a process involving the continuous extrusion of a viscoelastic material through a syringe nozzle onto a large substrate or 'print bed' (Feilden et al., 2017). In the context of nacre mimicry, shear forces arising during extrusion can be leveraged to align particles in the extrusion direction (inset, fig. 1.8), making it possible to produce filaments with controlled microstructures rapidly (Feilden et al., 2017). Alternatively, magnetic fields have been used to align platelets during extrusion to achieve the same goal (Kokkinis et al., 2015).

Feilden et al. (2017) used this method to additively manufacture or '3D-print' a water-based Pluronic F-127 hydrogel mixed with a 7:3 wt% ratio of alumina platelets and sub-micrometer alumina powder. After drying, pressing at 300 MPa, burning out the hydrogel at 500 °C and sintering at 1550 °C, a preform with a strength of 50 MPa was obtained. This preform was infiltrated with epoxy under vacuum, leading to an

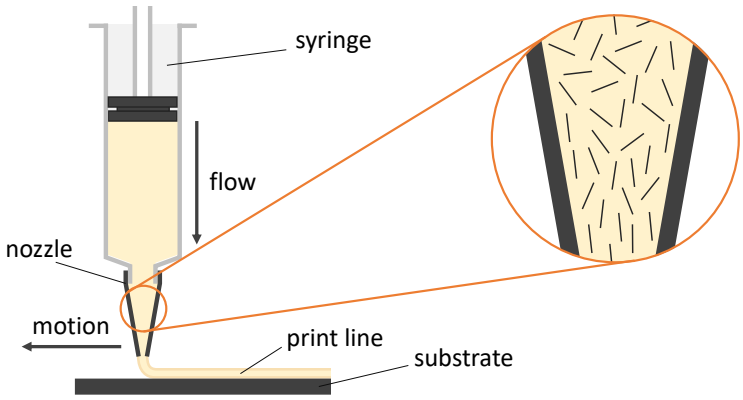

Figure 1.8: Schematic representation of direct ink writing or 'robocasting'. Inset depicting the shear-induced alignment of non-spherical colloids such as platelets and fibres in the nozzle during extrusion. Own work.

anisotropic composite with a maximum (trans-filament) flexural strength of 202 MPa with corresponding fracture toughness (K_{Ic}) and Young's modulus of 3.0 MPa m$^{1/2}$ and 99.1 GPa, respectively. Since then, as far as I am aware, no other attempts have been made at producing nacre-like composites via DIW.

1.7. A key novel ingredient: bacteria

Whereas most studies have focused on trying to match the inorganic volume fraction and well-stacked 'brick-and-mortar' microstructure of natural nacre, more recent work suggests that platelet interconnectivity plays a more significant role in achieving high strength, stiffness, and toughness in nacre-mimetic materials (Naglieri et al., 2015; Grossman et al., 2017; Gu et al., 2017; Grossman et al., 2018). So far, the formation of this interconnectivity has required sintering under pressure and at temperatures close to the melting point of the ceramic, thereby sacrificing energy efficiency and, in turn, environmental friendliness. To pave the way towards sustainable, advanced ceramic composites, a new approach should ideally be devised to produce such interconnectivity.

Biomineralisation is an excellent candidate for performing this task in milder conditions. By leveraging enzyme-driven processes that are difficult to recreate artificially, mineral bridges may be synthesised *in situ* using readily available and non-toxic raw materials (section 2.1). To demonstrate, recently, Spiesz et al. (2019) produced layered calcium carbonate/polyglutamate (PGA) composites by alternately immersing a substrate into a biomineralisation medium and a bath containing bacterially-produced PGA. The biomineralisation medium contained *Sporosarcina pasteurii* bacteria that deposit calcium carbonate in the presence of urea and calcium ions, after which the PGA binds to it. Repeating this 23 times yields a ~200 µm thick, layered composite. Later, Yu et al. (2021) fabricated mouldable bulk layered composites from a slurry of three bacteria that respectively produce cellulose, PGA, and $CaCO_3$. The size of $CaCO_3$ crystals was controlled by the PGA and by varying the ratio of Ca^{2+}:Mg^{2+} ions. The mouldability of these composites was later leveraged by Nettersheim (2022), who demonstrated that 3D-printing of the slurry is possible upon the introduction of alginate as a shear-thinning agent. This also happened to improve mechanical properties.

Other than these examples, as far as this author is aware, no other attempts have been made at 3D-printing nacre-like materials using bacteria as stiffening agents. Other 3D-printed materials have, however, been stiffened in similar conditions. With some resemblance, Xin et al. (2021) SLA-printed cubic polymer scaffolds from a tough resin and submerged them in a biomineralisation medium containing *S. pasteurii*, which almost fully (>95%) filled the sparse cubic scaffold. By varying the architecture of the template scaffold, layered polymer-ceramic composites were manufactured with specific strength and toughness similar to natural nacre and the freeze-cast PMMA/Al_2O_3 composites obtained by Munch et al. (2008).

Hirsch et al. (2023) 3D-printed an alginate microgel containing gelatin-encapsulated *S. pasteurii* that, upon immersion in a solution of $CaCl_2$, urea, and yeast extract, is stiffened and strengthened via biomineralisation. Despite the poor resulting compressive strength of 3.5 MPa, the study provides useful insight into the printing process and the behaviour of the bacteria. Similarly, Chen et al. (2022) performed direct ink writing of a UV-cross-linkable hydrogel containing mineralising alkaline phosphatase enzymes, which upon submer-

sion in a solution of Ca^{2+} resulted in stiffening of the hydrogel. However, again, only mediocre mechanical properties were achieved with tensile strength and stiffness of 3 MPa and 0.150 GPa, respectively.

An appealing prospect of using live bacteria mentioned by Nettersheim (2022) is that they can be re-activated to make materials containing them self-healing. Self-healing nacre has been investigated in the past by Du et al. (2019) using Diels-Alder chemistry, but the approach requires heating to trigger bond reformation. Bacteria such as *S. pasteurii* are endospore-producing, meaning they assume a dormant state until suitable conditions for revival arise. Increased nutrient availability in cracks can re-activate the bacteria, triggering biomineralisation and subsequent crack healing as demonstrated for concrete by Jonkers et al. (2010). Other spore-forming bacteria such as the PGA-producing *B. Licheniformis*, as used by Yu et al. (2021) and Nettersheim (2022), could be leveraged to, for instance, make self-healing biopolymer matrices. As far as I am aware, this topic remains largely unexplored.

Synthetic biology is evolving at an extraordinary pace, expanding our ability to engineer living systems for human needs (Gilbert and Ellis, 2019; Rodrigo-Navarro et al., 2021). The concept of using living cells to precisely and sustainably manufacture entire structures and materials is quickly becoming a realistic prospect (Gilbert and Ellis, 2019). It is crucial to bear in mind the vast control that may be possible in the future, especially concerning the approach of this thesis.

1.8. Research definition

The ability of nacre to overcome the typical mutual exclusivity of strength and toughness via mostly well-understood microstructural features provides a compelling incentive for mimicry. The simplicity, energy efficiency, and shaping freedom by which direct ink writing enables the production of nacre-mimetic microstructures with minimal competition makes it an ideal manufacturing platform. Combined with the largely unexplored potential of incorporating biomineralising bacteria into materials, especially in nacre-like materials to replicate mineral bridges, a vast terrain of unanswered questions is opened up.

Given the demand for materials that offer similar or improved performance compared to synthetic materials but with significantly reduced environmental impact and comparable cost, a highly relevant research gap exists in the junction of biomimicry, direct ink writing, and living materials. The central concept around which this thesis revolves is therefore:

> *The application of biomineralising bacteria in nacre-mimetic materials fabricated by direct ink writing to improve mechanical properties and provide unique material characteristics.*

The term 'unique material characteristics' is deliberately unspecific; it is warranted considering that this approach has no prior reference and, therefore, that hypothesis generation is a driving incentive. The research is guided by drawing specific objectives from this concept, given below.

Research objectives

The main research objective of this thesis is defined as:

> *To investigate the direct ink writing of a nacre-mimetic material incorporating biomineralising bacteria by characterising the printing process, the bacterial activity, and the resulting material.*

Further sub-objectives are specified as follows:

1. To determine a suitable ink formulation and corresponding printing condition for the direct ink writing of biomineralised nacre-mimetic material,
2. To characterise the ink in terms of its printability, ability to produce nacre-resembling material, and ability to support biomineralisation,
3. To determine how these results depend on the formulation,
4. To characterise the resulting material regarding its physical and mechanical properties and link this back to ink formulation and bacterial activity.

Research questions

To satisfy the research objectives, the main research question to answer becomes:

> *How can we print nacre-mimetic material incorporating biomineralising bacteria, and how do the ink formulation and bacterial activity influence the printing process and resulting material?*

This main question can be split into four further sub-questions of relevance:

1. How must an ink be formulated to achieve a microstructure resembling nacre via direct ink writing?
2. How do printing conditions affect printability and microstructure?
3. How do ink constituent quantities relate to bacterial activity, microstructure and the corresponding mechanical behaviour?

In summary, this research aims to explore the integration of biomineralising bacteria into nacre-mimetic materials using direct ink writing, providing a novel approach with the potential to address both material performance and sustainability challenges. These formalised objectives and research questions set the stage for the subsequent planning and execution of the project.

1.9. Project planning

The 100% Full Time Equivalent commitment level timeline, introduced as of September 2022, applies to this thesis project. This assumes a nominal duration of 32 weeks that may extend up to 39 weeks to accommodate interruptions such as holidays, illness, or other unforeseen reasons. To schedule the work into a feasible timeline, first, a Work Breakdown Structure (WBS) was constructed, delineating the main experimental tasks of this project into four work packages, including their dependencies and interrelations. The WBS can be found in appendix A.1. Following this, a timeline was drafted aimed at 32 weeks, totalling 36 weeks when including 4 weeks of pre-planned holidays and leaving 3 weeks of overhead. The timeline can be found in the form of a Gantt chart in appendix A.2. A reflection on the timeline can be found in appendix A.3.

1.10. Report overview

This thesis document consists of six chapters. Following the current, chapter 2 covers the fundamental principles of biomineralisation, rheology, shear-induced alignment, and the design of artificial nacre, providing essential background for setting up experiments and interpreting results. The formulation, preparation, and assessment of ink compositions via rheology and printing experiments are detailed in chapter 3. Chapter 4 covers the physicochemical characterisation of the printed material, including coupon geometry measurement, microstructure determination via scanning electron microscopy (SEM), and mechanical testing via 4-point flexural tests. The findings of these chapters are percolated into a comprehensive discussion in chapter 5, referencing back to the background and related literature. Finally, chapter 6 presents the conclusions, answers the research questions, provides recommendations for future work, and reflects on the project's significance and future opportunities.

This page has been intentionally left blank.

2

Background

Moving from concept to practice requires some foundational knowledge of underlying principles and processes, which is provided in this chapter. In particular, inducing and controlling biomineralisation requires understanding its mechanism and the factors influencing it, described in section 2.1. In section 2.2, a brief introduction is given to rheology, the branch of physics dealing with the deformation and flow of materials and a vital asset to the assessment of inks used in direct ink writing. Closely related, section 2.3 introduces the concept of shear-induced alignment of particles in colloidal inks. Finally, a summary of key design factors of nacre-mimetic materials identified from literature is given in section 2.4. These partly motivate the methodology used in subsequent chapters.

2.1. Microbially-induced calcite precipitation

Certain microbes have been observed to trigger the formation of solid calcium carbonate ($CaCO_3$) crystals from a solution containing urea ($CO(NH_2)_2$) and a calcium source (Anbu et al., 2016). Essentially, they induce a local increase in pH, which triggers the spontaneous precipitation of calcium carbonate in the presence of Ca^{2+} and ${CO_3}^{2-}$ due to a decrease in the solubility of the ions. This geo-biochemical process has been coined as 'microbially-induced calcite precipitation' (MICP). MICP can occur via various possible pathways depending on the organism involved. Of particular relevance to this thesis is the ureolytic pathway. Here, urease, an enzyme responsible for the hydrolysis of urea, causes the production of ammonia (NH_3), which raises pH. Chemically, the process proceeds as follows (DeJong et al., 2006; Anbu et al., 2016):

$$CO(NH_2)_2 + H_2O \xrightarrow{\text{Urease}} NH_2COOH + NH_3 \tag{2.1}$$

The carbamic acid hydrolyses spontaneously into an additional mole of ammonia:

$$NH_2COOH + H_2O \longrightarrow NH_3 + H_2CO_3 \tag{2.2}$$

The two products, NH_3 and H_2CO_3, exist in an equilibrium state:

$$H_2CO_3 \longleftrightarrow {HCO_3}^- + H^+ \tag{2.3}$$

$$2\,NH_3 + 2\,H_2O \longleftrightarrow 2\,{NH_4}^+ + 2\,OH^- \tag{2.4}$$

The production of hydroxide ions (eq. (2.4)) increases the pH, which can shift the bicarbonate equilibrium (eq. (2.3)), resulting in the formation of carbonate ions:

$${HCO_3}^- + H^+ + 2\,OH^- \longleftrightarrow {CO_3}^{2-} + 2\,H_2O \tag{2.5}$$

In the presence of a calcium source, e.g. $CaCl_2$, calcium carbonate starts to precipitate spontaneously with increasing rate up to pH 10 (Stocks-Fischer et al., 1999):

$$Ca^{2+} + {CO_3}^{2-} \longleftrightarrow CaCO_3\downarrow \tag{2.6}$$

In addition, a locally high pH occurs near the cell due to the production of $NH_4{}^+$. Since the cell wall is negatively charged, calcium ions accumulate, favouring local precipitation of $CaCO_3$:

$$Ca^{2+} + \text{Cell} \longrightarrow \text{Cell}-Ca^{2+} \tag{2.7}$$

$$\text{Cell}-Ca^{2+} + CO_3{}^{2-} \longrightarrow \text{Cell}-CaCO_3 \tag{2.8}$$

A schematic overview of the entire process is shown in fig. 2.1.

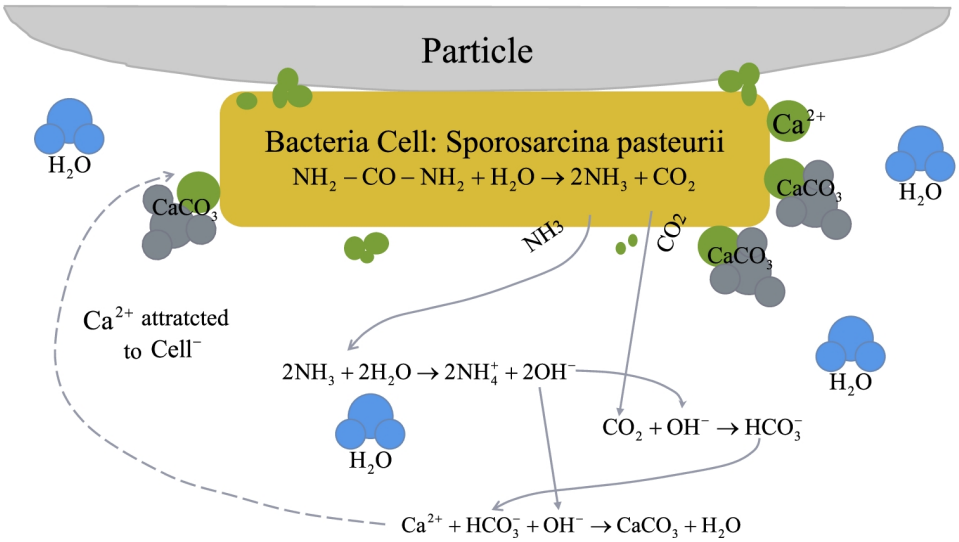

Figure 2.1: Schematic representation of microbially-induced calcite precipitation by *S. pasteurii* . Taken from DeJong et al. (2010).

A common choice for MICP is *Sporosarcina pasteurii* , a soil-borne, non-pathogenic, endospore-forming bacterium with a high urease activity that can tolerate extreme conditions (Anbu et al., 2016; Hirsch et al., 2023). This bacterium was selected for this thesis project for its commonality, biosafety, and availability in the lab. Relevant to know then is how to identify MICP when it occurs. Many studies have shown that the precipitate morphology can be identified in scanning electron microscopy as shown in fig. 2.2.

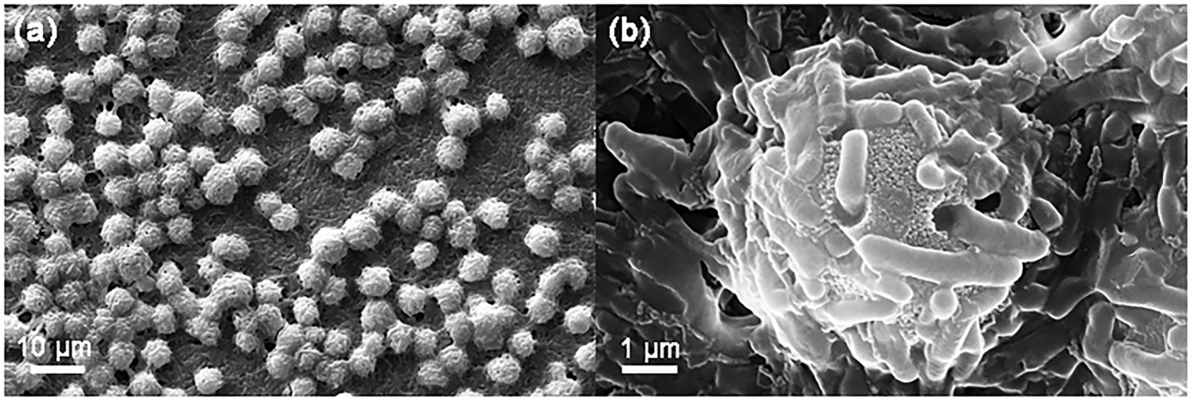

Figure 2.2: Scanning electron micrograph of typical MICP precipitate morphology obtained in urea- and calcium-rich medium containing live *S. pasteurii* cells at pH 9. Taken from Ghosh et al. (2019).

Critical for the experimental work here is knowing the various factors affecting the rate and yield of MICP by *S. pasteurii* . These factors establish experimental boundaries and can allow MICP to be controlled to yield the desired results. Intuitively, one would expect environmental factors such as temperature, pH, oxygen availability, and nutrient concentrations to play the most important roles. Fortunately, *S. pasteurii* is relatively insensitive to temperature, demonstrating optimal conditions for MICP between 20–40 °C, with measurable precipitation as low as 10 °C and as high as 50 °C (Okwadha and Li, 2010; Tang et al., 2020). Stocks-Fischer et al. (1999) reveal that pH plays a decisive role in urease activity (fig. 2.3a) and thus in both chemical and

microbial precipitation (fig. 2.3b). Note the lower solubility of calcite in the medium than in water, favouring precipitation. The rate of MICP is relatively independent of the concentration of the calcium source as long as it is available and much more strongly dependent on bacterial density (Stocks-Fischer et al., 1999; Tang et al., 2020).

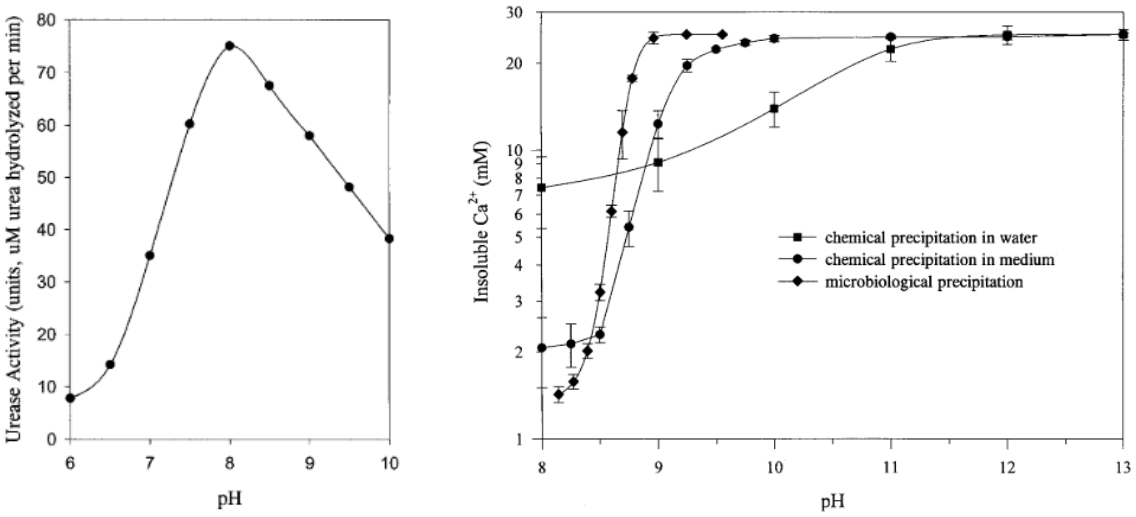

(a) Effect of pH on urease activity from the cell-free extract of *S. pasteurii*.

(b) Effect of pH on chemical and microbial calcium carbonate precipitation.

Figure 2.3: Effects of pH on MICP as measured by Stocks-Fischer et al. (1999).

Regarding oxygen, growth and proliferation of *S. pasteurii* has been shown to severely reduce in anoxic conditions as expected for aerobic bacteria (Seifan and Berenjian, 2018). Mortensen et al. (2011) show that the activity of urease fortunately remains unhindered. These authors find that anaerobic cultures indicated *higher* urease activity than oxic cultures over the same period. This finding is crucial in assuring that MICP occurs inside printed material where oxygen diffusion is likely limited. However, this suggests a practical limitation: sufficient bacteria must be present in the ink beforehand to trigger widespread MICP, as a minimum amount is not likely to spread to saturate the material. This aspect will be discussed later in the report.

The attentive reader may note the similar total yields for MICP and chemical precipitation in fig. 2.3b, sparking the question of why one would prefer MICP. After all, the conditions required for *S. pasteurii* to function may be detrimental to material strength and may be avoidable using chemical methods. The key difference here lies in the fact that whereas chemical precipitation happens almost instantaneously and occurs primarily in the free fluid, MICP can be precisely controlled in terms of timing, rate, morphology, and distribution by controlling the behaviour of the bacteria. MICP also tends towards nucleation at particle surfaces over free precipitation (DeJong et al., 2010), and it has been possible to produce nanometre-sized crystals (Ghosh et al., 2019). These aspects are central to the goal of replicating the inter-platelet microstructural features in nacre, especially the mineral bridges found to be crucial for mechanical strength in synthetic replicates (Naglieri et al., 2015; Grossman et al., 2017; Gu et al., 2017; Grossman et al., 2018).

Finally, both the presence of certain polymers and the addition of magnesium ions into the biomineralisation medium have been shown to reduce precipitate sizes, which may be leveraged to tune morphology (Davis et al., 2000; Tsortos and Nancollas, 2002; Yu et al., 2021).

2.2. Rheology

An indispensable analytical concept used extensively throughout this thesis is rheology, the branch of physics describing matter that exhibits both solid-like elastic behaviour and fluid-like viscous behaviour, known as viscoelasticity. Inks used in DIW fall strongly within this category: they must flow smoothly through a nozzle without clogging (fluid-like behaviour) yet retain their shape and support themselves once deposited (solid-like behaviour). This variable behaviour is made possible by shear-dependent structural changes at the molecular scale that facilitate flow under shear, i.e. a shear-thinning behaviour.

The properties of inks for DIW are often characterised by measuring their response to oscillatory shear. In

such measurements, there is a delay, a phase difference, between the applied strain and the resulting stress response as a result of having both a component proportional to instantaneous shear and a component proportional to shear *rate*, the derivative of shear, delayed by exactly 90°. The combination gives a phase delay δ between 0–90°. The ratio of the shear strain amplitude γ_a and the resulting shear stress amplitude τ_a gives the magnitude of the resistance to shear, the complex modulus, G^*:

$$G^* = \frac{\tau_a}{\gamma_a} \tag{2.9}$$

This modulus is decomposed into the elastic and viscous components using the phase delay:

$$G' = G^* \cos\delta \tag{2.10}$$

$$G'' = G^* \sin\delta \tag{2.11}$$

Yielding G', the storage modulus, which represents the deformation energy stored, and G'', the loss modulus, representing the deformation energy dissipated during flow. Note that the value of G' in the linear region at low shear strain is equivalent to the elastic shear modulus G of solid materials (del-Mazo-Barbara and Ginebra, 2021).

One of the key aspects in direct ink writing rheology is that the ink must satisfy two requirements (Smay et al., 2002; Feilden et al., 2016, 2017). First, shear thinning behaviour is required, i.e. the viscosity $\eta = \tau/\dot{\gamma}$ of the ink must decrease with increasing shear stress. Second, a storage modulus at rest or 'stiffness' greater than 10 kPa is required, in addition to a yield point greater than 50 Pa, so that the filaments retain their shape upon deposition. Both of these aspects are defined in fig. 2.4. Given the relevance to understanding the inks formulated in this thesis, these plots are provided in abundance throughout this report.

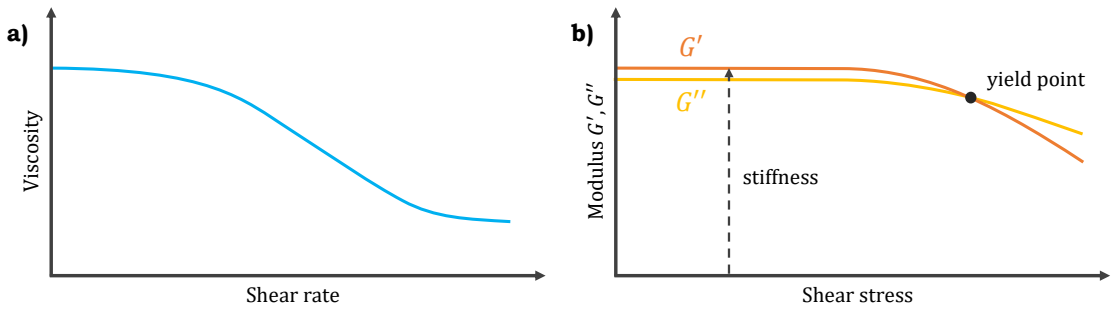

Figure 2.4: Example rheological plots demonstrating shear thinning in a so-called 'flow sweep' plot **(a)** and measurement of stiffness and yield point in an 'amplitude sweep' plot **(b)**.

2.3. Shear-induced alignment in direct ink writing

A specific rheology-related phenomenon, also critical to the work of this thesis, is that of shear-induced alignment. As explained by Feilden et al. (2017), a small, non-spherical colloid such as a short fibre or platelet, when placed in radially-aligned fashion in a flow containing a velocity gradient, experiences a torque as depicted in fig. 2.5. As the colloid aligns length-wise with the flow, the torque diminishes, leading to a general preference towards the flow-aligned state. In this state, colloids are also able to pack more densely, possibly constraining their movement and stabilising the stacked orientation. This stacked alignment typically facilitates shear thinning in colloidal suspensions (Anton Paar, 2024).

The phenomenon can be leveraged to align platelets in the direction of printing in DIW. In that case, a radial velocity gradient forms in the nozzle as a result of the zero flow velocity (no-slip) condition at the solid nozzle wall in combination with a non-zero flow velocity in the centre, allowing facile assembly of nacre-like filaments as demonstrated by Feilden et al. (2017).

Feilden et al. (2017) estimated the velocity profile and compared this to SEM cross-sections of printed filaments to predict and quantify the alignment of platelets. According to the authors, the rheology of a paste used for DIW can be appropriately described by the Herschel-Bulkley model (Herschel and Bulkley, 1926):

$$\tau = \tau_y + K\dot{\gamma}^n \tag{2.12}$$

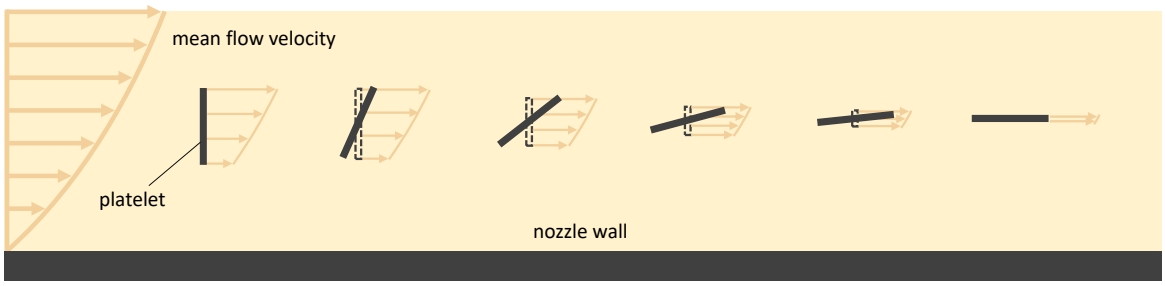

Figure 2.5: Detailed illustration of the shear-induced alignment mechanism.

Here, K is the consistency parameter describing the general 'thickness' of the fluid, and n is the 'flow behaviour index', which gives shear thinning behaviour for values less than unity. Assuming a uniform channel with a circular cross-section and applying eq. (2.12) to the Navier-Stokes equations, the velocity profile can be estimated as follows (Peker and Helvaci, 2008):

$$V(r) = \frac{nR}{\tau_w(n+1)}\left(\frac{1}{K}\right)^{\frac{1}{n}}\left[\left(\tau_w - \tau_y\right)^{\frac{n+1}{n}} - \left(\frac{\tau_w r}{R} - \tau_y\right)^{\frac{n+1}{n}}\right] \tag{2.13}$$

where R is the total radius of the channel and τ_w the wall shear stress, which is calculated from the pressure drop ΔP across the length of the nozzle:

$$\tau_w = \frac{R\Delta P}{2L} \tag{2.14}$$

Where L is the length of the nozzle. Differentiating gives the radial velocity gradient, which is a measure for the rate of shear alignment (Feilden et al., 2017):

$$\frac{dV(r)}{dr} = \left(\frac{1}{K}\right)^{\frac{1}{n}}\left[\left(\frac{\tau_w r}{R} - \tau_y\right)^{\frac{1}{n}}\right] \tag{2.15}$$

The results obtained by Feilden et al. (2017) are compiled in fig. 2.6.

Using these approximations, the authors find a proportional relation between the extent of platelet alignment and shear rates in the nozzle. They quantify this extent via a 'relative core radius', the ratio between the effective diameter of the misaligned core (determined via SEM) over the total filament diameter, with smaller ratios meaning a higher proportion of aligned platelets. This implies that alignment occurs radially inwards, which agrees with the expectation that it should occur fastest where the velocity gradient is highest (at the nozzle wall). In addition, the relative core radius was found to be independent of nozzle diameter (except for very small nozzles), and to decrease for increasing nozzle lengths. This implies that alignment has not reached equilibrium within the nozzle or that complete alignment is impossible.

The authors suggest that a given nozzle length represents a certain point in time in reaching equilibrium as overlaid in fig. 2.6f. Notably, the shape of the velocity profile and the time evolution of the core radius imply a convergence towards a non-zero value, intuitively, the span of r/R where $dV/dr \approx 0$. More data would be necessary to confirm this. This point is revisited in chapter 5.

2.4. Design principles of artificial nacre

The point of shear-induced alignment is to replicate nacre's layered microstructure, which is a subset of the larger aim of mimicking nacre's toughening behaviour as described in section 1.4. To understand which geometric factors govern the replication of these mechanisms, guidelines from literature are summarised below.

Briefly, based on the analyses of Currey (1977) and Glavinchevski and Piggott (1973), the ultimate tensile strength σ_c of a nacre-like hybrid material, assuming a matrix yield shear strength smaller than the matrix-platelet interfacial strength ($\tau_i > \tau_y$), can be estimated using (Bonderer et al., 2008):

$$\sigma_c = \alpha V_p \sigma_p + (1 - V_p)\sigma_m \tag{2.16}$$

Here, V_p is the platelet volume fraction, σ_p and σ_m the tensile strengths of the platelet and matrix, respectively, and α a factor based on the platelet aspect ratio s, the matrix yield shear strength τ_y, and σ_p. The

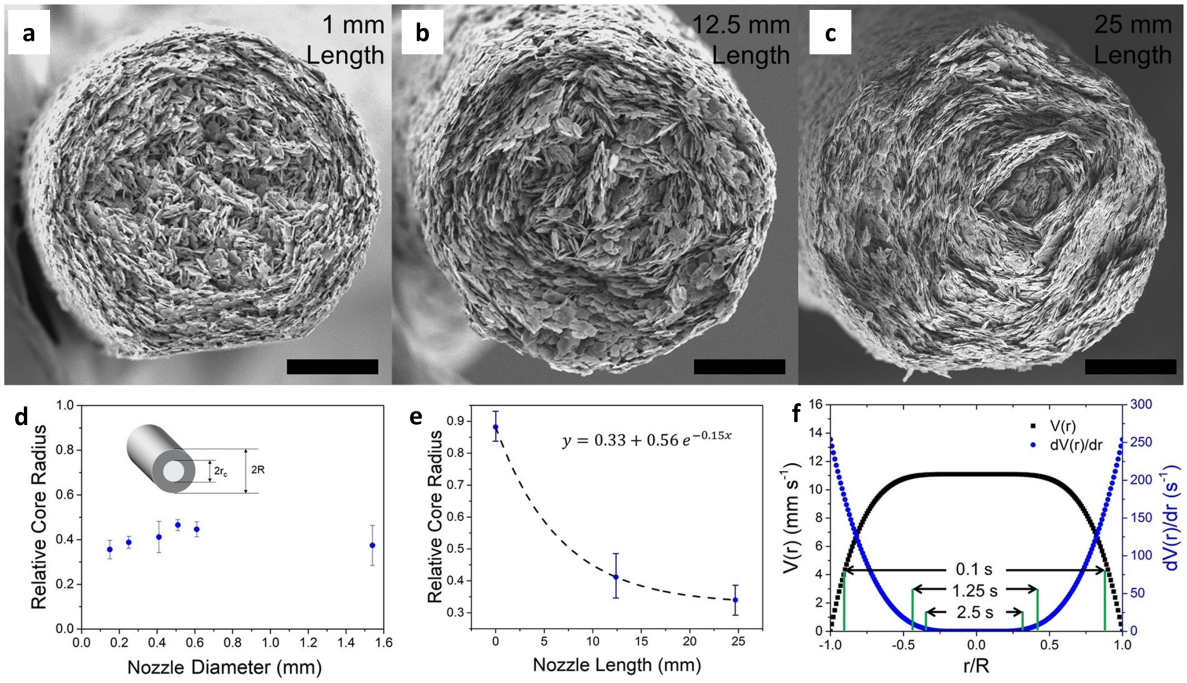

Figure 2.6: Filament micrographs and degrees of shear-induced alignment observed by Feilden et al. (2017) **(a-e)** and comparison to theoretical velocity distribution **(f)**. Scale bars **(a-c)** are 30 µm.

calculation of α depends on the failure mode, which is governed by the aspect ratio of the platelets. A certain threshold value s_c indicates this failure mode and is defined by

$$s_c = \frac{\sigma_p}{\tau_y} \tag{2.17}$$

For $s > s_c$, the platelets fail before the matrix yields, leading to brittle behaviour, for which α is given by:

$$\alpha = 1 - \frac{\sigma_p}{2\tau_y s} \tag{2.18}$$

For aspect ratios giving $s < s_c$ the opposite occurs, allowing for the primary toughening mechanisms to take place as described in section 1.4. The value of α is then given by:

$$\alpha = \frac{\tau_y s}{2\sigma_p} \tag{2.19}$$

In the case that the interface strength τ_i is smaller than the matrix yield shear strength ($\tau_i < \tau_y$), τ_y must be replaced by τ_i in eqs. (2.18) and (2.19). The platelets found in natural nacre, unsurprisingly, result in a value of s slightly lower than s_c (Currey, 1977). In addition to this criterion, Barthelat et al. (2007) provide 7 design guidelines for mimicking nacre's toughening behaviour:

1. Tablets should be stiff and have high tensile strength;
2. Interface should be much softer and more deformable than the tablets;
3. Interface should have high compressive stiffness and high compressive strength in out-of-plane direction
4. Tablets should be as thin as possible while avoiding tablet failure before sliding;
5. Tablets should be wavy in a dovetail-like fashion to generate the locking mechanism;
6. Tablet core area, interface tensile strength and tablet waviness should be finely tuned to maximise strength. Mineral bridges may aid in providing the required tensile strength in the core area.

Keeping these criteria in mind throughout the rest of this work provides a helpful perspective, especially when considering the results. A reflection of these points in the context of these results report is given in chapter 5.

3

Ink formulation

Building on the motivation and context outlined in chapters 1 and 2, this chapter addresses the first research objective: formulating and characterising an ink suitable for direct ink writing. The exploratory and iterative nature of ink formulation drives a trial-result-repeat structure consisting of three sections. Section 3.1 details the methods and results obtained for a preliminary composition based on readily available materials. In section 3.2, we move to a composition more representative of nacre and aligned with related research. This composition introduced challenges regarding rheology and printability, prompting a parametric study to understand its behaviour. The resulting improved ink formulation, discussed in section 3.3, serves as the basis for physicochemical characterisation in the following chapter.

The scope of the experimental work was narrowed by making some fundamental choices that shape the formulation approach. First, the ink formulation contains all final material, i.e. the printing process is a single-step extrusion of a suspension containing all mechanical elements. No material additions such as through vacuum infusion as used in the study by Feilden et al. (2017) are performed after printing. Second, for MICP to occur *in situ*, water is used as a solvent, and the necessary feedstocks for the bacteria are dissolved within it. Third, to obtain dry ceramic/polymer proportions close to that of nacre (95:5, respectively), a roughly similar ratio is taken as guideline. Last, solid fraction is maximised where possible to minimise shrinkage on solvent evaporation.

3.1. Preliminary: phyllosilicates and powdered chitosan

A preliminary formulation was composed using the above-stated constraints and readily available compounds in the laboratory. The same phyllosilicate (PS) mineral platelets used by Krüger (2022) to form a scaffold for bacterial cellulose production were used. The polymer, chitosan, was selected due to its commonality in nacre research (section 1.5), its resemblance to chitin (the biopolymer found in natural nacre), and its efficacy in past DIW experiments.

3.1.1. Methods

The preliminary ink was prepared by mixing the base components and media and inoculating the mixture with bacteria. Printing experiments were performed to generate samples and assess printability, followed by parallel plate rheology and scanning electron microscopy to observe microstructure and bacterial activity.

Preparation

First, powdered chitosan (PC) was mixed into 3.5 g of 1 wt% acetic acid solution and dissolved under vigorous manual stirring with a metal spatula and heating at 60 °C. Once dissolved, PS platelets were added in steps of 1 g, then homogenised by stirring manually until a viscosity deemed suitable by the eye was achieved. To this mix, 0.5 g of 8× concentrated biomineralisation (BM) medium was added containing 80 $g\,l^{-1}$ tryptone/peptone, 40 $g\,l^{-1}$ yeast extract, and 80 $g\,l^{-1}$ ammonium chloride, forming the main feedstocks for growth and proliferation. 120 mg of urea and 9 mg of calcium chloride dihydrate were added to allow MICP. The ink was then re-homogenised by speed mixing for 5 min at 3500 RPM. Finally, 70 µl of *S. pasteurii* glycerol stock stored in a freezer was melted and gently mixed into the ink using a glass stirring rod.

Immediately after inoculating, the ink was placed into a 20 ml luer lock syringe by removing the plunger, sealing with a luer cap and transferring the ink using a metal spatula. Centrifuging for approximately 1 min at 1000 rcf ensures the ink is pushed towards the tip and helps remove gas bubbles. The plunger is then moved back in using a long syringe needle to bypass the seal.

Assessing printability

Printability was assessed directly by printing rasters onto a microscope slide. Such rasters are commonly used to visually identify the defects customary of direct ink writing, such as (i) insufficient shape retention, (ii) corner rounding, (iii) filament sag, and (iv) slumping of the entire part (M'Barki et al., 2017; del-Mazo-Barbara and Ginebra, 2021). A syringe containing freshly prepared ink was fitted with an 18 ga (1.2 mm diameter) tapered nozzle and loaded into an Ultimaker UM2+ printer modified with a custom syringe extruder, as shown in fig. 3.1. The printer was instructed using a readily-available `.gcode` (appendix A.4) suited to this particular printer and nozzle type.

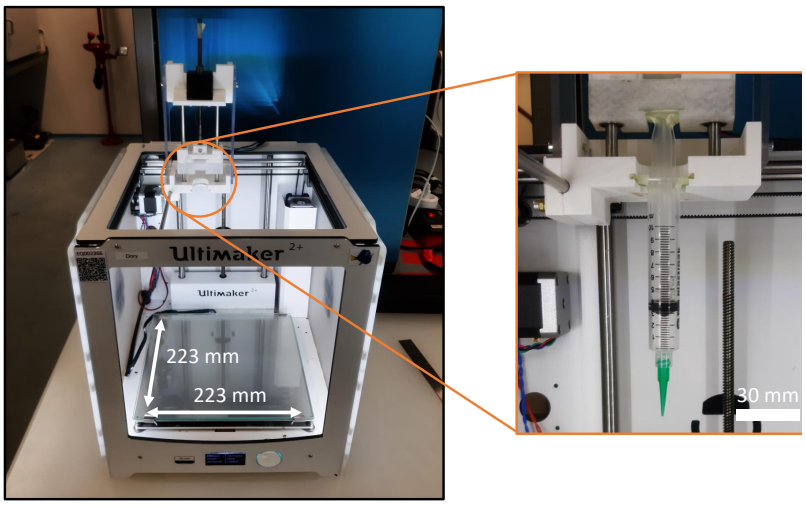

Figure 3.1: Ultimaker UM2+ printer fitted with custom syringe extruder for preliminary printing experiments.

Rheology

Two relevant predictors of printability are the yield shear stress τ_y and the stiffness at rest $\overline{G'}$ as described in section 2.2. These quantities were evaluated via amplitude and flow sweep curves. Samples were analysed using a rheometer housing serrated parallel plates 20 mm in diameter. These serrations help minimise wall slip, which is common for ceramic-loaded hydrogels (del-Mazo-Barbara and Ginebra, 2021). The same approach is generally used throughout this thesis: a 10 ml syringe containing the relevant ink is prepared in advance. The serrated plates are placed into the rheometer, and the inertia is re-calibrated. A small excess of ink (approx. 0.8 ml) is pushed onto the bottom serrated plate, after which the gap size is set to 1 mm and the excess trimmed off the circumference using a small spatula. To limit drying, which was found to be significant (fig. C.2), silicone oil is dripped over the circumference of the top plate and allowed to run down over the exposed sample edges, creating a barrier against moisture loss[1]. The process is shown in fig. 3.2.

[1] Ideally a solvent trap should be used, but this equipment was not available. Dutto et al. (2025) use the same method.

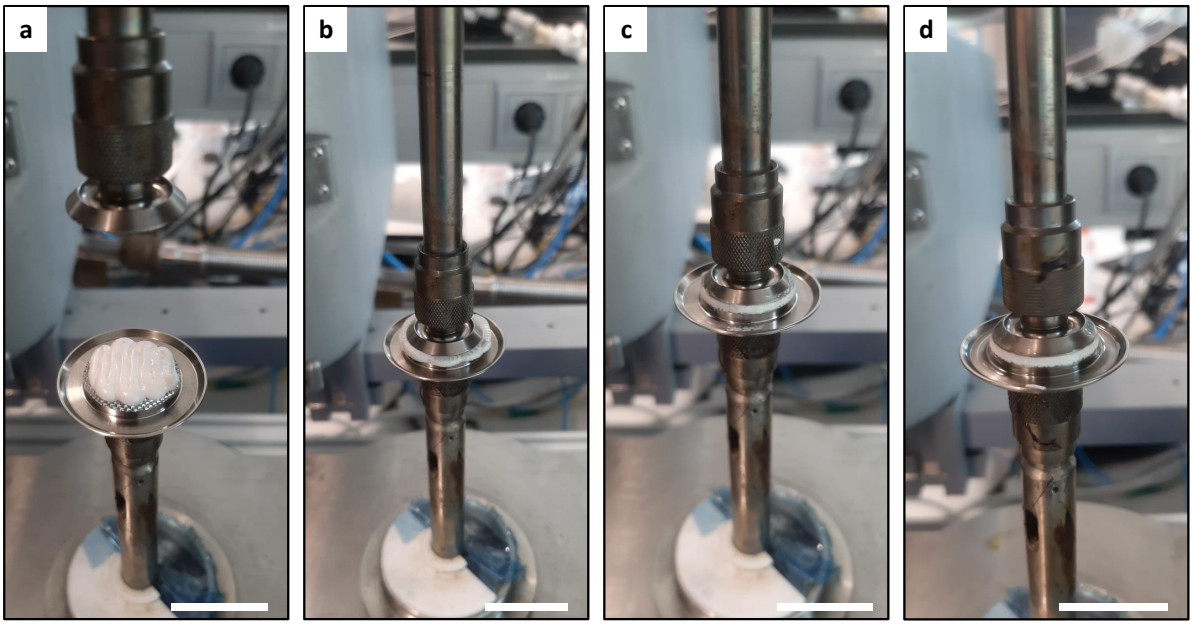

Figure 3.2: Sample preparation for rheological analysis. A small excess is added to the bottom plate **(a)**, after which the gap size is set **(b)**, and the excess is trimmed off **(c)**. The exposed surface is covered with silicone oil to reduce drying **(d)**. Scale bars are 20 mm (at the focal point).

Amplitude sweeps were carried out at ~20 °C in a stress-controlled ramp from 10 Pa to ~3000 Pa with approximately 15 points per decade, using a frequency of 1 Hz. The test is stopped manually after clear yielding. Flow sweep were carried out as 30 s linear ramps from 0.1–100 s^{-1}, sampled every 0.3 s.

The ink yield shear stress τ_y is then determined from the stress τ at which the phase lag δ first exceeds 45°. A lower limit of ~2 Pa is set to avoid false positives caused by noise at low shear stresses. This definition was found to be most suitable amongst other methods; the modulus crossover point is not adequate as some inks do not experience this crossover even after large viscosity drops associated with yielding, whereas the point of significant viscosity drop is difficult to establish for low viscosity inks.

Assessing bacterial activity and microstructure

To allow bacterial proliferation and MICP, a raster printed in section 3.1.1 was incubated for 12 h at 27 °C in a humidified Petri dish. The duration is based on the time required to achieve a majority (~60 %) of maximum precipitate yield in liquid media (Stocks-Fischer et al., 1999). While the precipitation rate is likely lower for highly viscous suspensions, where nutrient diffusion is reduced, this duration serves as an initial reference. After incubation, the sample was removed and air dried for 24 h, followed by freeze-drying by submerging in liquid nitrogen until boiling seizes and placement under vacuum (0.2 mbar) overnight. Upon removal, the sample was broken in half using tweezers and sputter coated in a sample holder using chromium (thickness ~5 nm) and placed in SEM. Imaging was performed at an acceleration voltage of 5 kV using the lower secondary electron detector (LEI) at different working distances in both low (LM) and high (SEM) magnification modes.

3.1.2. Results and discussion

This subsection presents the results of printability, rheology, and bacterial activity assessments for the PS/PC ink.

Printability

To begin, fig. 3.3 demonstrates the raster print obtained after direct ink writing the PS/PC ink. This preliminary composition demonstrates superb printability: filaments retain their shape and are not affected by the short overhangs, and other than some slight outwards sag observed for the bottom layers, the samples maintained their cubic shape over time. These positive results mean that high-fidelity coupons and filaments can be printed for characterisation.

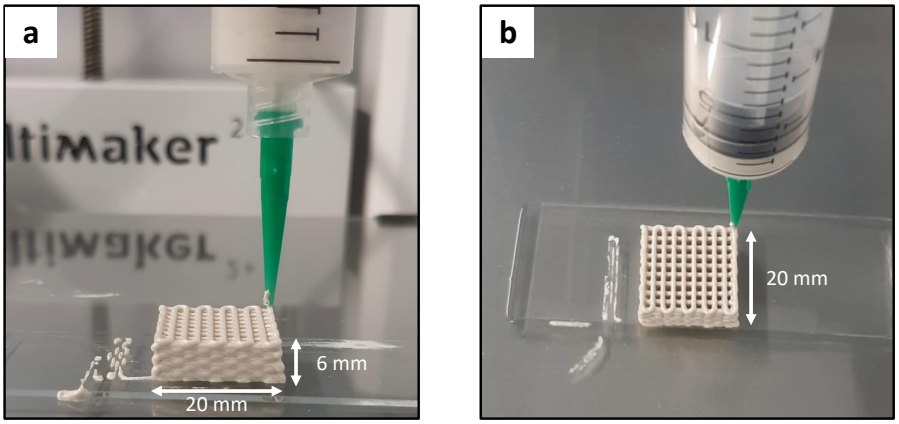

Figure 3.3: Print results of preliminary ink formulation demonstrating excellent printability. Two samples are printed using an 18 ga tapered nozzle, one viewed from the front **(a)**, and another from the top **(b)**.

Rheology

The resulting stress amplitude sweep and flow sweep curves for the phyllosilicate/chitosan ink are shown in fig. 3.4. Interestingly, despite the excellent printability, the storage modulus at rest does not satisfy the minimum set by Feilden et al. (2017), and shear thinning is observed only for the region $\dot{\gamma}$ >2 Pa. Note that from rest to extrusion speeds (~65 s^{-1}), the change in viscosity is still negative.

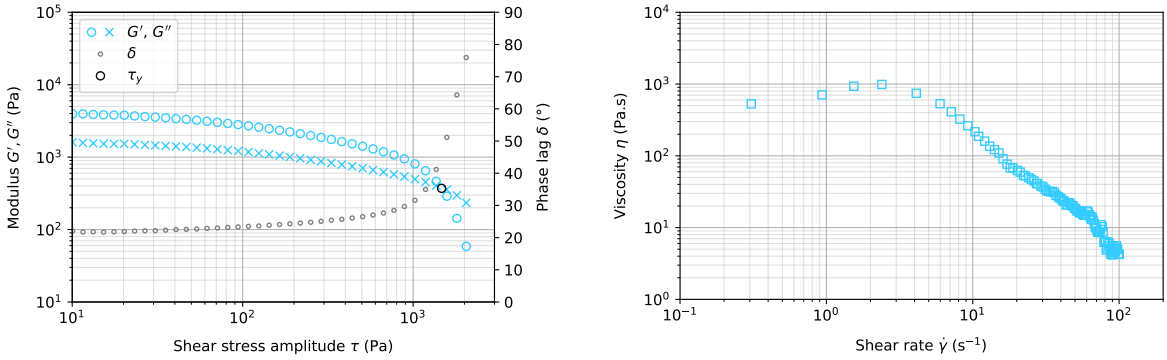

(a) Oscillatory stress amplitude sweep. The storage modulus at rest is about 4000 Pa. The yield point, denoted by the black circle, is approximately 1300 Pa.

(b) Shear rate sweep for the phyllosilicate/chitosan ink showing shear thinning behaviour above $\dot{\gamma} \approx 2\,s^{-1}$.

Figure 3.4: Results of rheological measurements performed on the phyllosilicate/chitosan ink showing only partial satisfaction of the rheological requirements set by Feilden et al. (2017) despite demonstrating excellent printability.

Bacterial activity and microstructure

Bacterial activity within the printed and incubated raster grid was qualitatively assessed through SEM by examining the filament microstructure to identify crystal formations and rod-shaped bacterial structures comparable to those in fig. 2.2. Additionally, the filament microstructure can be qualitatively assessed. The resulting micrographs are shown in fig. 3.5.

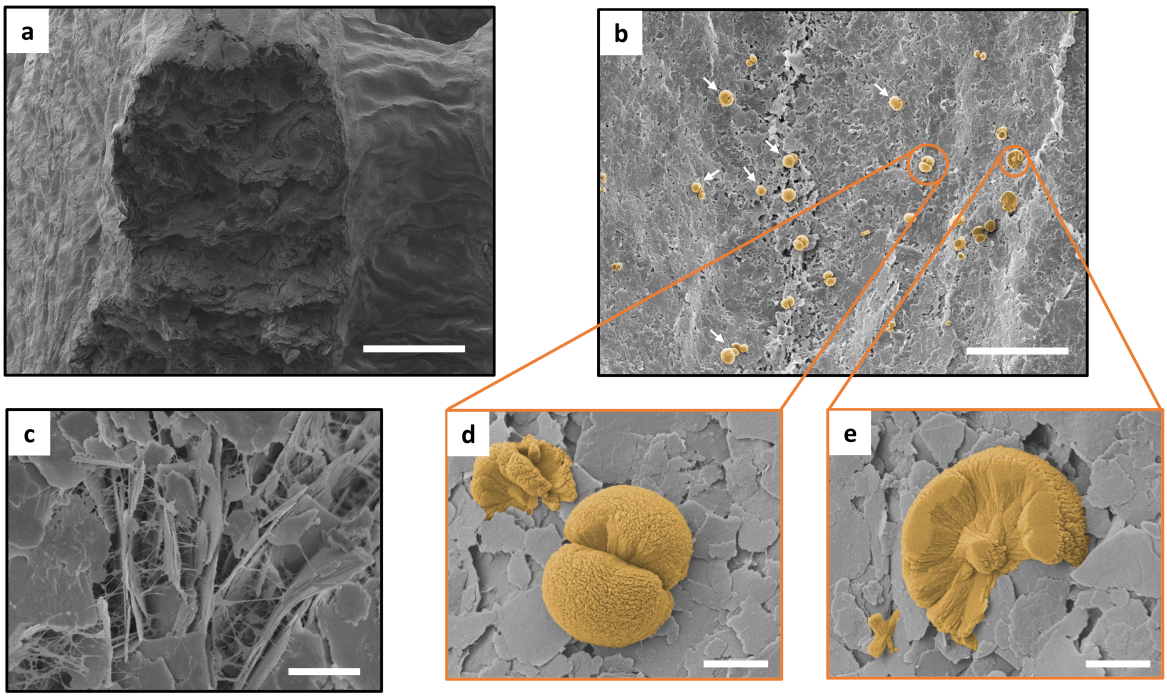

Figure 3.5: False-coloured SEM images of a freeze-dried sample printed using preliminary ink formulation. Cross-section of top-layer filament **(a)**, $CaCO_3$ deposits (yellow) on the print surface highlighted by the arrows **(b)**, close-up of filament cross-section **(c)**, and close-ups of two marked $CaCO_3$ deposits **(d-e)**. Scale bars are 500 µm **(a)**, 100 µm **(b)**, and 5 µm **(c-e)**.

Observing fig. 3.5, the overall filament structure (fig. 3.5a) appears to be well-compacted, that is, despite a significant water content of 53 wt% that is removed during freeze drying, no large void content or porosity is immediately apparent. At smaller scales (fig. 3.5b-e), porosity becomes visible at the junctions between filaments and between platelets. Filament internal structures are disordered with no clear sign of platelet alignment, although this can be expected considering the low nozzle aspect ratio used.

More importantly, on the print surface, distinct sphere-like deposits are visible. These are in the expected size range of *S. pasteurii* (1–10 µm) and resemble the typical morphology of vaterite grown via MICP, thereby presenting clear evidence of bacterial activity. Such deposits could not be distinguished within filament interiors. These observations are further addressed in section 3.1.3.

3.1.3. Increasing bacterial activity

The most apparent reason for the lack of precipitation or bacteria observed in the filament interiors is the lack of oxygen, limiting the growth and proliferation of *S. pasteurii* as described in chapter 2. However, other phenomena could lead to the same observation: (i) the topology of the internal microstructure can hinder precipitation or the ease at which it may be visually identified within the disordered filament structure, (ii) bacterial content may be too low, as a result of insufficient starting concentration, (iii) bacterial proliferation still be possible but limited by a factor other than oxygen concentration, (iv) bacterial distribution may be insufficiently homogeneous, leading to regions of high deposition (e.g. fig. 3.5b) and regions without, and (v) the preparation or the printing process may significantly reduce cell viability due to aggressive changes in pH, osmotic shock, or excessive shear.

The topological constraining, mobility of the bacteria and the diffusion rate of nutrients and oxygen are two factors inherent to this approach and, therefore, cannot be alleviated. However, the starting concentrations of both the bacteria and the nutrients can be increased, and homogeneity can be improved by mixing for longer durations or speed mixing. However, the latter may introduce excessive shear forces and should thus be carried out at low speeds. MICP may still occur at zero viability since the urease enzyme responsible for MICP remains present. Similarly, the arguments in (v) are presumed to be a lesser factor since *S. pasteurii* is highly resilient to extreme conditions (Anbu et al., 2016). Assuming sufficient nutrient content, three cases are possible for the low occurrence of MICP: (i) In the case of adequate cell density but insufficient viability, MICP should still be observable as long as the urease remains. (ii) In the case of low cell density but high

viability, bacteria will proliferate to induce MICP. (iii) In the case of low cell density and low viability, no MICP will be observed, but this can be ameliorated by increasing cell density. Therefore, in all three cases, MICP should be achievable by ensuring sufficiently high bacterial density.

As a result, the ink was resynthesised with increased bacterial density. Calcium content was also increased due to a mistakenly low (albeit sufficient) concentration. Urea and $CaCl_2 \cdot 2\,H_2O$ were added in solution rather than directly as a solid to improve homogeneity. Bacterial volume was increased simply by increasing the amount of glycerol stock from 70 µL to 1 mL. The change in the solid fraction was compensated by increasing the platelet volume fraction until printability reached satisfaction.

Samples printed using this formulation were placed under SEM, but no bacteria were found within the filament. As such, another ink was prepared with a greater step in bacterial density: first, 20 µL of *S. pasteurii* glycerol stock was added to 250 ml of fresh growth medium and incubated for 48 h. Upon removal, 50 mL of the inoculum was centrifuged at 6000 rcf for 10 min, after which the supernatant was decanted until ~5 mL of medium remained, representing a 10-fold concentration. The pellet was resuspended by vigorous shaking, after which 1 mL of this inoculate was added to the ink instead of the glycerol stock.

Remarkably, the ink was not printable because it solidified within 10 min after adding the inoculum, turning into a crumbly, rubbery texture. Crucially, this is linked to pH change, a detail not appreciated in this experiment but which shall be returned to in chapter 5. Nevertheless, to allow a more extended time window for printing, the growth medium inoculum was reduced to base concentration (1-fold). The resulting ink remained unprintable, clogging the nozzle within 10 min after starting printing. Finally, diluting the inoculate to 0.5× allowed a sample to be printed. Note that this ink still solidified after 30 to 90 minutes.

Following incubation for 96 hours, placing these 0.5× inoculated samples under SEM revealed no distinct minerals inside filaments. However, it showed an increase in mineral crystal size and spatial density on the surface as shown in fig. 3.6a, in addition to a large number of flattened, rod-shaped elements covering the entire print, shown in fig. 3.6b. These rod-shaped elements are presumed to be bacteria flattened during drying or otherwise. Note that the mineral crystals resemble a different polymorph of calcium carbonate, calcite, recognisable by the cube-like crystals and associated with a higher metabolic activity of *S. pasteurii* (Saracho et al., 2020).

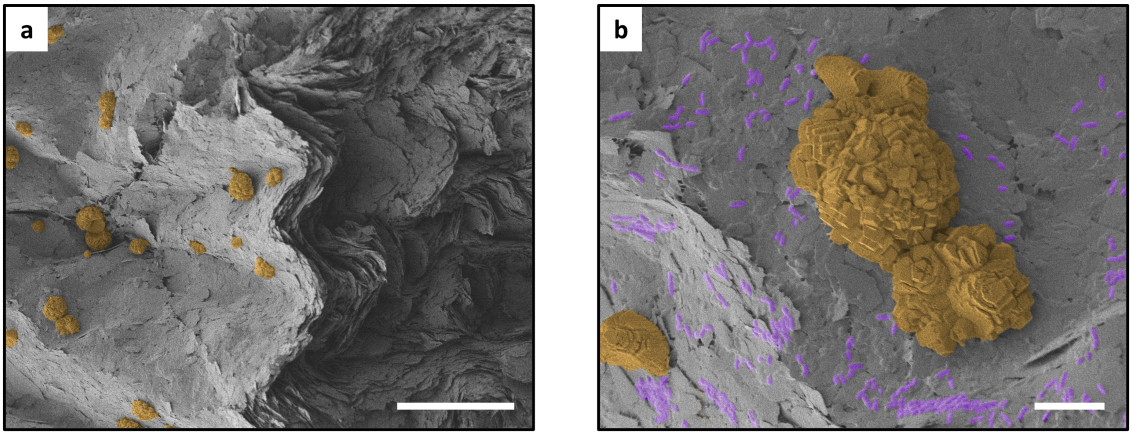

Figure 3.6: False-coloured SEM images of a sample obtained from the second ink formulation containing 1 mL of concentrated inoculate, showing large calcite deposits (yellow) **(a)** and surface extensively covered in flattened, rod-like elements resembling bacteria (purple, only a number have been coloured) **(b)**. Scale bars are 100 µm **(a)** and 10 µm **(b)**.

Compared to The density of mineral deposits, the density of bacteria observed in fig. 3.6 implies that many bacterial cells in the ink are either unviable or inactive. Whether this is the cause of toxicity, mechanical death, cellular processes, nutrient unavailability, or otherwise remains unclear. The lack of precipitates observed within the filament suggests that MICP either does not occur or cannot be identified using the current qualitative assessment via SEM. Nevertheless, the extensive outside coverage may noticeably impact material properties. As a result, we move to the next stage. The resulting composition and accompanying preparation protocol can be found table 3.1 and appendix C.1, respectively.

Table 3.1: Preliminary ink formulation containing 40.4 wt% phyllosilicate platelets. The concentrations in the fourth column are relative to the water content in the bottom row. *S. pasteurii* was added as 1 mL of 0.5x diluted growth medium inoculum.

Substance	Quantity (mg)	Wet wt%	Wet vol%	Concentration	
Silicate platelets	20,000	40.4	20.4	-	
Chitosan; powdered (PC)	750	1.53	2.07	27.6	$\mathrm{mg\,ml^{-1}}$
Acetic acid	250	0.51	0.66	153	$\mathrm{mmol\,l^{-1}}$
Tryptone/peptone	120	0.24	0.68	4.5	$\mathrm{mg\,ml^{-1}}$
Yeast extract	60	0.12	0.33	2.2	$\mathrm{mg\,ml^{-1}}$
Ammonium chloride	120	0.24	0.22	82.9	$\mathrm{mmol\,l^{-1}}$
Urea	600	1.22	1.25	374	$\mathrm{mmol\,l^{-1}}$
Calcium chloride dihydrate	441	0.90	0.66	112	$\mathrm{mmol\,l^{-1}}$
Water	26,732	54.9	73.7	-	
Total	49,541				

3.2. Nacre-inspired: alumina and high molecular weight chitosan

Despite obtaining a printing and biomineralising composition using PS/PC, practical changes to the experimental approach were necessary. First, the phyllosilicate platelets were not believed to be representative of the microstructure and deformation behaviour of nacre. To explain, mica and kaolin, the constituent phyllosilicate minerals, consist of sheet-like molecular structures that stack in a layered fashion, bonded weakly by potassium ions and hydrogen bonding (Kumari and Mohan, 2021). Critically, this weak bonding facilitates sliding under shear when wet, causing the bulk platelet to deform as a whole rather than forming a stiff, high-strength backbone that promotes deformation through shearing of the polymer matrix. Consequently, I suspect that the deformation during extrusion is dominated by crystal sheet sliding rather than by bulk platelet movement (which allows alignment) and polymer shear. With this motivation, PS platelets were replaced by stronger, stiffer alumina (Al_2O_3) platelets, which also happen to be more commonly used across the techniques covered in section 1.5. SEM images comparing the platelets are shown fig. 3.7.

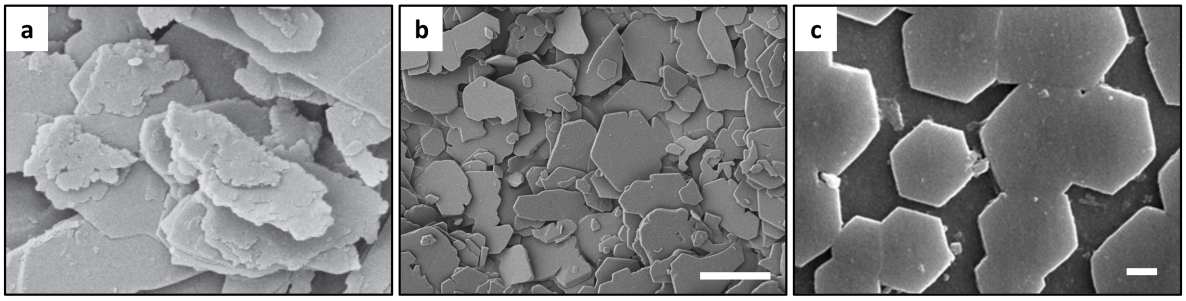

Figure 3.7: Scanning electron micrographs depicting geometrical differences between platelet types. Phyllosilicate platelets (**a**), consisting of clay-like mica and kaolin, are made up of sheet-like structures of repeating $[Si_{2n}O_{5n}]^{2n-}$ anions bridged by metal cations and hydrogen bonds. Scale unknown, platelet diameter in the order of 25 µm (Merck KGaA, 2019). Stiffer and stronger alumina platelets (**b**) with slightly more defined polygonal shapes. Scale bar 10 µm. Image courtesy of N.S. Guevara-Sotelo. Natural nacre from the Chinese pond mussel (*Sinanodonta woodiana*) (**c**), taken from Kalesaran and Lumenta (2021). Scale bar 1 µm.

A second change in approach was, unfortunately, of purely practical motive. Because the quantities of remaining powdered chitosan were insufficient, and because this particular type could not be re-ordered, the powdered chitosan (PC) was replaced by a high-molecular-weight chitosan (HMWC) variant from a different supplier. The effect of this change was evident and is considered later in this section.

3.2.1. Methods

Generally, the same methodology was used as for preparing and assessing the preliminary ink. Here, only deviations from it are stated. In particular, since alumina has a higher density ($3.99\,\mathrm{g\,cm^{-3}}$) than mica/kaolin ($\sim 2.7\,\mathrm{g\,cm^{-3}}$), the weight fraction was adjusted to match the volume fraction by increasing platelet content. A newer, slightly more user-friendly Creality Ender-3 V2 printer housing similar modifications to the extrusion module replaced the UM2+, depicted in fig. 3.8. The short, tapered 18 ga nozzle was replaced by a 38.1 mm

length, 0.508 mm diameter steel straight-barrel nozzle, matching roughly in aspect ratio (74.7) the longest nozzle used by Feilden et al. (2017) (61.0). This high aspect ratio ensures that printing occurs in a regime where shear forces are likely relevant. Tailored `.gcode` instructions were generated using a parametric script created using the Python FullControl package. The script can be found via appendix A.4. A test print was conducted using the PS/PC ink to confirm that the modifications affect results, yielding no qualitative difference.

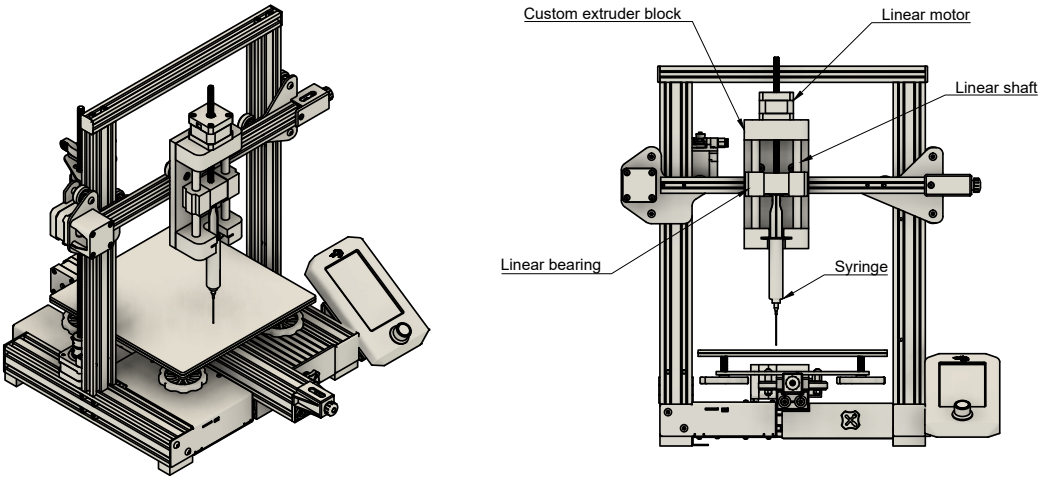

Figure 3.8: Creality Ender-3 V2 with custom print module for direct ink writing. Build plate is 235 × 235 mm.

3.2.2. Results and discussion

This subsection assesses the printability and rheology results of the Al_2O_3/HMWC ink for the same volume-wise composition as the PS/PC ink.

Printability

A raster 17 × 17 nozzle diameters in size (approx. 8.7 × 8.7 mm), was printed as previously (fig. 3.9). The result is shown in fig. 3.10.

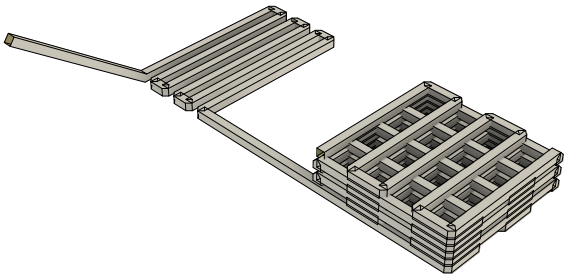

Figure 3.9: Model of raster print as generated using the FullControl package showing primer or 'lead-in' lines followed by a cubic grid structure.

Figure 3.10: Raster print result for Al_2O_3/HMWC mixture using the same volume-wise composition as the PS/PC mixture, showing significantly reduced print fidelity. 50 % print speed (500 mm/ min). Image size is approximately 10 × 10 mm.

Surprisingly, the Al_2O_3/HMWC ink demonstrates strongly reduced printability compared to the PS/PC ink. Since the process and volume-wise composition have essentially remained the same, the difference must be related to drastic changes in rheological behaviour at the molecular scale. A more in-depth discussion of the possible factors is made in chapter 5.

3.2.3. Rheology

Amplitude sweep and flow sweep curves, shown in fig. 3.11, support the reduction in printability. First, a significant decrease in storage modulus and yield point is observed. $\delta > 45°$ for the entire measurement range, meaning that the ink is fluid at rest. Second, a different shear thinning response is observed, having a less pronounced drop than for PS/PC ink, although an approximately similar magnitude change occurs across the measurement range. Note that this measurement range matches roughly the change in mean shear rate from rest to those expected during printing (~65 s^{-1}).

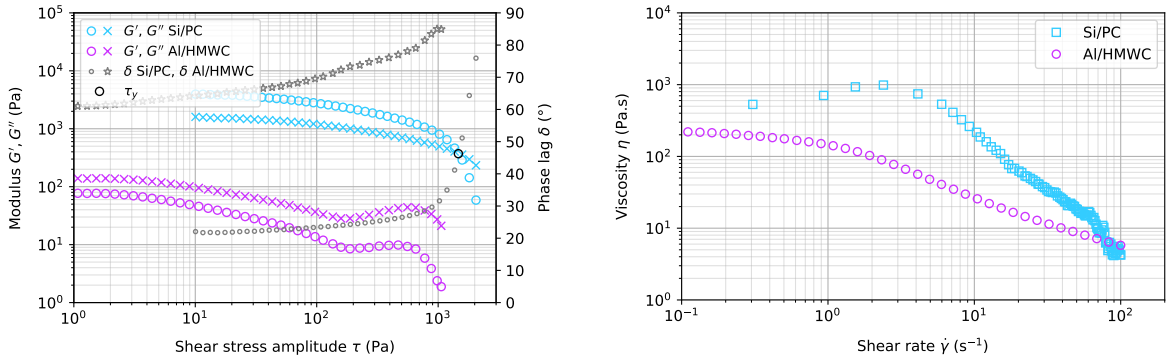

(a) Oscillatory stress amplitude sweep for the Al_2O_3/HMWC ink and comparison to PS/PC ink. Gap size 1 mm, sealed with silicone oil.

(b) Shear rate sweep for the Al_2O_3/HMWC ink and comparison to PS/PC ink. Gap size 1 mm, sealed with silicone oil.

Figure 3.11: Rheology of Al_2O_3/high molecular weight chitosan (HMWC) ink compared to phyllosilicate/powdered chitosan (PS/PC) ink.

3.2.4. Exploring compositional changes

Improving an ink formulation can be as simple as altering constituent balance, such as platelet or chitosan content. Given the reduction in storage modulus, loss modulus, and milder viscous response, an intuitive step would be to increase platelet or polymer content. Additionally, the shear rate can significantly affect the rheology of colloids, and since it is easily varied by altering printing speed, it is worthwhile to investigate its impact. In this subsection, these variations are assessed.

Compositions containing varying platelet and chitosan volume fractions were printed at different speeds. Rasters 17 × 17 nozzle diameters in size (approx. 8.7 × 8.7 mm) were printed onto microscope slides and imaged, followed by rheological assessment by measurement of stress amplitude and shear rate responses as before. The nutrients (tryptone/peptone, yeast extract, etc.) have been left out during preparation to decrease complexity and increase efficiency. The effect of their reincorporation is assessed later in this chapter.

Printability of varying compositions

Printability results are shown in figs. 3.12 and 3.13. Starting with the variation of polymer content in fig. 3.12, we can draw a few immediate observations. Print speeds below 50% yield the best results for all chitosan concentrations, although print fidelity is generally low and insufficient to print accurate shapes for mechanical testing. At 50%, there appears to be underextrusion for all chitosan concentrations, which is, to some degree, identifiable at lower print speeds in the form of corner rounding. Underextrusion may suggest that the printer is at the limit of the pressure it can provide for extrusion. Indeed, at higher print speeds, this underextrusion worsens until the extruding stepper motor stalls. Not immediately apparent from the images but clear to the eye is that all grids sagged in the overhangs despite the relatively small dimensions of the print, pointing to insufficient stiffness or yield stress for all compositions.

As for variation with chitosan content, fidelity improves with higher concentration, with the best results obtained at 3.31 vol%. Above this, however, the extruder motor stalls at all print speeds, implying that viscosity increases significantly with chitosan content or that a transition occurs from thinning to shear thickening behaviour. Therefore, such high concentrations should preferably be avoided.

Moving to the variation of platelet content in fig. 3.13, we observe again generally low fidelity and similar behaviour regarding print speed. A slightly improving fidelity is obtained for higher speeds, albeit tending towards underextrusion. As for the platelet content, no clear conclusions can be drawn.

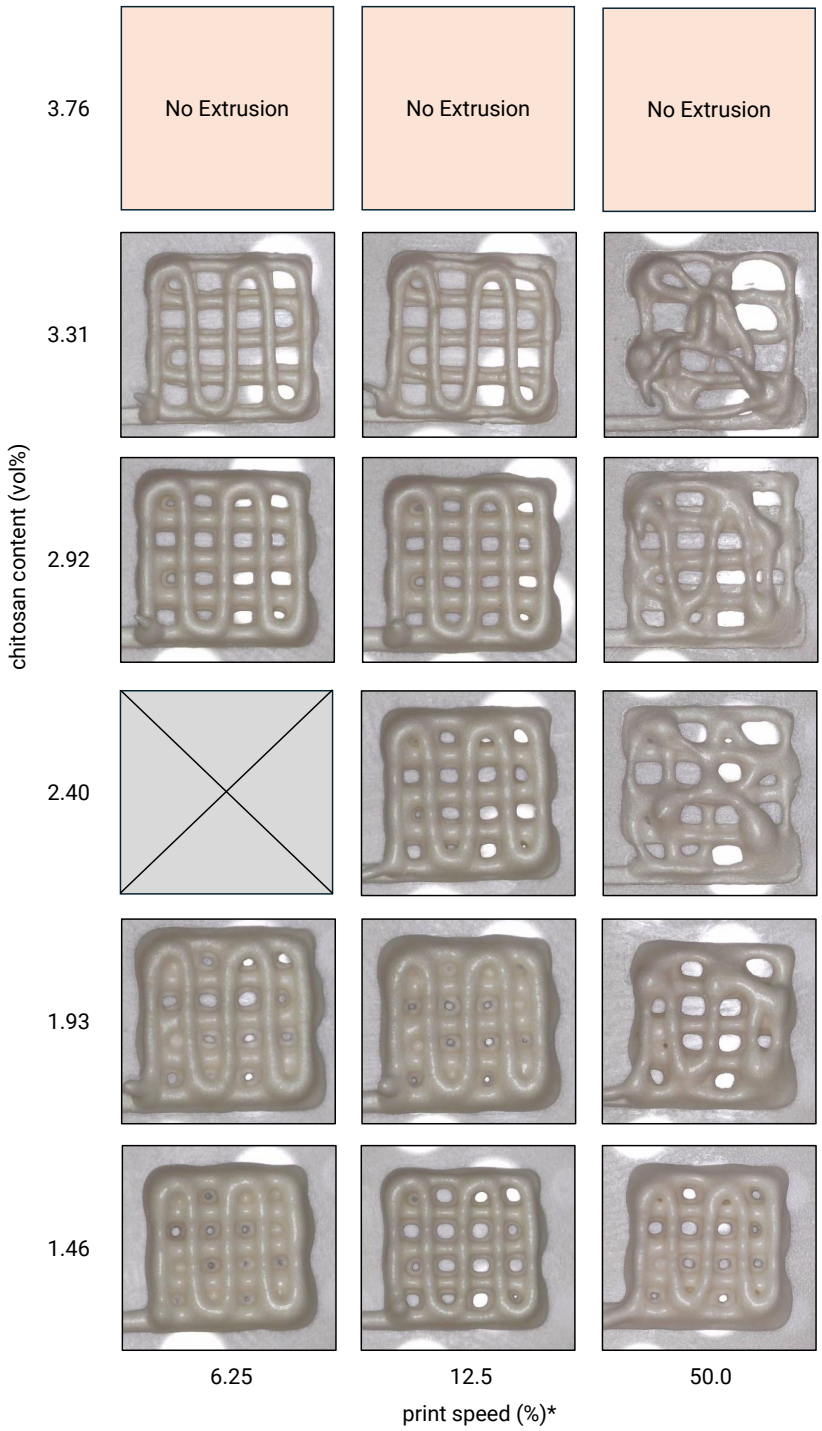

Figure 3.12: Raster print fidelity for varying chitosan content and print speed in Al_2O_3/HMWC inks. Platelet content remains approximately constant at (25.5 ± 0.4) vol%. Crossed-out grey squares denote data lost to corruption. Each square is approximately 10×10 mm. *100% print speed equates to 1000 mm/min.

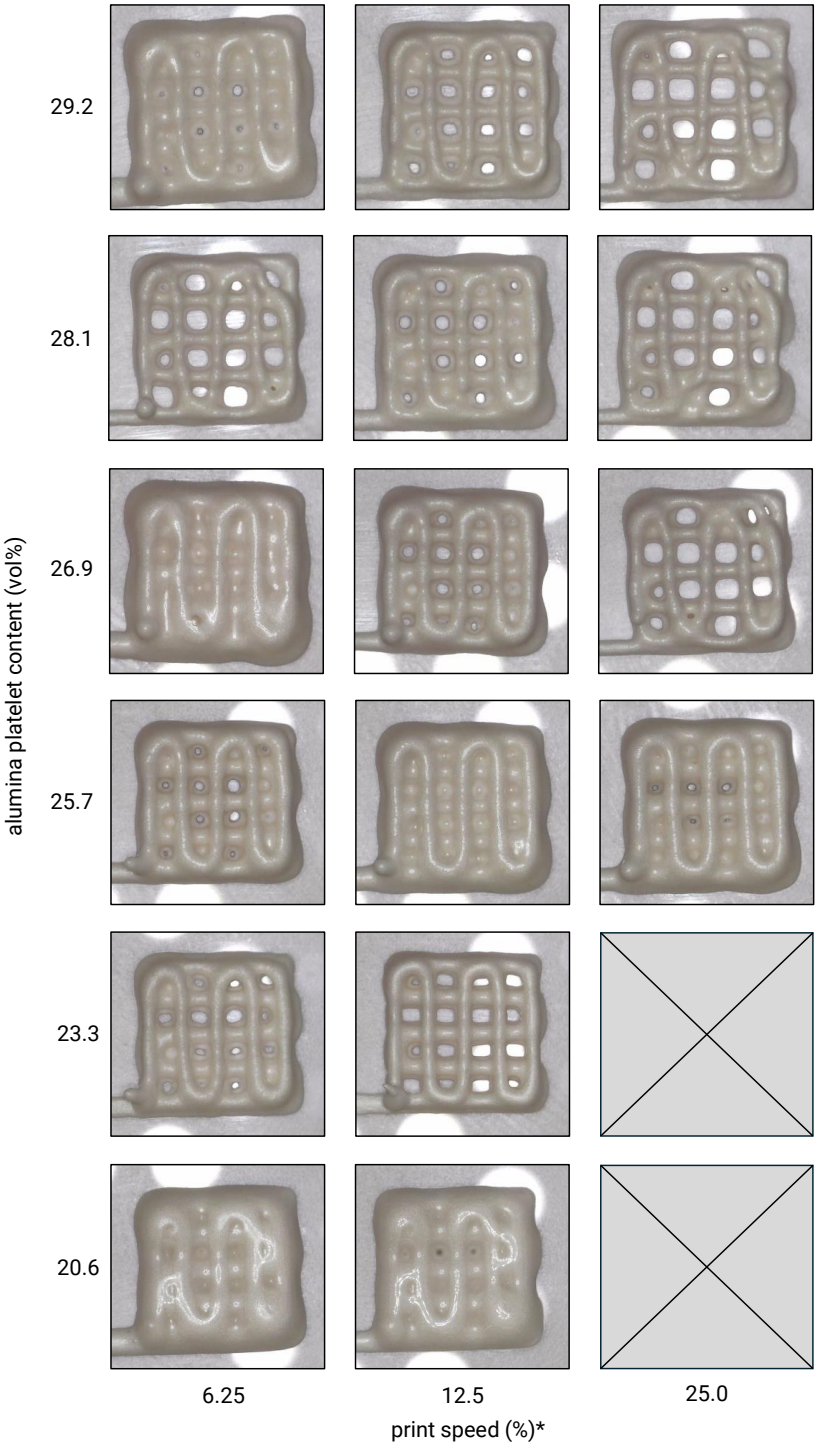

Figure 3.13: Raster print fidelity for varying platelet content and print speed in Al_2O_3/HMWC inks. Chitosan content remains approximately constant at (1.9 ± 0.1) vol%. Crossed-out grey squares denote data lost to corruption. Each square is approximately 10×10mm. *100% print speed equates to 1000 mm/ min. Inks containing 30.2 vol% alumina and above showed severe underextrusion (data not shown).

Rheology of varying compositions

To further understand the effects of the constituent changes, amplitude sweep and flow sweep tests were performed on all compositions. Storage moduli at rest were calculated for each measurement set by averaging the linear region, and the yield points were obtained as before. For each amplitude sweep, five repeat measurements were conducted to draw statistics; the raw data can be found in appendix D. The compiled results

are summarised in figs. 3.14 to 3.16.

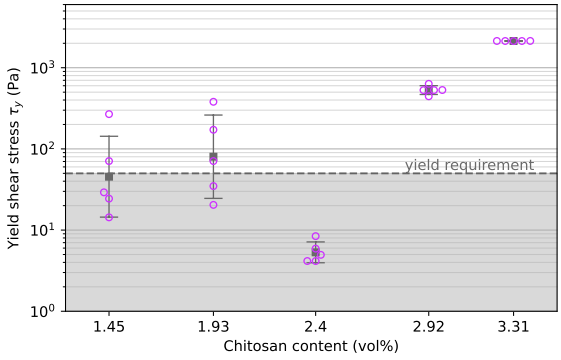

(a) Ink yield shear stress for varying chitosan content.

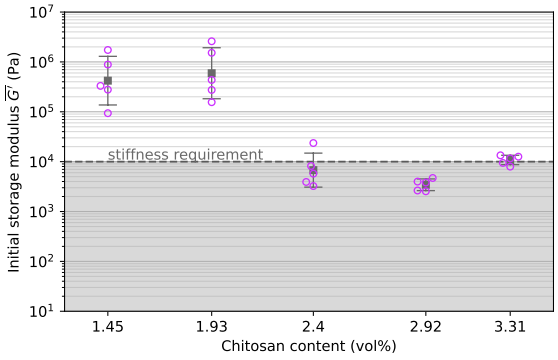

(b) Ink storage modulus for varying chitosan content. Each point represents a mean evaluated over each amplitude sweep curve's initial, approximately flat portion (appendix D).

Figure 3.14: Influence of chitosan content on ink yield shear stress and storage modulus. Platelet content is set at (25.5 ± 0.4) vol%. A non-linear relationship is observed in both yield stress and stiffness ($p > 0.05$ for a linear relationship), contrasting to that expected for a typical hydrogel (del-Mazo-Barbara and Ginebra, 2021). The shaded regions delimited by dashed lines depict the compositions not satisfying the rheological requirements set by Feilden et al. (2017). Note that points are scattered slightly to prevent overlap, but each label has the same vol%. Statistics (mean, standard deviation) are evaluated in logarithmic space to prevent bias towards low values.

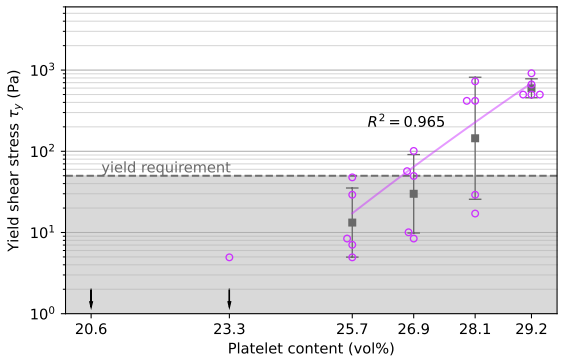

(a) Ink yield shear stress for varying platelet content. Arrows denote values falling below the starting point set for the measurement (i.e. yield at rest).

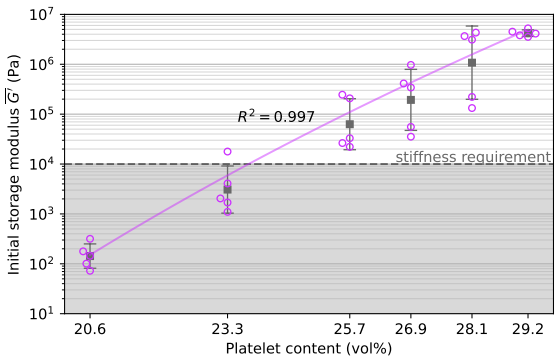

(b) Ink storage modulus for varying platelet content. Each point represents a mean evaluated over each amplitude sweep curve's initial, approximately flat portion (see appendix D).

Figure 3.15: Influence of platelet content on ink yield shear stress and storage modulus. HMWC content is set at (1.9 ± 0.1) vol%. A power-law relationship is observed for both yield shear stress ($p < 0.05$) and stiffness ($p < 0.05$), as expected for a typical hydrogel (del-Mazo-Barbara and Ginebra, 2021). The shaded regions delimited by dashed lines depict the compositions not satisfying the rheological requirements set by Feilden et al. (2017). Note that points are scattered slightly to prevent overlapping, but each label has the same vol%. Statistics (mean, standard deviation) are evaluated in logarithmic space to prevent bias towards low values.

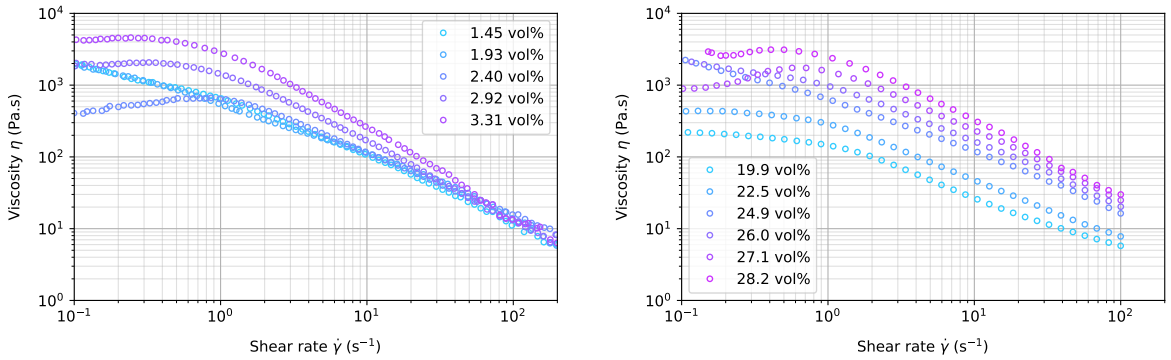

(a) Viscosity versus shear rate for varying HMWC content.

(b) Viscosity versus shear rate for varying platelet content.

Figure 3.16: Flow sweep responses for varying alumina and high molecular weight chitosan contents. Chitosan increases thinning behaviour accompanied by an upward shift, whereas alumina content only shifts the curves upwards. The shear rates expected during extrusion range from 16.3–130 s^{-1} for 6.25–50 % print speed, respectively.

Starting at fig. 3.14a, we observe a non-linear 'bucket-like' change in yield shear stress. This shape is somewhat unexpected. Statistical analysis supports the conclusion, with no significant difference between the first two points ($p = 0.46$) followed by a substantial decrease ($p < 0.002$) and an apparent increase.

Similarly shaped non-linear behaviour is observed for the storage modulus at rest shown in fig. 3.14b. No difference is observed from 1.45 vol% to 1.93 vol% ($p = 0.65$), followed by a significant decrease ($p < 0.00011$). No difference is present across 2.40 vol% and 2.92 vol% ($p = 0.11$), followed by a small increase for 3.31 vol% ($p < 7.7 \times 10^{-5}$).

The reason for these non-linear behaviours remains unclear. Avoiding ungrounded speculation, a more straightforward relationship is observed for the variation of platelet content: both yield point and storage modulus at rest appear to increase monotonically. However, no statistical difference is observed between 29.2 vol% and 30.2 vol% ($p = 0.11$), which may imply a maximum beyond this point.

Observing the flow rate responses in fig. 3.16a, we see increasing thinning behaviour for increasing HMWC contents accompanied by an upwards shift in viscosity, with all curves meeting approximately at 80 s^{-1}. Curiously, the curve transitions from a linear shape in logarithmic space to a plateaued shape. The reason for this is at this point also unclear, but is often related to the onset of a more defined yield point (del-Mazo-Barbara and Ginebra, 2021), which agrees with the results in fig. 3.15. Finally, in fig. 3.16b, we see a general upwards shift in viscosity with increasing alumina content, which agrees with results for a typical hydrogel found by del-Mazo-Barbara and Ginebra (2021). Again, a transition to a plateaued curve is apparent at high volume fractions.

The results for both the chitosan and platelet content variations are problematic: combinations satisfying the rheological requirements involve either τ_y or $\bar{G}'$ vastly overshooting. This overshoot is undesired because it results in high printing pressures required for flow, which can explain the underextrusion observed for a number of the compositions and at high print speeds. Even inks that show yield stress and stiffness close to the requirements fail to demonstrate satisfactory printability in practice.

To summarise, despite obtaining inks that (partially) conform to the printability requirements on yield stress, stiffness, and shear-thinning, all Al_2O_3/HMWC inks displayed poor shape fidelity in practice. As such, varying alumina or HMWC is insufficient for achieving printability in these hydrogels for the ranges tested. A different approach is necessary.

3.2.5. Isolating the effect of the platelets

To better understand the ink rheology and the effect of the platelets on the ink's behaviour and recognise the required polymer behaviour, suspensions containing only increasing amounts of alumina platelets dispersed in water were printed at varying print speeds. Since water has no shear-dependent behaviour, we can isolate microstructural changes dependent only on platelet behaviour and assess how they influence printability. The corresponding raster fidelity results are shown in fig. 3.17.

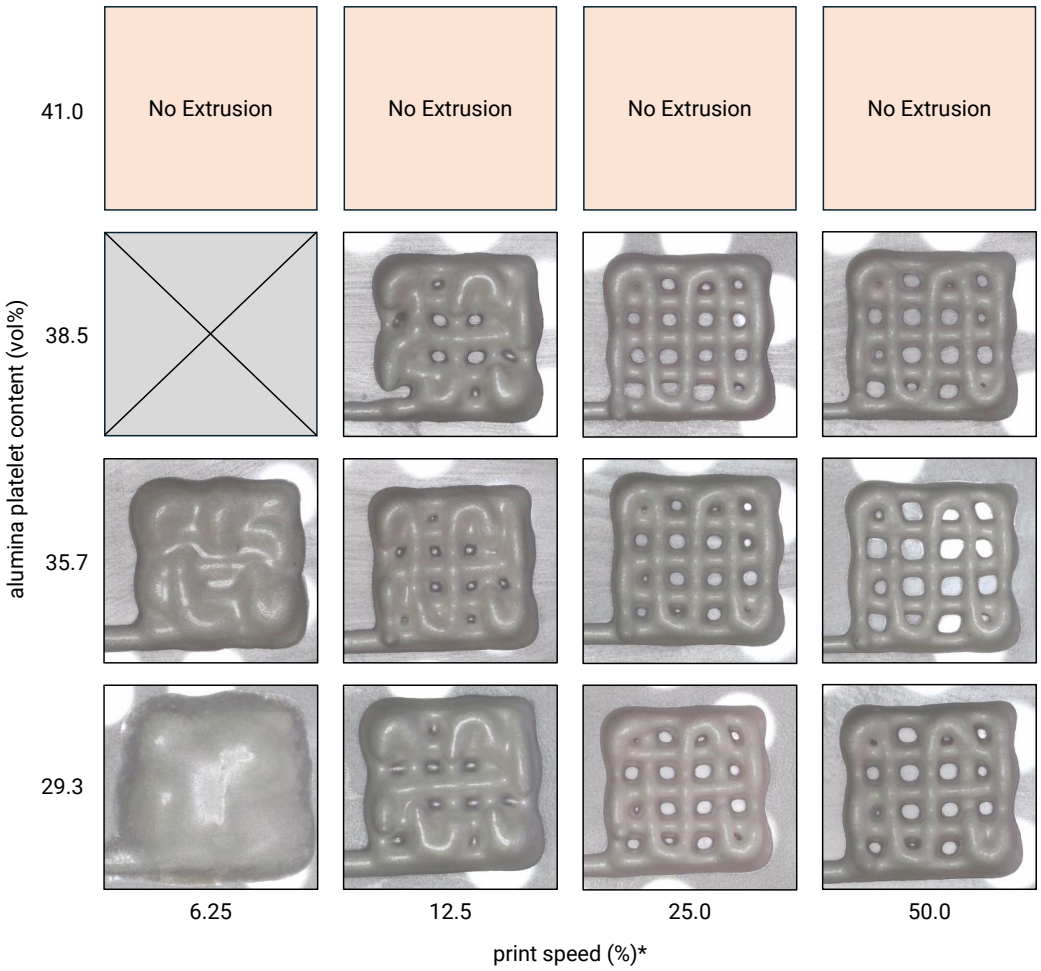

Figure 3.17: Raster print fidelity for aqueous colloidal suspensions with varying alumina platelet content and print speeds showing a clear increase in quality for higher print speed, suggesting significant alignment-related changes in rheology. Crossed-out grey squares denote lost/corrupt data. *100% print speed equates to 1000 mm/min.

Three observations can be drawn from these short experiments. First, platelet content does not affect printability except at the lowest print speed. Second, print speed significantly influences filament retention and, therefore, points to strong changes in colloidal interactions, possibly due to shear-induced alignment. Third, in agreement with other experiments on DIW of alumina-water colloids (del-Mazo-Barbara and Ginebra, 2021), a maximum printable volume fraction of 38.5–41.0 vol% is demarcated at which the printer stalls, which is commonly associated with a transition point from shear-thinning to shear thickening behaviour (no data collected). Last, the general printability remains low. Crucially, the shape fidelity remains similar to the polymer-loaded ink. Hence, the polymer does not have the desired effect. In this case, the observed corner rounding and underextrusion suggest insufficient shear thinning. A rheological modifier or base polymer with a more substantial shear-thinning effect is believed to be beneficial.

3.2.6. Troubleshooting by using fumed silica as a rheological modifier

The addition of a few wt% fumed silica has been successful in the past for solving printability issues for colloidal suspensions (Krüger, 2022) by promoting a highly shear-thinning behaviour. Subsequently, small weight fraction additions of fumed silica were assessed by printing rasters for compositions containing 0.4–1.2 vol% fumed silica for 0.65 vol% and 1.93 vol% chitosan in Al_2O_3/HMWC mixtures. The results are shown in fig. 3.18.

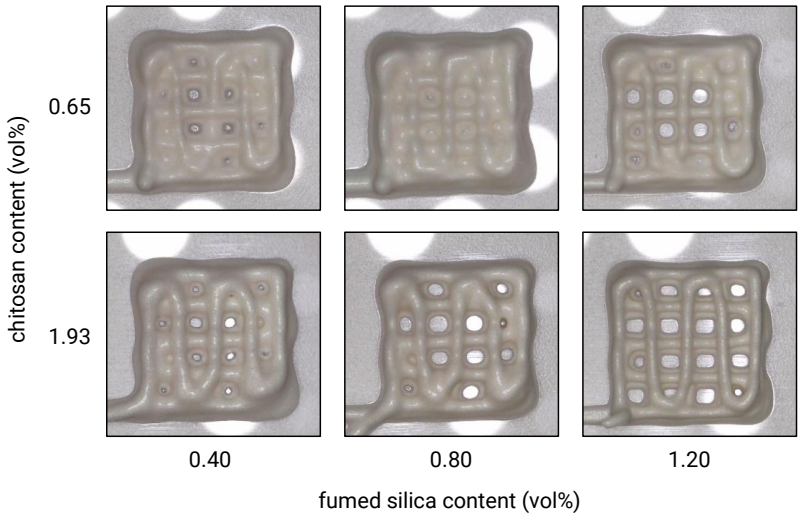

Figure 3.18: Raster print fidelity for varying fumed silica content showing a barely noticeable effect at low chitosan content and an improvement at higher content.

A somewhat noticeable improvement can be observed for increasing fumed silica content. However, the ink's homogeneity deteriorated, with the extrudate's consistency varying from solid to highly fluid during extrusion. The issue could not be resolved despite speed mixing for more extended periods to ensure homogeneity. As a result, this avenue was abandoned. Better results may be attainable using a hydrophilic variant since this may give more favourable colloidal interactions.

3.3. Nacre-inspired: alumina and cellulose nanofibres

Given the unsatisfactory printability of Al_2O_3/HMWC inks despite extensive troubleshooting, a different approach is investigated in this section. In particular, it was believed that stronger shear-thinning may improve results. A common choice of highly shear-thinning additive is cellulose nanofibres (CNFs) (del-Mazo-Barbara and Ginebra, 2021), which have yielded promising results in ceramic suspensions of spherical colloids (Smay et al., 2002). As such, an ink was prepared based on Al_2O_3/CNF.

3.3.1. Methods

Given the insights obtained in fig. 3.17, the CNFs were mixed into an as high as possible volume fraction of ceramic platelets in a volume ratio of 7:93 respectively and prepared similarly to previous mixtures. This composition could not be extruded; hence, the volume-wise solid fraction of the ink was reduced until a printable composition was found. The addition of nutrients was again omitted to reduce complexity and increase efficiency.

3.3.2. Printability

The compositions with varying solid fractions were evaluated as before. The results are shown in fig. 3.19.

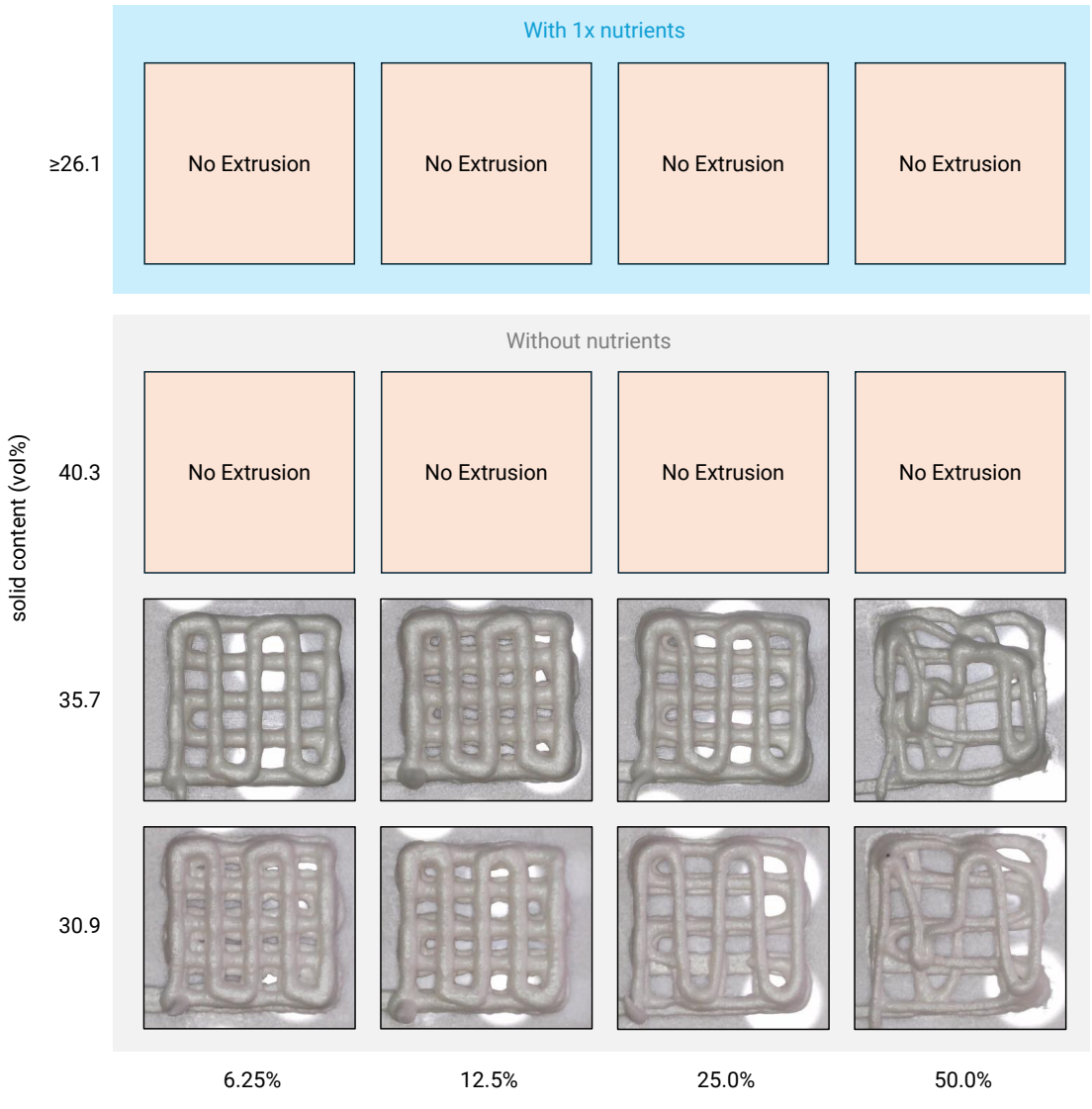

Figure 3.19: Raster print fidelity for varying solid content and with the addition of biomineralisation nutrient solution (N.S.) at optimal (1x) concentration. Satisfactory results are obtained below 25 % print speed and 40.3 vol% solid content without nutrients. The inclusion of nutrients at optimal concentrations disrupts printing altogether, suggesting a significant increase in viscosity. *100 % print speed equated to 1000 mm min^{-1}.

Although fidelity remains low in absolute terms, with filaments now demonstrating noticeable roughness, overhang sagging, and slight corner rounding, the improvement is considerable over previous compositions and deemed sufficient for preparing mechanical coupons. Notably, a reduction in fidelity is observed again for 50 % print speed, with onset more apparent at 25 %. Therefore the recommended print speed setting for maximum shape fidelity with this composition is set at 12.5 %.

Given the satisfactory results, the nutrient solution was re-introduced at its optimal concentrations. Most unexpectedly, the composition could not be extruded at any print speeds despite having a lower solid fraction to accommodate the dissolved nutrients (fig. 3.19, bottom row), suggesting that the nutrients significantly distort the ink rheology. Possible mechanisms for this peculiar effect are raised in chapter 5.

Rather than dwelling on the problem, the effect was circumvented by diluting the nutrient solution until a reasonably printable ink was achieved, roughly at 0.5× concentration. Printing fidelity notably increased with nutrient solution concentration (data not captured). Although not ideal, lower concentrations have yielded measurable precipitation in other studies (Stocks-Fischer et al., 1999). Hence, it is likely that biomineralisation will still occur at perceivable rates at these concentrations.

3.3.3. Rheology

For completeness and to compare to the previous rheological results, amplitude sweep and flow sweep measurements were conducted as previously and are included in fig. 3.20. Notice the similarities to the successfully printing PS/PC ink.

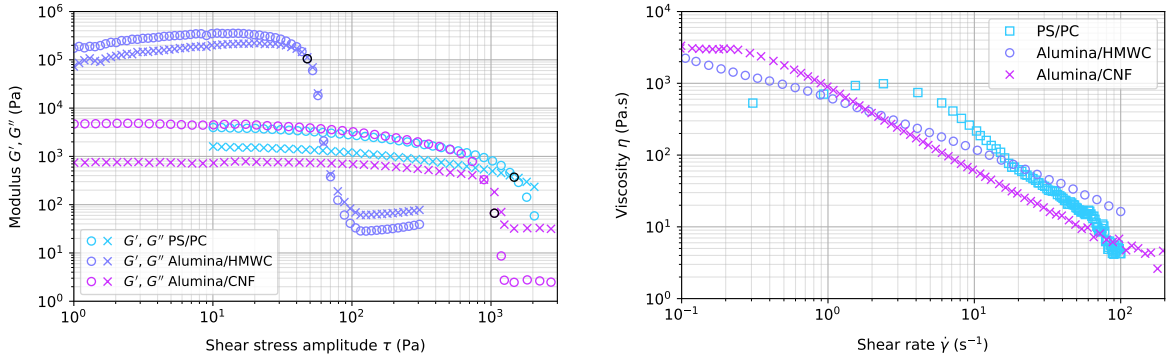

(a) Amplitude sweep curves for PS/PC, Al_2O_3/HMWC, and Al_2O_3/CNF inks. Note the similarity between PS/PC and Al_2O_3/CNF inks, demonstrating satisfactory printability.

(b) Flow sweep curves for PS/PC, Al_2O_3/HMWC, and Al_2O_3/CNF inks.

Figure 3.20: Amplitude and flow sweep curves comparing PS/PC, Al_2O_3/HMWC, and Al_2O_3/CNF rheology. The Al_2O_3/HMWC ink contains 25.7 vol% alumina and 1.93 vol% HMWC, whereas the Al_2O_3/CNF ink contains 23.2 vol% alumina and 1.72 vol% CNF.

3.4. Chapter summary

This chapter detailed the development of an ink formulation for direct ink writing of nacre-mimetic materials. Initial experiments with a phyllosilicate (PS) and powdered chitosan (PC) ink showed good printability and surface biomineralisation, though internal precipitation was absent. A subsequent formulation using alumina (Al_2O_3) platelets and high molecular weight chitosan (HMWC) better represented nacre but exhibited poor printability, prompting a parametric study on rheology that yielded no satisfactory results. Attempts to modify rheology with fumed silica also proved ineffective.

Switching to cellulose nanofibres (CNF) instead of chitosan improved printability with alumina, though only at reduced nutrient concentrations. This final Al_2O_3/CNF ink will undergo further physicochemical characterisation and mechanical testing in the next chapter.

This page has been intentionally left blank.

4

Material characterization

With an ink formulation suitable for direct ink writing obtained, the next step is to assess the properties of printed material. The methodology describing this is given in section 4.1, followed by results and discussion in section 4.2.

4.1. Methods

Material properties were evaluated using beam-shaped coupons with varying bacterial content. Microstructures of filaments printed at different speeds and nozzle lengths were analysed. Coupon geometry was assessed via 3D optical profiling, followed by density and void content measurements. Mechanical performance was tested using 4-point flexural testing, with fractured cross-sections examined under SEM. Calcium carbonate content was quantified via thermogravimetric analysis and SEM, while filament alignment was assessed through SEM cross-sections. An overview is shown in fig. 4.1.

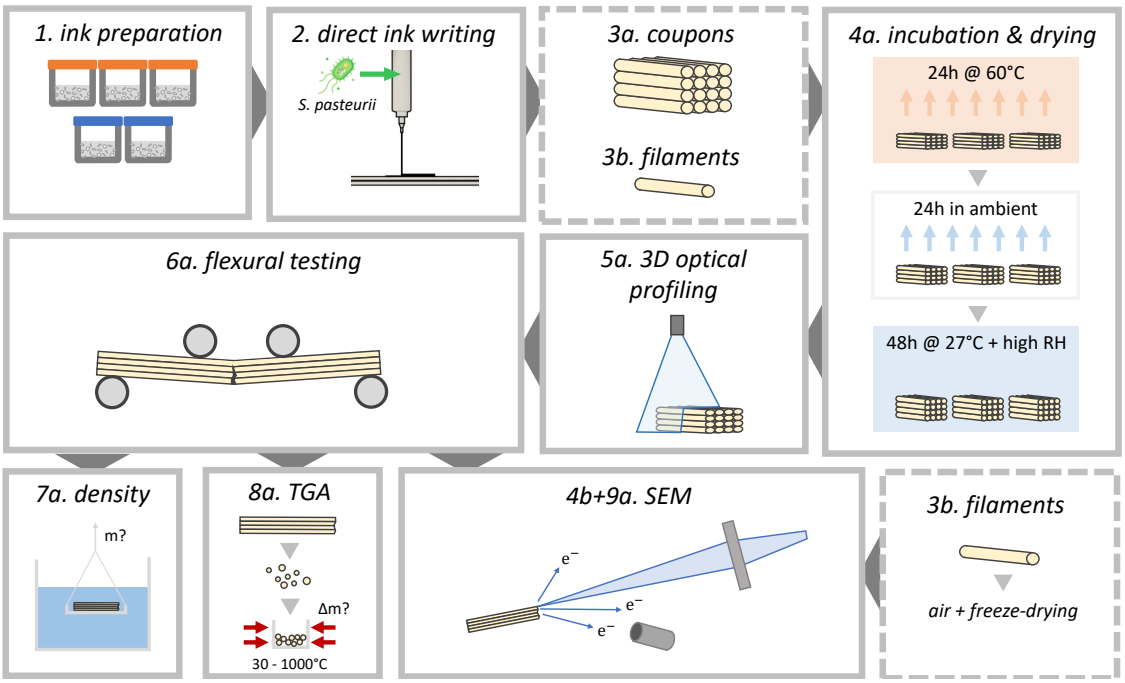

Figure 4.1: Illustrated overview of characterisation process showing workflow. Five compositions consisting of three inks with varying bacteria content and two controls are prepared (1), followed by direct ink writing (2), yielding coupons (3a), and filaments (3b). Coupons are incubated and dried (4a), followed by optical profiling (5a) and flexural testing (6a). The broken coupons are used for density measurements (7a) and thermogravimetric analysis (TGA) (8a). Both the coupons and filaments are finally observed under scanning electron microscopy (SEM) (4b+9a).

4.1.1. Coupon and single filament fabrication

Coupons in the shapes of rectangular beams and individual filaments were printed from 5 different Al_2O_3/CNF ink compositions allowing comparison between them. The compositions are summarised in table 4.1, and follow the same preparation process.

First, dry powders were sterilised by autoclaving in a bottle with a cotton stopper, followed by drying in a convection oven at 120 °C and replacing the cotton stopper with the sterile cap for storage. Powders were weighed and combined into a sterilised mixing beaker inside a biosafety cabinet, which was closed and roll-mixed for 15 minutes at 80 RPM. Nutrient solutions were prepared by weighing the relevant amounts into a beaker, adding distilled water, transferring to a 50 ml syringe and sterilising via 0.22 µm filtration. The powders and solution were then mixed in a sterile environment and speed mixed in 5 rounds, each round consisting of about 2 minutes at 3500 RPM followed by about 2 minutes at 1000 RPM. The latter aids in degassing and pushing the ink that creeps up the sides back down, ensuring as high as possible homogeneity.

Following speed mixing, equal volumes of inoculum or, in the case of the control batches, distilled water was added to the inks, followed by another 2 min round of speed mixing at 600 RPM. Inks were then transferred to 10 ml syringes, followed by degassing under vacuum using a custom adapter and tapping the syringe on a hard surface, thereby forcing air bubbles out. This step was observed to reduce the number of under-extrusions during printing and functioned better than centrifuging, as the latter tended to separate out the liquid phase even at mild rates.

Table 4.1: Overview of Al_2O_3/CNF compositions prepared for material characterization

Composition	Description
TC15	Control
TC16_1	Control + 0.1x nutrient concentrations
TC16_2	0.1x nutrient concentrations + 1x *S. pasteurii* inoculum
TC16_3	0.1x nutrient concentrations + 2x *S. pasteurii* inoculum
TC17	0.5x nutrient concentrations + 2x *S. pasteurii* inoculum

Before printing, the Ender-3 V2 printer was prepared by transferring to the biosafety cabinet (fig. 4.2) prior to printing and thoroughly sterilising using 70 % ethanol and the cabinet's UV function. Printing was controlled from outside through a laptop running Repetier-Host software connected to the printer via a USB cable. The as-bought print bed was flipped to the smoother side and covered with a sheet of PTFE to facilitate coupon removal after drying. The print bed was levelled using an empty syringe and a small piece of aluminium foil, making sure to tighten each bed levelling knob until the nozzle lightly scrapes the aluminium foil at all x- and y- locations without changing z.

Each ink then underwent the same steps for printing: after loading the syringe containing the ink into the extrusion module, the luer cap was replaced by a 0.51 mm diameter steel-tip nozzle as used previously. 15 coupons were printed consecutively with filaments oriented in length-wise direction with length 30 mm, width of 4 nozzle diameters (2.04 mm), and height of 4 layers totalling 1.89 mm. The layer height was set to 70% of the nozzle diameter to improve layer adhesion. Immediately after printing, the coupons were covered by a sterile plastic box containing damp towels (fig. 4.3a). These towels were wetted with sterile deionised water after soaking in ethanol and left to dry inside the cabinet, ensuring sterility of the covered environment. To stimulate biomineralisation the covered coupons were transferred to an incubator set at 27 °C and incubated for 48 h. After removal, the samples were left to dry in ambient air for 24 h (fig. 4.3b) followed by deactivation and full drying in a convection oven at 60 °C for an additional 24 h. Upon removal, the as-printed parts were stored in an air-conditioned room at ~20 °C and ~55 %rH until further use.

As for the individual filaments, batch TC15 was used to print ~10 mm long lines onto a PTFE-lined glass slide. Here, the z-height was set to increase to 1.1 times the nozzle height after printing the primer, so that the filament is gently laid down onto the print bed, ensuring minimal deformation. Printing was followed by air- and oven-drying as done previously followed by storage until further use.

4.1.2. Coupon profilometry

To quantify the dimensional changes during drying and capture precise cross-sections of each coupon for calculation of flexural strength, 3D scans of the coupons were made using a 3D optical profilometer (appendix C.4). Length-wise profiles were obtained for each coupon by averaging 4 line scans spaced 0.1 mm apart and centred width-wise. Width-wise profiles were obtained by averaging 30 line scans with the same

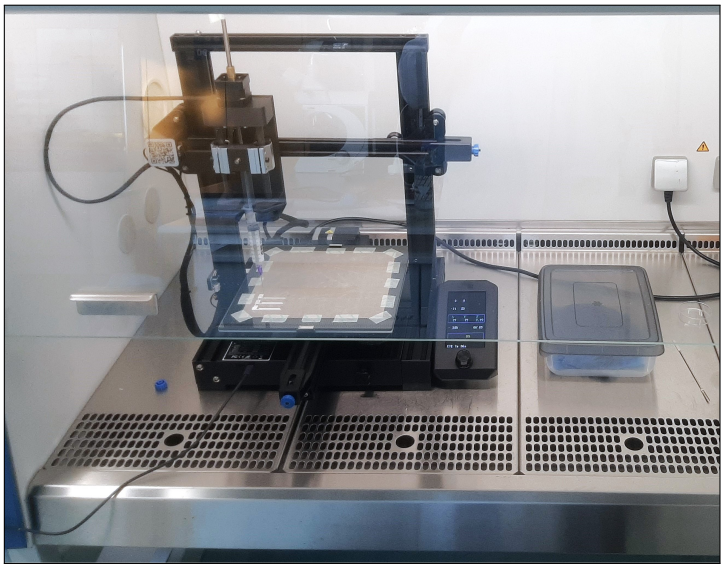

(a) View of the printer inside biosafety cabinet during coupon fabrication. Sterile humidified enclosure (plastic box) is placed to the right of it.

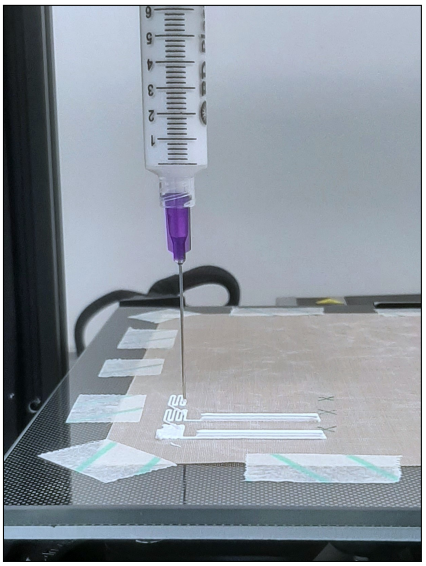

(b) Close-up of coupons being printed inside the biosafety cabinet.

Figure 4.2: Views of sterile printing process inside a biosafety cabinet.

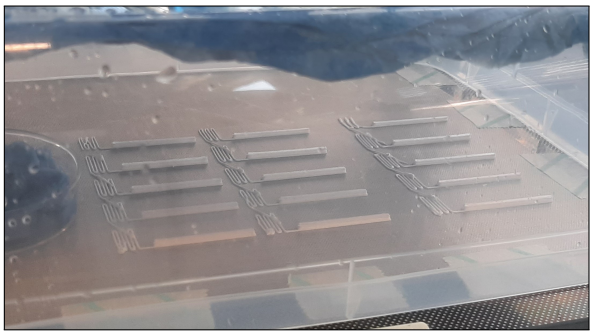

(a) Photo of coupons inside humidified enclosure showing geometry immediately after printing.

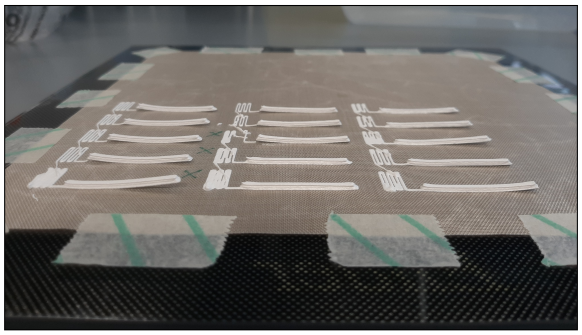

(b) Photo of same coupons after removing enclosure and drying in air, showing partial detachment and warping.

Figure 4.3: Photos of coupon geometries directly after printing and after drying in air.

spacing, centred length-wise. Average profiles were calculated by the proprietary microscopy software and exported as a single .csv file for each coupon.

From these profiles, the cross-sectional area can be computed by numerically integrating, i.e.

$$A = \sum_{i=0}^{n-1} \Delta y_i \, \bar{h}_i \tag{4.1}$$

where $\Delta y_i = y_{i+1} - y_i$ is the width-wise step size and $\bar{h}_i = \frac{1}{2}(h_i + h_{i+1})$ the average height of the step, consistent with the coordinate system in fig. 4.5. Using this area the shrinkage ratio h_{dry}/h_{wet} can be computed for each coupon.

4.1.3. Void content estimation

The density of a solid is frequently determined using Archimedes' principle, which in combination with theoretical density estimations can be used to estimate the porosity or void content of a material. Archimedes' principle states that a body immersed in a fluid experiences a buoyancy force equal to the weight of the fluid displaced by the body. Comparing a solid sample's apparent weight in air to its apparent weight in an auxiliary liquid, the density can then be determined via

$$\rho = \frac{A}{A - B}(\rho_0 - \rho_L) + \rho_L \tag{4.2}$$

where A is the measured weight of the sample in air, B the measured weight in the auxiliary liquid, ρ_0 the density of the auxiliary liquid and ρ_L the air density.

Typically, an oil, water, or ethanol is used as auxiliary liquid. Oils such as silicone oil would be most suitable in this case since the sample is hydrophilic (causing swelling of the cellulose if immersed in water) and because some of the compounds present in the nutrient mix are highly soluble in water and partially soluble in ethanol. However, the quantities of well-characterised oils available in the lab were insufficient, and given the relatively low concentrations and solubilities of the ethanol-soluble compounds, ethanol was selected instead.

Compositions TC15, TC16_1, TC16_2, TC16_3, and TC17 were measured by taking 4-5 random halves of coupons, totalling approximately 250mg in weight. These coupons were weighed collectively to obtain A and B. The immersed weight B was recorded at two moments, once immediately after immersion (B_i) and once at equilibrium (B_{eq}) approximately one hour after immersion. Upon immersion, the samples were observed to fizz at a rapidly decaying rate, at the same time the observed weight was seen to decrease. In approximately 10-minute intervals the sample holder was shaken using tweezers, dislodging built-up bubbles with an associated weight increase.

4.1.4. Mechanical testing

Mechanical performance was assessed via destructive four-point flexural tests as depicted in fig. 4.4. ASTM designation C1161-13 was taken as a guideline standard albeit with significant deviations. The coupons prepared in section 4.1.1 were used as-printed. Coupons were manually placed topside-down on the bottom supports. This orientation was chosen because preliminary tests showed that failure occurred in tension (i.e. the supported side), therefore meaning that the material's strength is better reflected through failure in the top print layer than by the distorted bottom layer. Due to the lack of proper bearing supports, articulating fixtures, and alignment tools as recommended in ASTM C1161-13, placement of each beam coupon in the fixture involved some heuristics and manual fine-tuning in order to properly level them for simultaneous contact with the top loading supports. In particular, because the coupon surfaces are not parallel (fig. 4.6) and because all supports had some observable misalignment, each coupon's position had to be finely adjusted so that the top loading fixtures would touch the coupon at the same time.

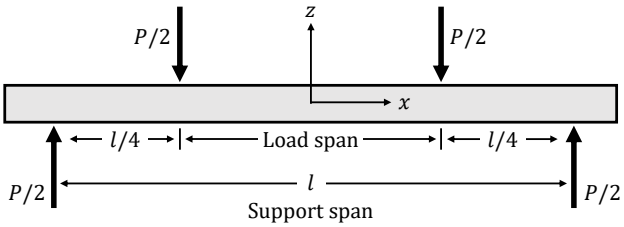

Figure 4.4: Loading diagram of a four-point flexural test.

Following placement, each coupon was loaded until complete failure (<90% peak load) at a displacement speed of 0.1 mm/ min. A USB microscope recorded the full test for observation of failure type, crack location and growth. These videos can be found via appendix A.4.

Adjusted force-displacement data appendix E.1 was processed into stress-strain curves by calculating the second moment of area and neutral axis for each coupon cross section obtained from profilometry (section 4.1.2) and inserting into the symmetric bending equation:

$$\sigma = \frac{Mc}{I} \tag{4.3}$$

Where σ is the stress experienced at a distance c from the neutral axis for a cross-section with a second moment of area I under a bending moment M. The second moment of area in this case is obtained by first computing the centroid (neutral axis) location and performing numerical integration by approximating the cross-section as a sum of rectangular strips, i.e.

$$I_{yy} = \sum_{i=0}^{n-1} \frac{\Delta y_i \, \bar{h}_i^3}{12} + \Delta y_i \, \bar{h}_i \left(\frac{1}{2} \bar{h}_i - h_c \right)^2 \tag{4.4}$$

where I_{yy} is the second moment of area, $\Delta y_i = y_{i+1} - y_i$ the step size, $\bar{h}_i = h_{i+1} - h_i$ the average height of the segment, and h_c the neutral axis location on the y-axis. Similarly, the neutral axis location is obtained by numerically integrating the first moment of area and dividing by the total area obtained through eq. (4.1):

$$Q_y = \sum_{i=0}^{n-1} \frac{1}{2} \Delta y \, \bar{h}_i^2 \tag{4.5}$$

$$h_c = \frac{Q_y}{A} \tag{4.6}$$

The maximum bending moment is then obtained simply from Euler-Bernoulli beam theory assuming a symmetric, balanced load at quarter span; it is constant along the load span and equates to

$$M = \frac{P}{2} \frac{l}{4} \tag{4.7}$$

where P is the load measured by the load cell and l the support span as depicted in fig. 4.4. For the stress location c in eq. (4.3) the maximum height of the profile is used since this, assuming no stress concentrations, is the location of highest tensile stress. The strain, on the other hand, is calculated via

$$\varepsilon = \frac{12 c \delta_m}{l^2} \tag{4.8}$$

where δ_m is the measured crosshead displacement. This data analysis algorithm was implemented in Python and the area and second moment of area calculation were verified by approximating the cross-section as a trapezoidal shape, yielding values within a few per cent of the batch averages. The code is available via appendix A.4.

4.1.5. Scanning electron microscopy

Following full drying and, in the case of the beam-shaped coupons, mechanical testing, both the coupons and filaments were freeze-dried by immersing in liquid nitrogen until boiling seizes and placing under 0.1 mbar vacuum overnight. After removal from the vacuum, the samples were gently placed onto a sample holder lined with carbon tape with the cross-section facing upwards. To prevent charging, samples were sputter coated with 15–20 nm gold. Observation was performed at 5 kV acceleration voltage, 8 µA probe current, and using a low magnification (LM) mode with the lower secondary electron detector (LEI).

4.1.6. Thermogravimetric analysis

Whereas calcium chloride fully dehydrates below 250 °C and does not decompose up to its melting point at 1935 °C, calcium carbonate decomposes rapidly into calcium oxide and carbon dioxide above 600 °C. This difference can be used to distinguish between the two calcium species and quantify their presence within biomineralised samples.

Thermogravimetric analysis (TGA) allows the measurement of a sample's decomposition behaviour by measuring its weight change when subject to heating in a controlled atmosphere. Since the printed material contains a variety of compounds with weight fractions possibly in the range of that of calcium carbonate, the decomposition behaviour of each must be verified. In order of volume fraction, pure alumina should show little to no change across the entire spectrum, although hydrated forms such as surface hydroxyl groups can cause mass losses up to 550 °C (Yang et al., 2007). Cellulose, including CNF, degrades by about 70 wt% in a single step below 400 °C in a nitrogen atmosphere, followed by a shallow decline above this. In air, full degradation (>99 wt%) occurs below 500 °C (Mautner et al., 2017). Similarly, urea degrades fully (>90 wt%) below 400 °C (Rahmanian et al., 2015). No TGA data could be found on peptones and yeast extract. However, given that both comprise mostly organic material, mainly proteins and amino acids, followed by smaller quantities of carbohydrates, minerals, and vitamins, it is likely that most of the degradation occurs below 600 °C, followed by oxidation of organic residues at higher temperature (Tao et al., 2023). This latter aspect favours TGA in nitrogen atmosphere over air. Lastly, ammonium chloride decomposes fully (>99 %) below 400 °C in argon atmosphere (Zelenková and Slovák, 2022). A similar result can be expected in nitrogen atmosphere.

Fortunately, no clear overlaps exist with the decomposition of calcium carbonate besides possibly a shallow decline caused by CNF. The calcium carbonate content can thus be quantified via the change in mass between 600 °C and 900 °C via

$$\mathrm{wt\%}_{\mathrm{CaCO_3}} = \frac{\Delta \mathrm{wt\%}}{m_{w,\mathrm{CO_2}}} m_{w,\mathrm{CaCO_3}} \tag{4.9}$$

where Δwt% is the weight percentage loss, m_{w,CO_2} the molecular weight of CO_2, and $m_{w,CaCO_3}$ the molecular weight of calcium carbonate.

As a result, following flexural testing, one coupon from each batch was ground and placed into alumina crucibles suitable for TGA. Each crucible was weighed empty before each measurement and filled with at least 10 mg. Each sample was then subjected to a temperature ramp from 30 °C to 1000 °C at 10 °C/ min under constant flow of nitrogen at 19.8 ml/ min while continuously monitoring weight. A blank control was obtained by running the same program with an empty crucible, and the resulting weight-temperature curve was fitted using a second-degree polynomial to remove noise and subtracted from the sample curves before converting to weight %.

4.2. Results and discussion

In this section, all material characterisation results are presented and briefly discussed. In particular, optical profilometry yielded coupon surface maps and estimations of shrinkage and void content, demonstrating the drying behaviour of the ink, shown in section 4.2.1. This is coupled with measurements of density via Archimedes' method in section 4.2.2. The resulting void contents are compared. Four-point bending tests are summarized in section 4.2.3, followed by an assessment of the material microstructures observed via SEM in section 4.2.4. Finally, although yielding poorly interpretable results, thermal curves from TGA are briefly discussed in section 4.2.5.

4.2.1. Coupon profilometry

After extrusion, the deposited material begins to dry immediately, expelling moisture and causing shrinkage. This shrinkage significantly impacts part fidelity, making it essential to quantify. At the same time, controlled shrinkage is desirable, as it helps prevent void formation within the material. Hence, it is essential to quantify coupon shrinkage. Figure 4.5 shows the width-wise profiles at a length-wise central section of each beam for each ink composition obtained after complete drying. Generally, there appears to be a relatively large shrinkage in the height-wise direction, about 25 % across all coupons and ink compositions. This height decrease is most pronounced for compositions TC16_2 and TC16_3.

Similarly, significant bottom-layer sag can be observed for the TC16 compositions. This implies higher filament retention for compositions TC15 and TC17, which is peculiar considering that the worst retention was expected for TC17 as suggested by the printability experiments in section 3.3.2. Possibly, the addition of nutrients initially causes a decrease in viscosity due to increased lubrication but serves to thicken at higher concentrations.

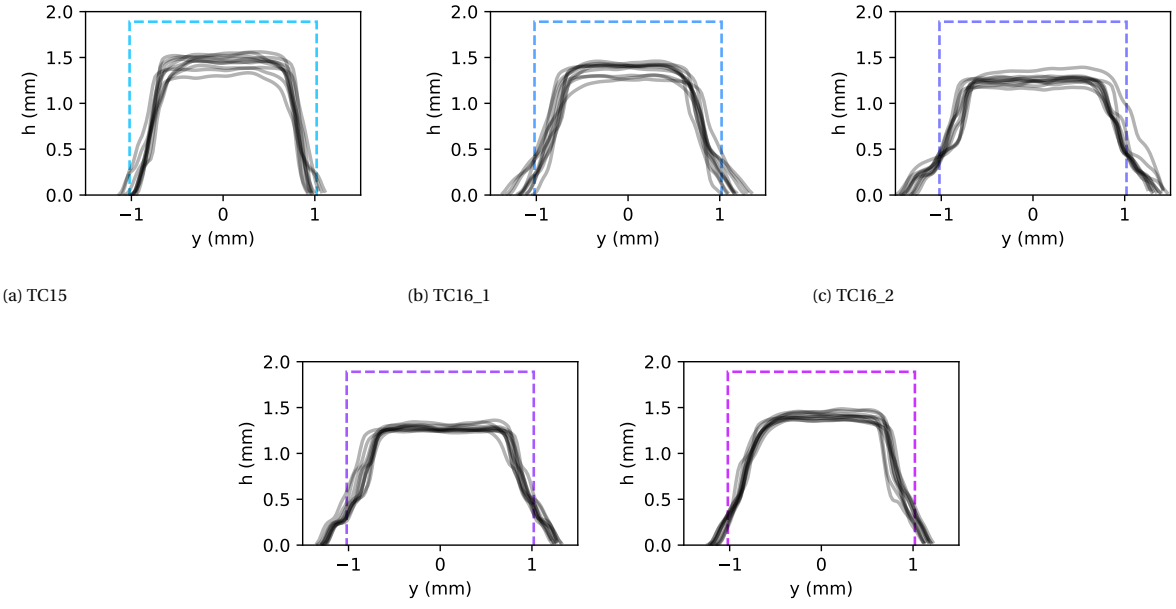

(a) TC15 (b) TC16_1 (c) TC16_2

(d) TC16_3 (e) TC17

Figure 4.5: Coupon height profiles in width-wise direction. Dashed lines represent the ideal dimensions instructed by the `.gcode` files.

Similarly, length-wise profiles were obtained for the width-wise middle of the coupon. These are shown in fig. 4.6. For most coupons, sag seems to be worst in the middle, whereas the edges appear to retain their shape better. Since these edges are essentially subject to a larger surface area exposed to air, the difference may be a result of faster drying and/or reduced mobility. Additionally, since the edges are the points where the print lines turn in direction, locally the microstructure may be different in a way that impedes shrinkage. This aspect will not be investigated further. More importantly, some coupons appear to *increase* in height at the edges. This is an artefact resulting from the upwards warping of the beams upon drying, which is not apparent from the profilometry but seen clearly in fig. 4.3b.

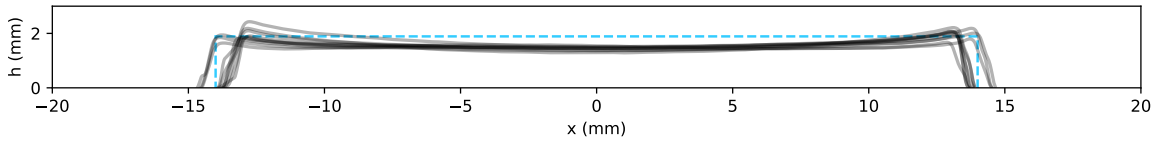

(a) TC15

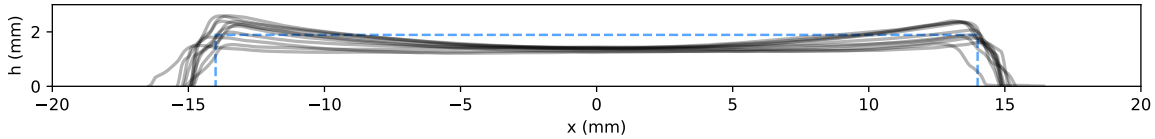

(b) TC16_1

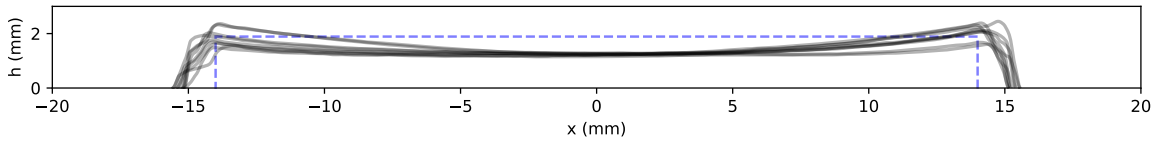

(c) TC16_2

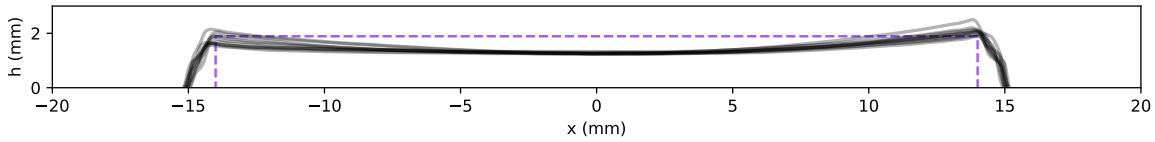

(d) TC16_3

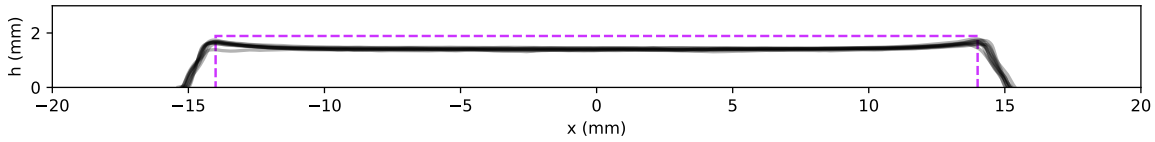

(e) TC17

Figure 4.6: Coupon height profiles in length-wise direction. Note that the curvature of the bottom side is not immediately apparent but will significantly affect the perceived cross-section at distances far from the middle. Dashed lines represent the ideal dimensions instructed by the `.gcode` files.

From these height profiles, we can also compute shrinkage statistics by comparing the dry cross-sectional area to the ideal, square cross-section. Since the coupon warping causes an apparent increase in cross-sectional area at the edges, only the width-wise profiles are used for this. The results are given in table 4.2. Compared to full compaction, that is, the expected volume reduction should all water be expelled and no voids remaining (~74.5 %), these shrinkage numbers are significantly lower. In fact, an estimation of the void content can be computed by calculating the expected shrinkage for full compaction for each ink composition and subtracting the true shrinkage. These values have also been included in table 4.2, and confirm a high void content in the order of 35 %. This is beneficial for printing fidelity since the shape of the filament shape is retained. However, it is likely severely detrimental to mechanical performance, which is apparent in section 4.2.3.

Table 4.2: Shrinkage statistics obtained for each coupon batch. The standard deviation is given in brackets.

Batch	Mean shrinkage (%)	Mean void content (%)
TC15	39.7 (1.3)	35.2 (1.3)
TC16_1	39.2 (1.0)	35.3 (1.0)
TC16_2	36.3 (1.9)	38.2 (1.9)
TC16_3	38.1 (0.7)	36.4 (0.7)
TC17	37.4 (0.5)	35.5 (0.5)

4.2.2. Void content estimation

The high void content estimated using shrinkage statistics can be corroborated by performing density measurements of the coupons. Values of dry weight A, wet weight immediately after submersion B_i and at equilibrium B_{eq}, and corresponding densities ρ_i and ρ_{eq} are presented in tables 4.3 and 4.4.

Table 4.3: Coupon densities measured via Archimedes' method immediately after immersion.

Batch	A (mg)	B_i (mg)	T (°C)	ρ_0 (g cm^{-3})	ρ_i (g cm^{-3})
TC15	235.5 ± 0.1	158 ± 20	20.0 ± 0.1	0.78934	2.40 ± 0.83
TC16_1	226.1 ± 0.1	143 ± 20	20.4 ± 0.1	0.78900	2.14 ± 0.68
TC16_2	223.9 ± 0.1	136 ± 20	20.4 ± 0.1	0.78900	2.01 ± 0.59
TC16_3	248.1 ± 0.1	148 ± 20	20.8 ± 0.1	0.78866	1.95 ± 0.49
TC17	230.1 ± 0.1	148 ± 20	20.8 ± 0.1	0.78866	2.21 ± 0.71

Table 4.4: Coupon densities measured via Archimedes' method after reaching equilibrium.

Batch	A (mg)	B_{eq} (mg)	T (°C)	ρ_0 (g cm^{-3})	ρ_{eq} (g cm^{-3})
TC15	235.5 ± 0.1	182.8 ± 0.1	20.4 ± 0.1	0.78900	3.834 ± 0.023
TC16_1	226.1 ± 0.1	174.0 ± 0.1	20.4 ± 0.1	0.78900	3.420 ± 0.021
TC16_2	223.9 ± 0.1	174.0 ± 0.1	20.7 ± 0.1	0.78874	3.535 ± 0.022
TC16_3	248.1 ± 0.1	194.2 ± 0.1	20.8 ± 0.1	0.78866	3.626 ± 0.021
TC17	230.1 ± 0.1	179.6 ± 0.1	20.8 ± 0.1	0.78866	3.589 ± 0.022

Note immediately the large differences between ρ_i and ρ_{eq}. Three reasons are possible for this large difference: (i) dissolution of ethanol-soluble compounds, (ii) an inertia/stabilisation-related peak in weight immediately after dropping into the sample holder, (iii) ingression of auxiliary liquid into voids. To quantify the dissolution of compounds the submerged samples were left to dry for 24 h in ambient air and re-weighed. The maximum weight loss measured was 0.28 %. This is much smaller than the observed differences. Note that dissolution is only relevant for the samples weighed at equilibrium and is likely negligible for the weights measured immediately after immersion. Regarding the second point, re-immersion of wet samples showed that the balance weight stabilizes to the second significant digit within 1 reading, implying that this is negligible. This leaves only the third point, which is corroborated by observations of samples fizzing and building up gas on the surface over time accompanied by a gradual increase in mass over time.

The weights at equilibrium can be compared to theoretical calculations of density to validate the measurements. Additionally, they provide a clue about the 'interconnectivity' of the voids, i.e. whether the liquid ingresses to fill voids fully or if some voids are inaccessible. This theoretical density ρ_{th} can be obtained by summing up the products of each component's density and volume fraction, i.e.:

$$\rho_{th} = \sum_i v_{f,i} \cdot \rho_i \tag{4.10}$$

where $v_{f,i}$ is the volume fraction of component i with corresponding density ρ_i. Calculating for compositions TC15 through TC17_1 gives the results shown in table 4.5. Here we see that the theoretical densities agree reasonably well with the measured densities at equilibrium, with a maximum difference of 9.2 % for TC16_1. This suggests that the voids are connected which is often only the case for large void contents.

The sample void volume fraction $v_{v,f}$ can then be determined simply via

$$v_{v,f} = \frac{\rho_{th} - \rho}{\rho_{th}} \tag{4.11}$$

with results shown in table 4.5.

Table 4.5: Computed theoretical densities and estimated void content using Archimedes' method (AM) on mechanically tested coupons and via coupon geometry (CG). Propagated uncertainty is included next to the value.

Batch	ρ_{th} (g cm^{-3})	Void content via AM (%)	Void content via CG (%)
TC15	3.828	37.3 ± 21.7	35.2
TC16_1	3.767	43.2 ± 18.3	35.3
TC16_2	3.767	46.6 ± 15.7	38.2
TC16_3	3.767	48.2 ± 13.0	36.4
TC17	3.548	37.7 ± 20.0	35.5

Despite the large errors, the void content estimations obtained via Archimedes' method agree well with those estimated from the coupon geometry. It is relevant to mention here that due to the nature of the measurement (observing the first value shown on the scale after immersion), the estimations are likely conservative and that the error should tend towards lower values of void content. Nevertheless, the void content remains excessively high. This is likely to be reflected in the mechanical performance obtained.

4.2.3. Mechanical behaviour

Results of four-point flexural tests for coupons from the five available bioink compositions (table 4.1) provide a general indication of the mechanical strength of the printed Al_2O_3/CNF material and can reveal the effects of embedding bacteria and nutrients. To clearly view these differences, maximum flexural stress and flexural work of fracture values were extracted from the raw force-displacement data (appendix E.1) and compiled into statistical plots, shown in figs. 4.7 and 4.8. Here, moving from left to right starting at TC16_1 essentially represents an increasing stimulus for bacterial activity.

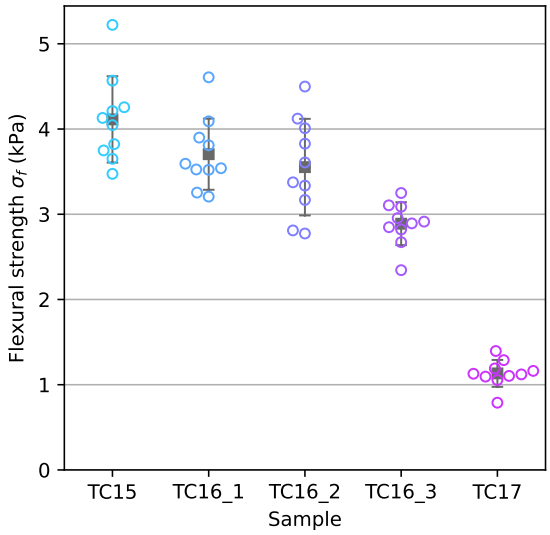

Figure 4.7: Flexural strength statistics evaluated for each coupon batch.

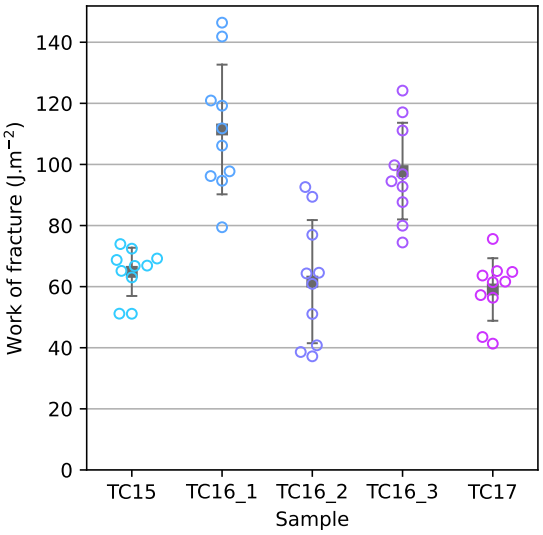

Figure 4.8: Flexural work of fracture statistics evaluated for each coupon batch.

Note that despite the measures taken to ensure simultaneous contact of the loading fixtures with the coupons, indications of asymmetric loading can be observed in the load-displacement curves. In particular, after passing through a first peak in load, some samples undergo a second, smaller peak. This second peak can be interpreted as a redistribution of stress within the sample: under a biased loading, at failure, the biased side complies, shifting the load towards the less compliant unbiased side. With the associated decrease in stress, the failed location tolerates a small increase in load until it fails fully. Note that an unbalanced load scenario leads to a conservative peak load: in the fully biased scenario (assuming 3-point bending with the load point located at 1/4 span) the effective stress is 33.3% lower than that estimated for 4-point bending.

From the flexural strength we can conclude that the introduction of 0.1x nutrient solution causes a negligible change in strength from TC15 to TC16_1 ($p = 0.065$). No significant difference is measured between TC16_1 and TC16_2 ($p = 0.504$) whereas TC16_3 presents a significant decrease compared to TC16_1 and TC16_2 ($p = 0.00053$), followed by a clear reduction for TC17. This suggests that the addition of nutrients and/or bacteria with or without MICP is detrimental to material strength.

As for flexural work of fracture, statistically significant differences are computed across coupons TC16_1, TC16_2, and TC16_3 ($p = 1.7 \times 10^{-5}$). Interestingly, there is an increased work of fracture measured for TC16_1 relative to TC15, approximately 200 %. This may be related to cross-linking or simply because more solid material is added. Conversely, all samples containing bacteria show lower work of fracture than the sterile control, although an increase is observed for TC16_3 relative to TC16_2. More data is necessary to conclude the causes of these differences with any degree of certainty.

4.2.4. Scanning electron microscopy

To determine the role of filament microstructure and MICP in the measured mechanical performance, SEM images were captured of post-mortem sample cross-sections. The resulting micrographs are displayed in fig. 4.9. In addition, single filaments were printed using various nozzle lengths and at different print speeds and micrographs taken of their cross-sections. The results are shown in figs. 4.9 and 4.10.

Starting with the coupon cross sections, two things can be immediately noted. First, as a positive result, filament outlines can be identified as a result of platelet alignment at the circumference. However, the extent of alignment appears to be limited, with only the very outer circumferential ring showing clear indications of aligned platelet stacking. Second, the cross-sections appear relatively consistent in texture across all coupons, meaning the comparison of mechanical properties is likely to be fair. Less fortunately, porosities can be observed in the form of spherical dark spots in both the interior and exterior, especially for the coupon of composition TC16_2. This further corroborates the high estimations of void content, and, given the steps endured to degas the inks, also highlights the difficulty in defoaming inks with high solid loading.

Moving to individual filament cross-sections and starting with the variation of nozzle lengths in fig. 4.10, we observe similar trends. Unfortunately, no discernable difference can be observed across the varying noz-

zle lengths. The rough topology is a key impediment in this assessment. Regardless, outer circumferences of filaments do again show some degree of alignment whereas the interiors remain largely disordered with arbitrarily located clusters of alignment. Porosity is also clearer in this case, although the larger holes may be related to material pull-out during fracture. Closely observing the filament exterior surfaces, we can observe widespread porosity. This can explain the relatively easy ingression of liquid observed during density estimations. Similar remarks can be made about the variation in printing speed. Clearly, it is much more difficult to obtain aligned filament cross-sections than initially presumed. The difficulty in obtaining clean, flat cross-sections such as those in fig. 2.6 is also emphasized.

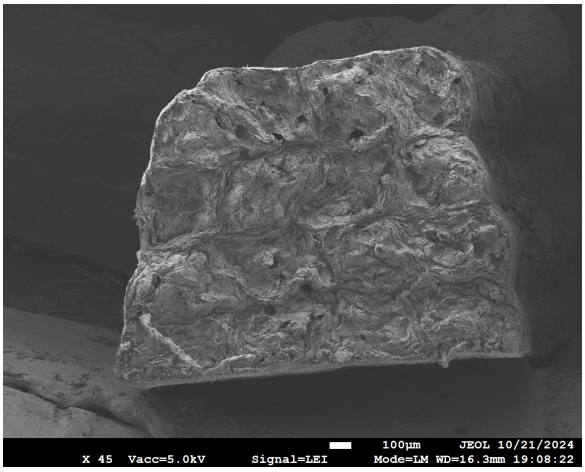

(a) TC15

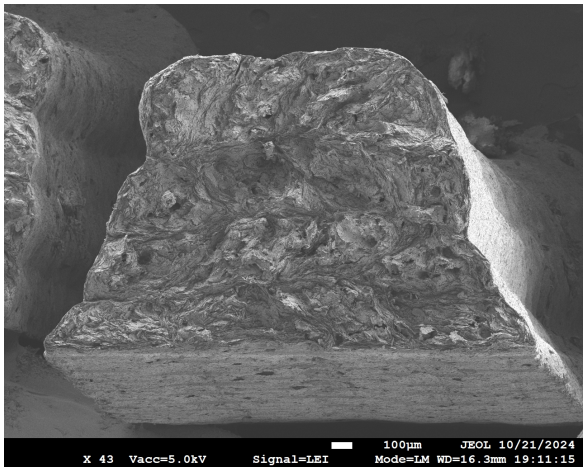

(b) TC16_1

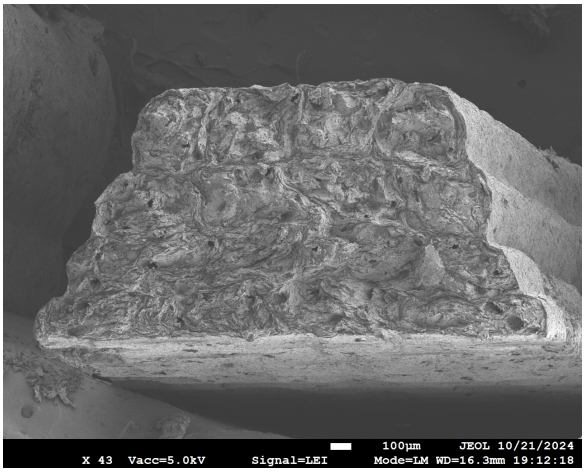

(c) TC16_2

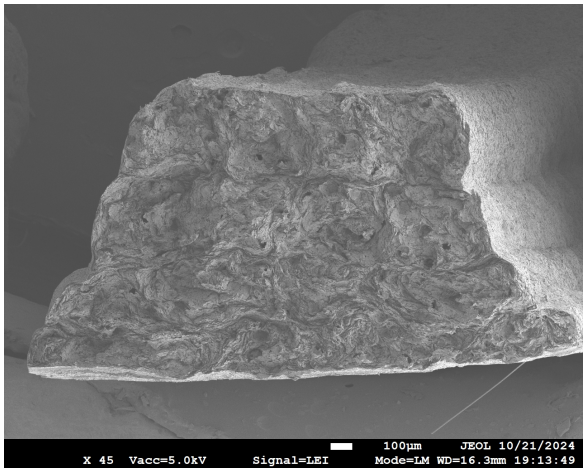

(d) TC16_3

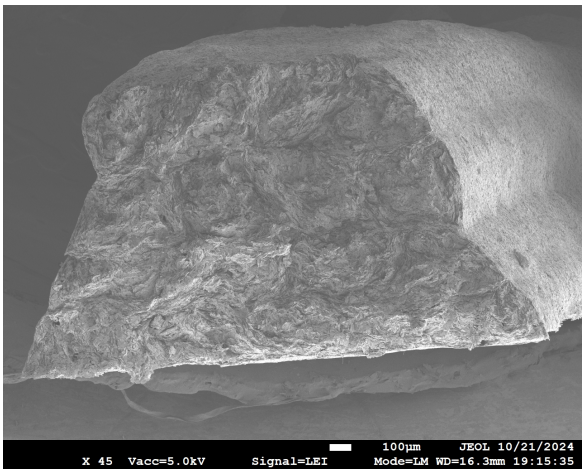

(e) TC17

Figure 4.9: Scanning electron micrographs of coupon fracture surfaces.

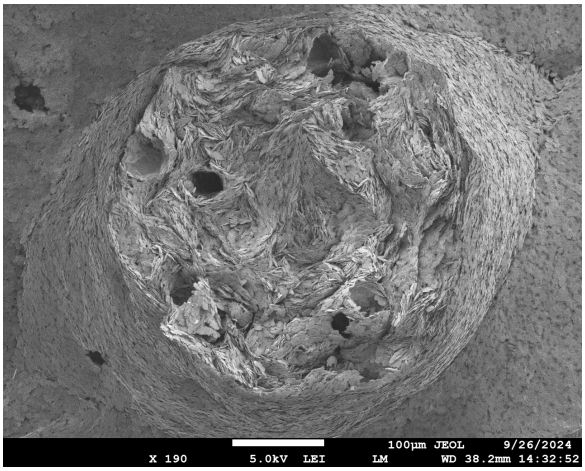

(a) 6.35 mm

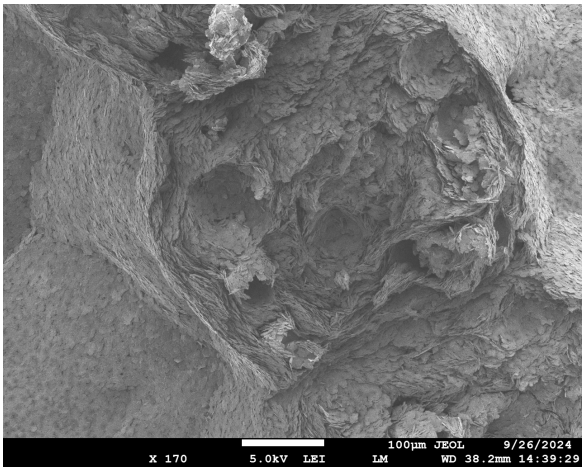

(b) 12.7 mm

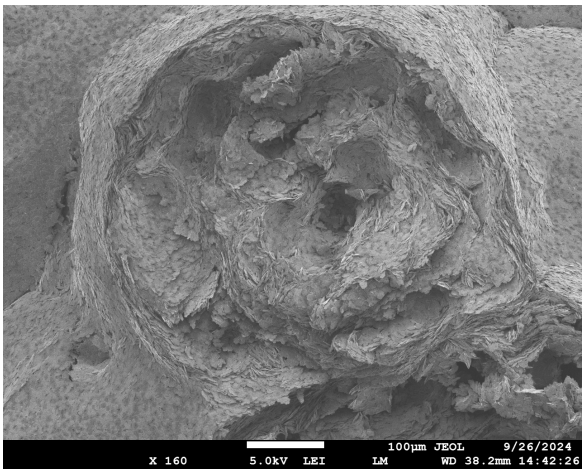

(c) 25.4 mm

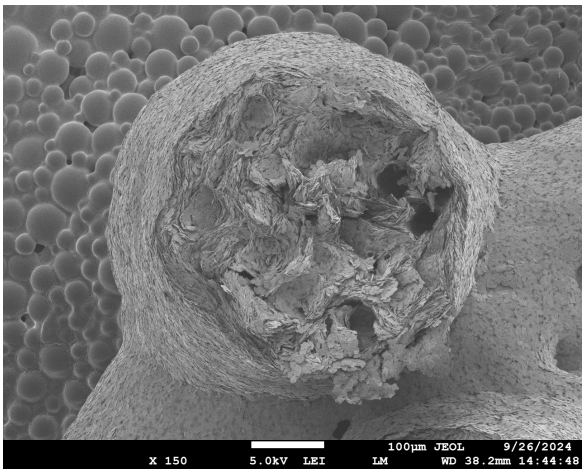

(d) 38.1 mm

Figure 4.10: Scanning electron micrographs of filament cross-sections for varying nozzle lengths.

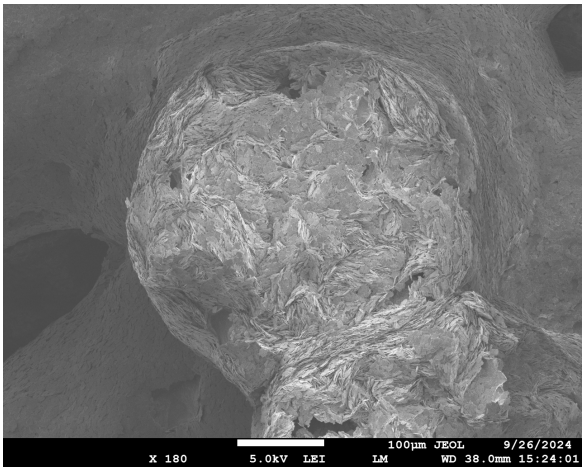

(a) 6.25 %

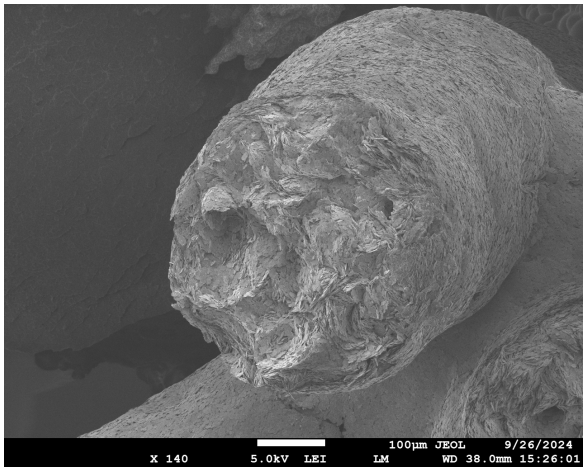

(b) 12.5 %

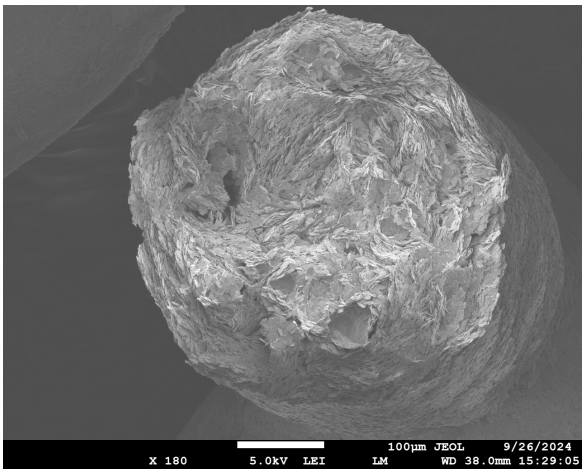

(c) 25 %

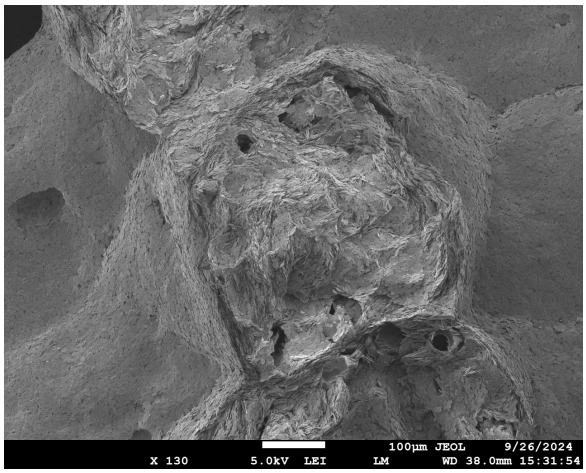

(d) 50 %

Figure 4.11: Scanning electron micrographs of filament cross-sections for varying print speed. Nozzle length is 38.1 mm. No clear differences in filament microstructure are discernable.

Regarding MICP the bacterial activity observed was limited. SEM scans of the sample surfaces revealed no calcium carbonate precipitates or rod-like bacterial shapes as previously seen for the PS/PC ink. This suggests that the reduced nutrient content hindered both precipitation and bacterial proliferation more strongly than initially expected, highlighting the importance of its optimization for achieving desired biomineralisation outcomes.

4.2.5. Thermogravimetric analysis

The thermal decomposition behaviour of the compositions was analysed in TGA as a measure for quantifying the presence of calcium carbonate. The resulting blank-subtracted weight-temperature curves are shown in fig. 4.12.

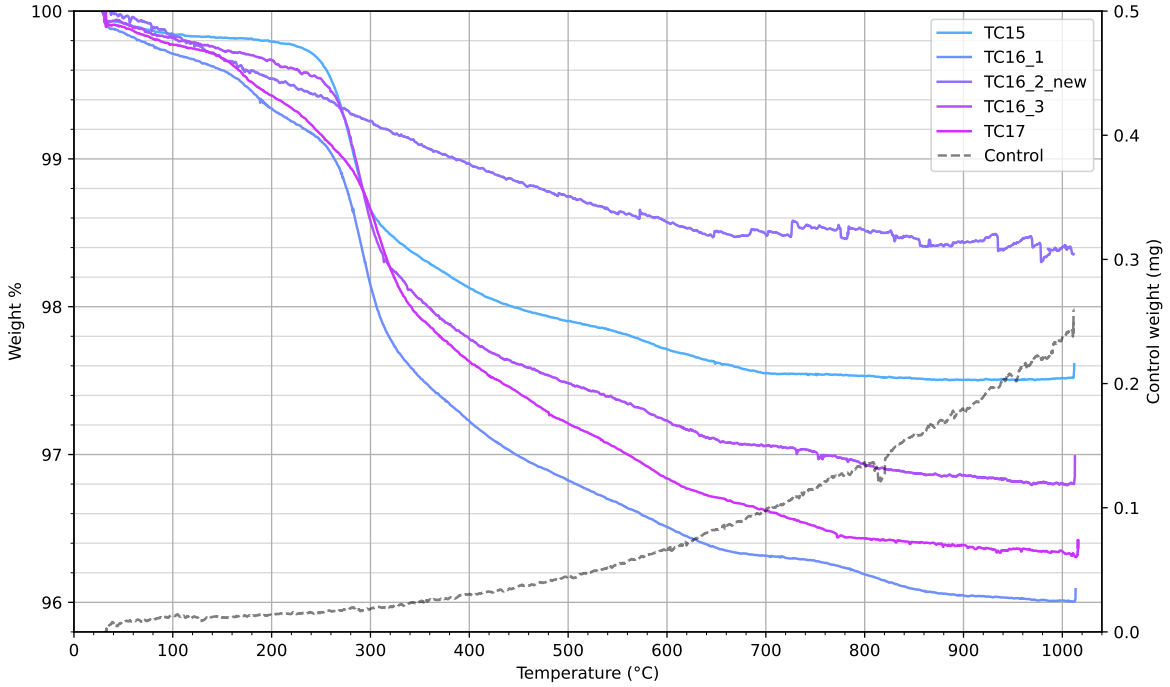

Figure 4.12: Sample thermal decomposition curves obtained via thermogravimetric analysis.

Immediately, no clear plateaus can be discerned in the region from 600 to 900 °C from which the weight proportion of calcium carbonate can be determined. Only composition TC16_1 appears to show limited plateauing in the region from 650–750 °C, which is unlikely to be a calcite-associated peak given the fact that it is a sterile control. Additionally, sample TC16_2 appears to be erroneous despite repetition, pointing to problems with the apparatus itself. Note also that the total weight changes are small due to the high (dry) ceramic content, possibly leading to a large spread and error in the curves. Unfortunately, this is also worsened by the high mass gain measured for the empty crucible which contributes significantly to the processed results. Possible reasons for this high mass gain are the buoyancy effect (which is repeatable and can be reliably subtracted) or an impure nitrogen source causing oxidation of the sample. At this stage of the project, insufficient time remained to further explore this. It is possible that better results are attainable using an oxygen-rich atmosphere. In that case, it should be taken into account that the unknown organics may cause weight changes in the same region as calcium carbonate.

4.3. Chapter summary

This chapter assessed the printed nacre-mimetic material's structural, mechanical, and compositional properties. Profilometry and Archimedes' method revealed significant shrinkage and void content both in the order of ~35 %. Mechanical testing reflects this high void content showing flexural strengths in the order of 1–5 kPa. Additionally, the addition of nutrients and bacteria was shown to reduce flexural strength and work of fracture, with higher concentrations worsening performance. SEM images revealed poor platelet alignment and no signs of bacterial activity or biomineralization, likely due to limited nutrients. The thermogravimetric analysis yielded inconsistent results, suggesting repetition is needed. Overall, the material's mechanical properties and microstructural control were suboptimal, and bacterial biomineralization was hindered, highlighting the need for improvements in ink formulation and processing approach.

This page has been intentionally left blank.

5

Discussion

In chapter 3, we looked at formulating an ink suitable for direct ink writing, followed by physical assessment in chapter 4. This chapter reviews the results of these chapters together and forms a comprehensive discussion. Key findings are summarised in section 5.1, interpreted with reference to literature in sections 5.2 to 5.4, and linked to key hypotheses in section 5.5. Limitations are addressed in section 5.6, and practical and theoretical implications are explored in section 5.7.

5.1. Overview of key findings

A preliminary ink formulation containing phyllosilicate (PS) platelets and powdered chitosan (PC) demonstrated excellent printability. Observation via SEM indicated the occurrence of MICP on the sample surface. Evidence of calcite precipitation within the filament cross-section was not observed. A second formulation containing alumina and high molecular weight chitosan (HMWC) exhibited much-reduced printability. Amplitude sweep and flow sweep measurements confirmed the reduction, showing a significant decrease in τ_y from 1.4×10^3 Pa to yield at rest, and $\overline{G'}$ from $\sim 4 \times 10^3$ Pa to $\sim 8 \times 10^1$ Pa.

A systematic parameter sweep reveals that τ_y and $\overline{G'}$ increase in a power-law manner with platelet content, whereas a non-trivial relation is observed for increasing HMWC content. The former could not be leveraged to obtain a printable ink as print fidelity remained low for all inks, even those satisfying the requirements posed by Feilden et al. (2017). Introducing a small wt% fumed silica as a rheological modifier did not improve printability. Replacing the HMWC, cellulose nanofibers (CNFs) yielded superior ink printability with alumina platelets, albeit still on the border of what can be considered satisfactory in absolute terms.

Adding nutrients was found to reduce printability strongly. In particular, an ink containing a much lower solid fraction than the maximum established for aqueous Al_2O_3/CNF could not be extruded at optimal nutrient concentrations, indicating a significant increase in viscosity. Diluting the nutrients to at least half the concentration resolved the printability issue while retaining theoretically sufficient nutrients for biomineralisation.

Al_2O_3/CNF inks containing varying nutrient and bacterial concentrations were prepared for physicochemical characterisation in chapter 4. After fully drying, samples shrunk by 36–40 %, an amount lower than expected for 100 % compaction (~75 %), indicating a high porosity in the order of 35 %. Estimations of void content using Archimedes' principle yield similar high values.

Flexural testing yielded strength values in the order of 5 kPa, with generally decreasing strength for increasing bacterial and nutrient contents. However, statistically insignificant differences were found for the lowest nutrient and bacterial content relative to both controls. The work of fracture tells a different story: statistically significant differences are observed between the two controls, showing a clear increase in work caused by adding a small concentration of nutrients. The introduction of bacteria is detrimental: all inoculated inks perform worse than the sterile control. The lowest strength and work of fracture values were found for the sample containing the highest nutrient and bacterial content.

Scanning electron micrographs of the coupon cross-sections reveal evidence of platelet alignment only in the outermost ring of each filament. However, most of the filament interiors remain disordered. This microstructure appears consistent across all coupons. SEM performed on individual filaments printed with varying print speeds and nozzle lengths yield the same results: a thin outer ring of well-aligned platelets en-

closing a disordered interior. The degree of alignment was impossible to quantify due to poor cross-section quality, and no pattern was distinguishable across the varied printing conditions. Despite using similar inoculum concentrations as for the initial PS/PC ink, no $CaCO_3$ deposits nor bacteria could be identified within or covering the coupons. TGA curves yield no practical results, requiring repetition in different conditions.

There are four key points of interpretation here. First, a significant difference in printability is observed for samples containing the same weight-wise composition but using different components. Second, the metrics of printability used by Feilden et al. (2017) seem insufficient for guaranteeing printable inks. Hence, additional constraints on ink rheology are likely missing. Third, platelet alignment has remained highly limited throughout printing experiments, and the high degree of alignment obtained by Feilden et al. (2017) has not been replicated. Last, the occurrence of MICP could not be linked to mechanical properties since evidence of it is lacking, although results for the PS/PC ink are promising.

5.2. Rheology and the differences across compositions

The difference in the printabilities of PS/PC and Al_2O_3/HMWC inks imply extensive differences in the interactions occurring at the molecular scale. The sources of these changes are related to the change in polymer and/or platelets. Increased molecular weight is expected to increase viscosity, yield stress, and storage modulus due to increased entanglement and interactions between molecular chains (Wang et al., 1991). This change was noticeable in practice as it was remarkably more difficult to dissolve than the powdered variant, requiring prolonged heating and filtration in its gelled state to prevent nozzle clogging during printing. However, we observe the opposite effect here, implying that the platelets dominate the viscoelastic behaviour.

Bearing this logic in mind, recall the deformation-related motivation for the change in platelet type mentioned in section 3.2. In hindsight, it makes sense that the PS/PC demonstrated such vastly superior printability. The crystal plane-sliding deformation in phyllosilicates is responsible for the excellent mouldability of wet clay (Breuer, 2012); it is an ideal solid for printing, hence why it has proved difficult to compete with.

Besides differences in deformation behaviour, the geometrical differences are also likely to play a role, although larger and more disperse particles (the PS platelets) are expected to yield less viscous suspensions (Ancey, 2001; Ancey et al., 2001), so in this case this role is probably minor. In contrast, surface chemistry is a driving consideration in colloidal suspension rheology, especially for ceramics (Lewis, 2000; Smay et al., 2002; Lewis, 2006; Lewis et al., 2006; Franks et al., 2017).

5.2.1. Relation of rheology to colloid chemistry

Whereas phyllosilicates contain a certain ratio of both tetrahedral (hydrophobic) silica and -OH modified (hydrophilic) alumina (Breuer, 2012), the alumina platelets are hydrophilic alone. This difference in surface charge changes two strong interactions. First, larger hydration forces are experienced for suspensions of alumina. There is a lower tendency to aggregate, which translates to higher viscosity and yield point (Au et al., 2014; Anton Paar, 2024). Second, electrostatic repulsion forces, represented by the magnitude of the so-called zeta potential, differ greatly between suspensions of the two particles as shown in figs. 5.1a and 5.1b.

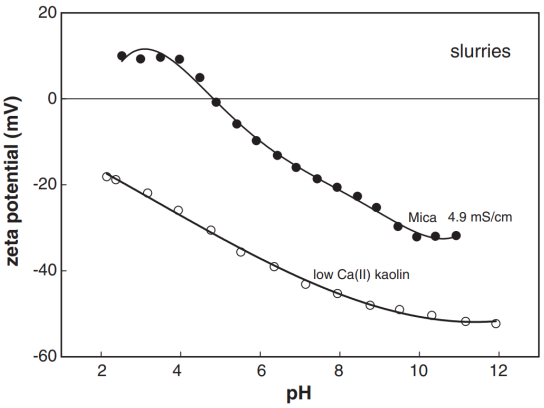

(a) Zeta potential of mica and kaolin slurries for varying pH as measured by Au et al. (2014).

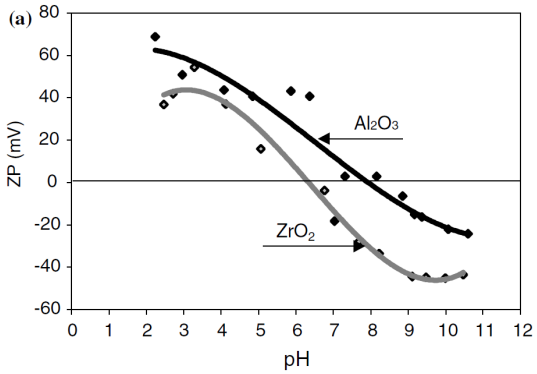

(b) Zeta potential of alumina for varying pH as measured by Novak and Kalin (2004).

Figure 5.1: Differences in zeta potentials for phyllosilicate and alumina suspensions. Negatively charged particles attract positive charge; hence, at sufficiently low pH, the zeta potential is positive.

The zeta potential describes the charge present at a small distance from the particle surface. At the low pH (~4.5) of acetic acid solutions, both mica and kaolin display lower magnitude zeta potentials than alumina. Up to a pH of about 5, the opposite charges of mica and kaolin mean that the platelets will experience electrostatic attraction instead of repulsion. These differences in hydration and electrostatic forces convey that mica/kaolin platelets will experience increased flocculation tendency compared to alumina platelets and, therefore, exhibit higher yield stress and storage modulus.

Particle-polymer interactions are also likely to play an important role. Polymers that tend to adsorb to colloids can give rise to steric repulsions, which prevent aggregation. This adsorption behaviour can depend strongly on particle charge. Observe the zeta potentials shown in fig. 5.1b, and compare to those of alumina and mica/kaolin: both alumina and chitosan demonstrate a high positive zeta potential at low pH, whereas these repulsions are much lower or even attractive for mica/kaolin dispersions. Similarly, the switch to cellulose would result in attractive forces between the polymer and the alumina, possibly explaining the improved results obtained with Al_2O_3/CNF.

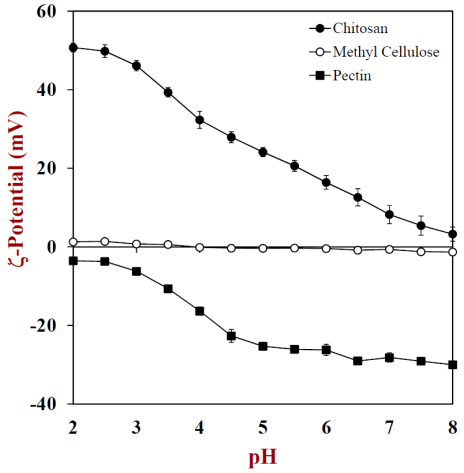

(a) Zeta potentials of chitosan, methylcellulose, and pectin for varying pH as measured by Espinal-Ruiz et al. (2014).

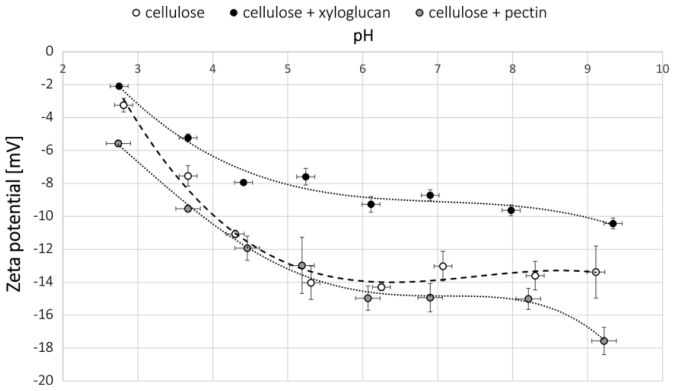

(b) Zeta potential of cellulose for varying pH as measured by Myśliwiec et al. (2016).

Polymer adsorption and steric repulsions often depend on molecular weight since longer molecules provide more contact points and can 'wrap' around colloid particles. This can cause greater steric repulsions and thus decrease aggregation tendency. Alternatively, longer polymers interact at greater distances, impeding the disruption of the hydrogel network responsible for shear thinning. The physical differences observed in practice suggest that this is indeed an important factor.

In summary, a range of molecular interaction differences suggests a stronger aggregation and shear thinning tendency for the phyllosilicate particles than for alumina. Of course, somewhere here, there lies a balance. Higher attractions lead to higher shear forces required for flow, so there must be a trade-off between aggregation, i.e. shape retention, and extrudability. The zeta potentials of (primary) ink constituents may serve as valuable metrics for achieving this balance.

5.2.2. pH changes can induce strong coagulation

Given the dependence of colloidal interactions on pH, one should closely monitor changes in pH caused by different ink constituents. This was not controlled for throughout this thesis. I suggest that the reduction in printability caused by the reintroduction of nutrients results from this change in pH, possibly magnified by a more substantial presence of ions in solution. A simple measurement reveals that the pH of 1x nutrient solution is approximately 6.0, whereas that of MilliQ water is 5.3. While small, the difference may strengthen aggregation sufficiently to cause non-printability.

This pH dependence can perhaps be leveraged to induce aggregation in a controlled manner. At the time of writing this discussion Dutto et al. (2025) published a demonstration of this concept. After casting a fluid-like ceramic colloid containing *S. pasteurii* into a mould, ammonia production via ureolysis induces a pH increase, triggering coagulation of the slurry and leading to a part strong enough to be post-processed without damage. The authors show that the coagulation dynamics can be controlled by changing bacterial and nutrient concentrations. Similarly, one could trigger filament coagulation by printing into a bath at a high pH, allowing looser constraints on the ink's rheology.

Notably, similar coagulation behaviour was observed in this thesis (section 3.1), where adding 2x concentrated *S. pasteurii* inoculum rendered the preliminary ink non-extrudable within 10 minutes. While linked to bacterial activity, this seems more likely driven by such pH-controlled coagulation than by stiffening through biomineralisation. Promisingly, Dutto et al. (2025) did not investigate the possibility of biomineralising their slurry. Future studies could investigate its impact not only on mechanical properties but also on coagulation behaviour.

5.2.3. Evidence of time dependency

The inks investigated in this thesis have so far been modelled as Herschel-Bulkley fluids (eq. (2.12)). This involves assuming time-independent values of yield stress τ_y, flow behaviour index $n > 0$, and flow consistency parameter $k > 0$. The general lack of printability and platelet alignment brings these assumptions into question and motivates a closer look at the rheology data, revealing a particularly unexpected behaviour, shown in fig. 5.4.

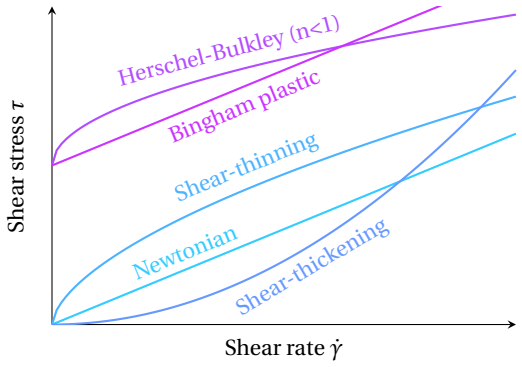

Figure 5.3: Expected shear stress responses for time-independent viscoelasticity models (del-Mazo-Barbara and Ginebra, 2021).

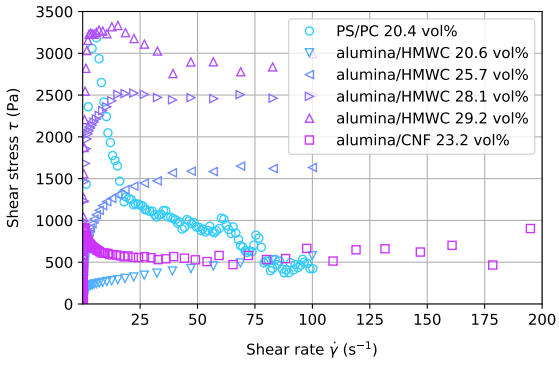

Figure 5.4: Comparison of shear stresses versus shear rates experienced by different ink compositions during flow sweep measurements.

Compare these results to fig. 5.3. Whereas Al_2O_3/HMWC inks up to 25.7 vol% demonstrate shear-thinning Herschel-Bulkley type curves, those at higher volume fractions, in addition to the PS/PC and Al_2O_3/CNF inks, display behaviour that cannot be fitted using any of the time-independent models. This is especially evident for the PS/PC ink. It is safe to rule out measurement artefacts such as wall slip since we are using serrated plates and because gap analysis in amplitude sweep measurements showed a negligible difference in shear rate measurements (appendix D.3). A different explanation is necessary.

A strong candidate is that the ink rheology contains a time-independent component that leads to shear thinning, similar to thixotropy (Cheng, 1987; Zhu and Smay, 2011; del-Mazo-Barbara and Ginebra, 2021). In particular, as the measurement progresses, the increasing time under shear is accompanied by structural breakdown. Lower shear resistance is measured, which, in this case, dominates the shear response of the material. The resulting 'effective' shear stress versus shear rate behaviour is showcased by Zhu and Smay (2011) in fig. 5.5.

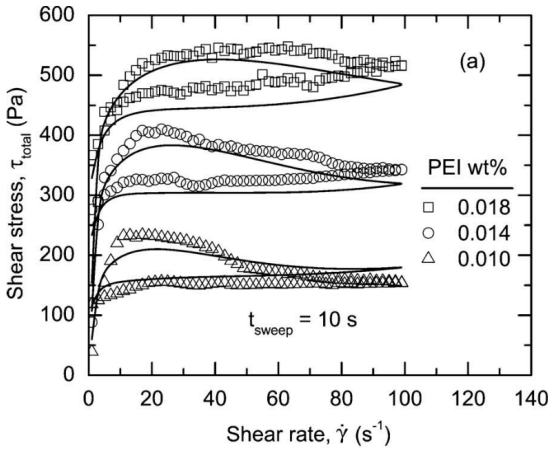

Figure 5.5: Hysteresis loops (shear rate ramp up and ramp down) for highly concentrated colloidal Al_2O_3 inks containing varying amounts of poly(ethylenimine) (PEI) flocculant. Taken from Zhu and Smay (2011).

Time-dependent phenomena such as thixotropy are apparently well-known and have been observed and modelled extensively in literature, including for spherical alumina colloids used in 3D printing (Zhu and Smay, 2011). This was, unfortunately, previously unknown to me. While an extensive discussion of modelling approaches shall be avoided, modelling this generally involves the introduction of a structural parameter $0 \leq \lambda \leq 1$ into constitutive equations such as the Herschel-Bulkley model, or models that decouple elastic and viscous stress such as that of Dullaert and Mewis (2006) and Zhu and Smay (2011). The parameter is commonly made a function of time and fluid state, thereby conveying structural kinetics such as floc attrition and aggregation (Zhu and Smay, 2011). In our case, it could convey the rearrangement of platelets, allowing modelling of the current ink's behaviour. Strictly speaking, thixotropy is completely reversible through Brownian motion (Barnes, 1997), whereas shear-induced alignment may not be as a result of the strong shape anisotropy and accompanying stacking behaviour. This should be considered when forming models in the future.

Crucially, time-dependent behaviour does not emerge when plotting viscosity against shear rate since it appears simply as a steeper shear thinning gradient. More importantly, strong time dependency invalidates the rheological model and implies that values obtained for inks at rest do not accurately represent the behaviour of the printed material. Therefore, these values cannot be used as predictors of printability. This finding is critical for understanding why, in this thesis, inks that satisfy printability requirements do not demonstrate satisfactory printability.

Obtaining more accurate values may fortunately be as simple as shearing the material at rates and times representative of extrusion and performing similar analysis afterwards (Zhu and Smay, 2011). Various measurement techniques exist for obtaining indications of structural change and the timescales involved when going from a rested material (i.e. in the syringe) to a previously sheared material (i.e. extrudate). One such method is the three-interval thixotropy test (3ITT), which yields the elastic recovery of the material (del-Mazo-Barbara and Ginebra, 2021). Insightfully, del-Mazo-Barbara and Ginebra (2021) clarify that $\overline{G'}$ and τ_y are but a few among a variety of parameters that form predictors of extrudability and shape fidelity. This third metric, elastic recovery, may be critical for explaining the lack of printability observed in the current inks. This has been briefly explored in appendix D.4; indeed, a significant, permanent decrease in viscosity is observed before and after shearing.

Data on what is considered 'sufficient' elastic recovery is incomplete, but the recovery should occur within seconds, and the recovered stiffness should be above the minimum for shape retention. In fact, most predictors of printability do not have hard-set requirements as implicitly suggested by Feilden et al. (2017), but

carry ranges of values that have shown positive results for different studies with different colloid systems (del-Mazo-Barbara and Ginebra, 2021).

Notably, the shear stress - shear strain curves shown in fig. 5.4 indicate more significant time-dependent (i.e., restructuring) behaviour for PS/PC and Al_2O_3/CNF inks than for Al_2O_3/HMWC inks. This further supports the suggestion that the PS/PC inks deform largely by PS crystal plane sliding. Note also the onset of time-dependent behaviour at high platelet volume fractions in Al_2O_3/HMWC inks, suggesting increased restructuring.

5.3. Lack of platelet alignment

Comparing the present results to those obtained by Feilden et al. (2017) shown in fig. 2.6, we observe an evident lack of structural organisation that requires more attention. Nozzle exit and aggressive corner flow at the extrusion end could be a source. These sudden changes in flow conditions introduce high shear, which may reduce alignment. Mezi et al. (2019) demonstrate using numerical simulation that the flow-wise alignment of fibres reduces dramatically after exiting the nozzle due to an outward flow of material, with the middle streamlines becoming fully perpendicular to the extrusion direction. However, this perpendicularity is observed neither here nor by Feilden et al. (2017). The corner flow appears to be negligible for similar reasons. A different argument is necessary.

An alternative explanation relates to the flow within the nozzle as depicted in fig. 5.6. Due to the radial shear stress gradient in the nozzle, an ink with a given yield stress yields only in the region outside of a core where the stress is below the yield stress (Siqueira et al., 2017; Hausmann et al., 2018; Balani et al., 2021; Wilms et al., 2021). Since particles require a minimum 'residence time' under shear to align, the region outside of the plug flow where shear *stress* is high but shear *rate* is low also experiences reduced alignment (Feilden et al., 2017; Hausmann et al., 2018). The combined effect is a filament containing a highly aligned outer layer, whereas the core remains largely disordered. This is precisely what we observe.

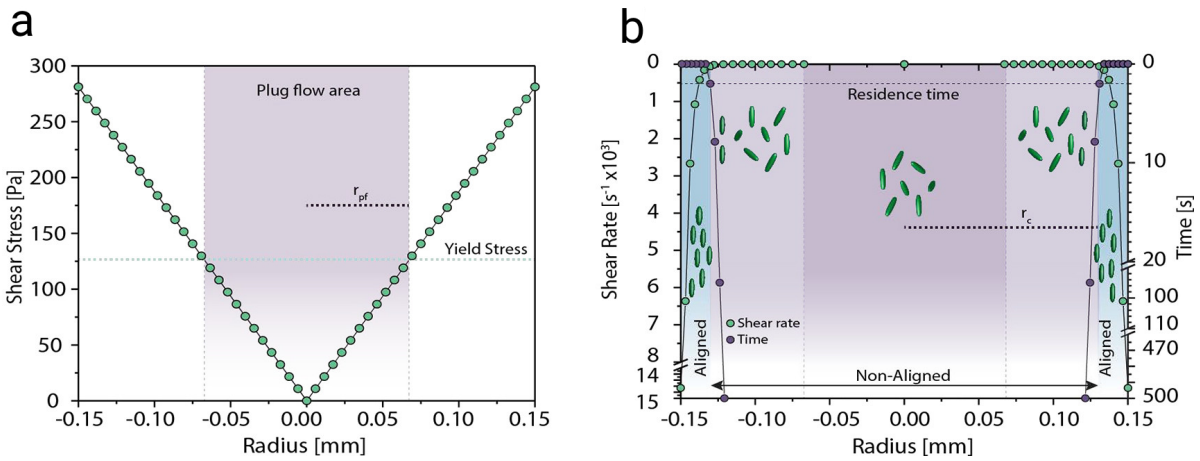

Figure 5.6: Shear stress distribution across a 0.3 mm diameter, 80 mm length nozzle as determined by Hausmann et al. (2018) **(a)**. The yield stress for this CNC-loaded ink is shown as a horizontal dotted line, forming a plug flow regime of radius r_{pf}. Shear rate profile and alignment times across the nozzle radius, showing the formation of a large unaligned zone of 'differential flow' outside of the plug flow regime, containing a thin, highly aligned zone demarcated by the sudden increase in residence time **(b)**. Taken from Hausmann et al. (2018).

To further understand this, for a Herschel-Bulkley fluid, shear thinning increases this non-aligned or 'critical' radius by widening the region where shear rates are low, as depicted in fig. 5.7. Hausmann et al. (2018) provide an estimation of this critical radius r_c in eq. (5.1):

$$r_c = r_{pf} + \frac{2K}{\Delta P} L^{1-n} \left(\frac{\beta(\Phi) Q}{R^2 \pi} \right)^n \tag{5.1}$$

Where β is a constant that captures the inherent alignment behaviour of the ink, which is made a function only of the particle volume fraction Φ. Q is the mass flow rate, and the plug flow radius r_{pf} can be determined from eq. (2.15) by equating to zero, yielding:

$$r_{pf} = \frac{2\tau_y L}{\Delta P} \tag{5.2}$$

Which clearly shows the dependence on yield stress and flow behaviour index. Curiously, the plug flow radius increases only with τ_y since ΔP is linearly correlated to L. Hence, the size of the unyielded core can be determined from the rheology of the ink alone, and one should favour lower yield stresses.

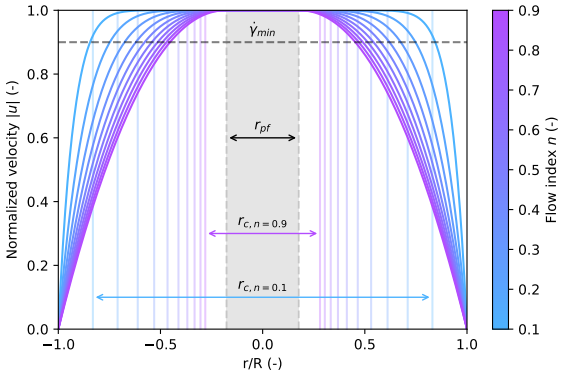

Figure 5.7: Nozzle velocity profiles for varying flow behavioural indices, showing a widening of the critical radius. The plug flow radius r_{pf} is independent of n and remains constant. Here a fictitious residence time is represented as a minimum shear rate $\dot{\gamma}_{min}$ below which no alignment occurs. The critical radii corresponding to these residence times are depicted by vertical lines to demonstrate the effect of shear thinning on the degree of alignment.

The above equations do not apply to the inks studied here due to the substantial time dependence. However, they provide helpful insight. Since the current inks experience reduced shear resistance after exposure to stress, and since the outer, slowest layers experience the highest shear, the shear thinning behaviour is essentially strengthened at the outer layers, leading to further widening of the shear profile. Hence, reducing this time-dependent shear thinning is desirable. Alternatively, formulating an ink that experiences *increased* shear resistance with increased alignment ratios would be beneficial. The shear profile then narrows due to an inwards-growing shear-thickening layer, promoting further alignment in the unaligned regions.

In summary, the current ink rheologies are not optimised in terms of velocity profile and shear-induced alignment behaviour, leading to the low alignment observed. The rheology should be improved by minimising eq. (5.1) using the properties for pre-sheared material. As a first rough guideline, this involves minimising the yield shear stress and maximising the flow behaviour index n while retaining printability.

5.4. Bacterial activity

For the initial PS/PC ink, precipitates with the morphology of calcium carbonate deposited via MICP were found on the outside print surface. None were found inside the filament interiors. For the Al_2O_3/CNF inks, no evidence of MICP could be found. For the latter, reduced nutrient content is likely the cause. However, the limited results for the PS/PC ink remained unclear previously and may be the result of a paradox that is only apparent since the coagulation behaviour was revealed in section 5.2.2: the inclusion of bacteria rapidly triggers a change of pH, which leads to coagulation and subsequent non-printability. Consequently, an ink that stimulates MICP is not printable, and an ink that does not shows no MICP. Therefore, a balance must be struck between inoculating the ink with sufficient bacteria to trigger MICP and not too much to cause short-term aggregation and non-printability. This 'printability window' should be considered when formulating inks for the current approach.

More interestingly, given the rapid coagulation time after the addition of *S. pasteurii* shown both here and by Dutto et al. (2025), I suggest that it may be possible to mix the bacteria into the ink during extrusion in a multimaterial approach, thereby extruding as coagulation takes place. In this way, the bacteria function as a 'hardening agent' that allows increased filament retention upon deposition.

5.5. Key hypotheses

Condensing the above discussion and main findings, we arrive at three key hypotheses that are most relevant for future studies:

Hypothesis 1: Optimising ink rheology

The rheology of the formulated inks can be improved via small changes in composition. Keeping an approximately similar ratio of ceramic and polymer, aggregation tendency can be controlled via zeta potential behaviour, pH, and polymer molecular weight to yield a favourable balance between fluidity and structure. This hypothesis can be tested by selecting components that lead to pH-dependent aggregation tendency, varying pH, and MW and observing the corresponding changes in rheology and printability.

Hypothesis 2: pH-based ink coagulation

***S. pasteurii* induces pH-based coagulation.** A 'printing' window exists which requires delaying bacterial activity sufficiently to allow printing but not so much as to prevent MICP from occurring. A multimaterial approach can leverage this to allow immediate coagulation, thereby improving print fidelity. This can be tested by varying bacterial content in inks containing urea but lacking biomineralisation feedstock, similar to the study by Dutto et al. (2025).

Hypothesis 3: Time-dependent ink rheology

Rheological properties of the inks depend on shear history. Hence the ink behaviours cannot be adequately described by the Herschel-Bulkley model as used by Feilden et al. (2017). Rheology data obtained at rest becomes insufficient for predicting the extruded material's behaviour. Whether such time dependency is required for successful printing and if platelet alignment plays a role in this remains unclear. This is critical to investigate since it, if true, places a fundamental constraint on the rheology of nacre-inspired inks. This hypothesis can be tested by performing rheology experiments that test or incorporate shear history and quantifying platelet alignment in parallel.

Hypothesis 4: Improving mechanical behaviour

Mechanical behaviour can be improved by increasing compaction and minimising shrinkage. The large void content should be reducible by increasing the solid fraction to decrease mass loss on drying while promoting the mobility of the polymer. This can be tested by varying solid and polymer content.

5.6. Limitations of the current experimental approach

While many choices in this study were motivated by achieving mechanical strength, it must be made clear that this work is not an optimisation of mechanical strength. Instead, the goal is to chart the design space for printing bacteria- and platelet-loaded hydrogels so that the microstructure involved in the toughening mechanisms observed in natural nacre can be replicated. At the same time, the materials obtained here bear insufficient resemblance to nacre to be fairly labelled 'nacre-mimetic'. Warranting this label would require proper implementation of the guidelines mentioned in section 2.4. The platelet aspect ratio s would have to be optimised for a given polymer and platelet material so that $s \lesssim \frac{\sigma_p}{\tau_y}$. To demonstrate, assuming a perfect interface, cellulose as the polymer (τ_y ~300 MPa (Zhang et al., 2015)) and alumina platelets (theoretical σ_p 46 GPa), the critical platelet aspect ratio should ideally be in the order of

$$s_c = \frac{46\,\text{GPa}}{300 \times 10^6\,\text{Pa}} \approx 150 \tag{5.3}$$

The alumina platelets used in this study deviate by a factor ~ 2.

Even using the correct aspect ratio, the printed material should at least consist of a layered structure of tightly stacked ceramic platelets embedded in a polymer matrix as described in section 2.4. In section 4.2.4, micrographs reveal that such a layered microstructure is absent. Void content estimations suggest that the space between platelets is largely empty and devoid of polymer. To become a proper representation of nacreous material, the particles should ideally be fully dispersed, aligned, and embedded in polymer. The latter may possibly be achieved by adsorbing polymers onto suspended platelets instead of dissolving the polymer

directly into a highly loaded suspension as done here. Crucially, the platelets used here are not convex, meaning that tablet interlocking will not occur even in an aligned state. This feature is critical for replicating the toughening mechanisms in nacre and should, therefore, be included in any potential optimisation studies. In the end, natural nacre exists within a two-layer armour system, which will behave differently than nacre on its own.

5.7. Implications for theory and practice

The findings and hypotheses proposed in this study hold important implications for both conceptual understanding and practical application of MICP in bioprinting. From a theoretical perspective, colloidal stability and structure seem to play much more important roles than initially implied. Little data is available on the conditions governing the stability of highly anisotropic platelet-loaded colloids, therefore the current evidence forms an incentive for expanding this knowledge.

Crucially, the effect of platelet alignment on ink rheology and vice versa is a topic requiring more attention. It makes logical sense that platelet alignment should affect ink rheology since the ink structure becomes highly anisotropic. Varying packing ratios for different degrees of alignment are likely to facilitate or impair sliding, implying that time dependency may be fundamentally linked to shear-induced alignment. Understanding this relationship may be key to unravelling the rheology of nacre-like inks.

The need for precise control of MICP in the current direct ink writing approach is evident. The existence of a printing window before coagulation occurs sets an important constraint on bacterial activity and/or the printing process. Requiring precise control also presents a case for the genetic engineering of bacteria, a field that is advancing quickly and could, therefore, provide useful new tools in this situation (Gilbert and Ellis, 2019). A new multimaterial approach is suggested to streamline the process of DIW with MICP by inoculating during printing and triggering coagulation immediately, possibly allowing a new method for fabricating robust biocomposites.

This page has been intentionally left blank.

6

Conclusions and perspectives

This chapter concludes the current study and reflects on the extent to which the initially set research objectives have been answered. Conclusions are provided section 6.1, which have been structured to answer the research questions. Recommendations for future studies are made in section 6.2, followed by a summary of scientific significance in section 6.3.

6.1. Conclusions

This study aimed to characterise the printing process, bacterial activity, and resulting material for nacre-mimetic composites using biomineralising bacteria in direct ink writing (DIW). Despite the challenges, significant progress was made, outlined below:

1. How must an ink be formulated to achieve a microstructure resembling nacre via direct ink writing?

A microstructure resembling nacre can be achieved through shear-induced alignment of platelets. This work demonstrates that achieving this behaviour is not trivial. Alignment is dependent not only on the presence of shear flow but also on the radial profile of this shear flow inside the nozzle. Shear thinning, which is desired for printing, is then undesired for alignment because it biases high shear flow towards the nozzle wall, preventing reorientation of the inner parts of the filament. A high yield stress aggravates this by forming a large 'plug flow' region. Hence, ink constituents must be chosen to minimise shear thinning effects and yield stress while retaining printability.

Rheology is found to be time-dependent, invalidating typical rheological models such as the Herschel-Bulkley model as used in comparable work by Feilden et al. (2017). A more advanced method describing time-dependent structural changes is required. The target rheology should be sheared material rather than material at rest to retain printability. Sufficient yield shear stress and stiffness should then be measured. This forms a second trade-off, where yield shear stress must be high enough to allow shape retention but minimised to promote platelet alignment. Rheological values do not vary trivially with constituent content. Ink yield shear stress and stiffness were found to vary in a power law relation with ceramic content but varied non-linearly with polymer content. This contrasts with the behaviour observed for other systems (del-Mazo-Barbara and Ginebra, 2021).

2. How do printing conditions affect printability and microstructure?

Nozzle aspect ratio and print speed directly affect the flow shear profile. Higher aspect ratios and print speeds are desired because they subject the ink to more pronounced shear. In the current work, however, the effect of higher print speeds on printability was noted but could not be linked to microstructure. The lack of a trend in microstructure across different printing conditions implies that shear-induced alignment is dominated by rheology and not by printing conditions.

3. How do ink constituent quantities relate to bacterial activity, microstructure and the corresponding mechanical behaviour?

Inks containing 1-fold nutrient solution concentrations demonstrated biomineralisation on the material surface. Below the surface, the presence of bacteria or mineral deposits could not be identified, either because the current quantification approaches were insufficient or because the bacterial activity is hindered within the filament. This must be verified in the future. At 0.5-fold concentration, all signs of bacterial activity were lost, implying a minimum between 0.5-fold and 1-fold concentration. Similarly, inoculum concentrations were varied to control bacterial activity with optimal results achieved by adding 2 vol% of 0.5-fold incubated growth medium. Below this value, no precipitation is observed. Above it, microbially-induced pH change causes ink coagulation, preventing extrusion. Hence, a 'printing window' is established for the current system. The presence of bacteria and nutrients proved detrimental to flexural strength but had varying effects on the work of fracture. Since these numbers were evaluated at 0.5-fold nutrient concentration, the negative influence is likely caused by the presence of nutrients and bacteria, not biomineralisation. Hence, any potential positive effect of biomineralisation should compensate for this adverse effect.

6.2. Recommendations for future work

The following recommendations are made based on the findings and experimental work conducted in this thesis:

1. **Optimise ink formulation**
    - Future formulations should focus on colloidal stability. Understanding colloidal interactions, controlling pH, and investigating surface treatments such as polymer adsorption to achieve a fully dispersed, polymer-enriched platelet network with the right balance between aggregation and mobility may enable successful ink formulations.
    - Higher ceramic volume fractions achieved using dispersants should be investigated as a way to reduce shrinkage.
2. **Advance understanding of anisotropic colloid rheology**
    - Rheological testing should incorporate shear history representative of the extrusion process and structural recovery assessments to evaluate structural breakdown and elastic recovery. Suitable models should be developed or applied that take into account colloid anisotropy.
    - Changes in velocity profiles caused by different ink behaviours should be investigated, ideally coupled with rheology and linked to particle alignment.
    - As a first measure for achieving increased alignment, the ink should be optimised to minimise yield shear stress and shear thinning while remaining printable.
    - Better quantitative approaches for platelet alignment, for example, Wide-Angle X-ray spectroscopy (WAXS), should be used.
3. **Enhance bacterial activity and MICP and improve characterisation approach**
    - To increase MICP, future work should aim to optimise MICP behaviour, e.g. via tuning nutrient and/or oxygen availability or by using slow-release nutrient systems to ensure bacterial viability without compromising printability.
    - Alternatively, a multimaterial approach where bacteria are added during extrusion to trigger coagulation immediately may provide a new method for producing strong parts that induce biomineralisation.
    - Combined approaches should be used to quantify MICP, e.g. by combining Scanning Electron Microscopy and Energy Dispersive X-ray Spectroscopy (SEM/EDS), thermogravimetric analysis (TGA), or other methods such as computed tomography. Attention should be given to the conditions in TGA that facilitate the quantification of calcium carbonate, i.e. those that allow for distinguished plateaus in mass loss. The mechanical influence of MICP on materials remains a topic to be explored.

6.3. Significance of this work

In summary, this research contributes to understanding the requirements for printing nacre-inspired materials via direct ink writing (DIW) and microbially induced calcite precipitation (MICP) as a pathway to mechanically enhance nacre-inspired materials. By examining how different formulations and bacterial activity influence printability, microstructure, and mechanical performance, a groundwork is laid for future investigations into sustainable, bioinspired structural materials.

The following points are highlighted as key contributing knowledge:

- Rheology of platelet-loaded inks can be time-dependent;
- Time-dependency complicates nozzle shear flow and invalidates standard rheological models such as the Herschel-Bulkley model for predicting alignment and printability;
- Requirements for rheology in the context of direct ink writing should thus be set on sheared material;
- To maximise shear-induced alignment, yield shear stress and shear thinning index should be set to the minimum and maximum, respectively, required for printing.

This page has been intentionally left blank.

Bibliography

Almqvist, N., Thomson, N. H., Smith, B. L., Stucky, G. D., Morse, D. E., & Hansma, P. K. (1999). Methods for fabricating and characterizing a new generation of biomimetic materials. *Materials Science and Engineering: C*, *7*, 37–43. doi:10.1016/s0928-4931(98)00072-1

Anbu, P., Kang, C. H., Shin, Y. J., & So, J. S. (2016). Formations of calcium carbonate minerals by bacteria and its multiple applications. *SpringerPlus*, *5*, 1–26. doi:10.1186/S40064-016-1869-2

Ancey, C. (2001). Role of lubricated contacts in concentrated polydisperse suspensions. *Journal of Rheology*, *45*, 1421–1439. doi:10.1122/1.1413504

Ancey, C., Jorrot, H., Rheol, J., & lè ne Jorrot, H. (2001). Yield stress for particle suspensions within a clay dispersion. *Journal of Rheology*, *45*, 297–319. doi:10.1122/1.1343879

Anton Paar. (2024). The influence of particles on suspension rheology. Retrieved October 28, 2024, from https://wiki.anton-paar.com/nl-en/the-influence-of-particles-on-suspension-rheology/

Au, P. I., Siow, S. Y., Avadiar, L., Lee, E. M., & Leong, Y. K. (2014). Muscovite mica and koalin slurries: Yield stress–volume fraction and deflocculation point zeta potential comparison. *Powder Technology*, *262*, 124–130. doi:10.1016/j.powtec.2014.04.078

Balani, S. B., Ghaffar, S. H., Chougan, M., Pei, E., & Şahin, E. (2021). Processes and materials used for direct writing technologies: A review. *Results in Engineering*, *11*, 100257. doi:10.1016/j.rineng.2021.100257

Ball, P. (2001). Life's lessons in design. *Nature*, *409*, 413–416. doi:10.1038/35053198

Barnes, H. A. (1997). Thixotropy—a review. *Journal of Non-Newtonian Fluid Mechanics*, *70*, 1–33. doi:10.1016/s0377-0257(97)00004-9

Barthelat, F., & Espinosa, H. D. (2007). An experimental investigation of deformation and fracture of nacre-mother of pearl. *Experimental Mechanics*, *47*, 311–324. doi:10.1007/s11340-007-9040-1

Barthelat, F., Tang, H., Zavattieri, P. D., Li, C. M., & Espinosa, H. D. (2007). On the mechanics of mother-of-pearl: A key feature in the material hierarchical structure. *Journal of the Mechanics and Physics of Solids*, *55*, 306–337. doi:10.1016/j.jmps.2006.07.007

Bhushan, B. (2009). Biomimetics: Lessons from nature - an overview. *Philosophical Transactions of the Royal Society A*, *367*, 1445–1486. doi:10.1098/rsta.2009.0011

Bonderer, L. J., Studart, A. R., & Gauckler, L. J. (2008). Bioinspired design and assembly of platelet reinforced polymer films. *Science*, *319*, 1069–1073. doi:10.1126/science.1148726

Bonderer, L. J., Studart, A. R., Woltersdorf, J., Pippel, E., & Gauckler, L. J. (2009). Strong and ductile platelet-reinforced polymer films inspired by nature: Microstructure and mechanical properties. *Journal of Materials Research*, *24*, 2741–2754. doi:10.1557/jmr.2009.0340

Borges, J., & Mano, J. F. (2014). Molecular interactions driving the layer-by-layer assembly of multilayers. *Chemical Reviews*, *114*, 8883–8942. doi:10.1021/cr400531v

Bouville, F., Maire, E., Meille, S., Moortèle, B. V. D., Stevenson, A. J., & Deville, S. (2014). Strong, tough and stiff bioinspired ceramics from brittle constituents. *Nature Materials*, *13*, 508–514. doi:10.1038/nmat3915

Breuer, S. (2012). The chemistry of pottery. *Education in chEmiStry*, *49*(4), 17.

Cartwright, J. H., Checa, A. G., Escribano, B., & Sainz-Díaz, C. I. (2009). Spiral and target patterns in bivalve nacre manifest a natural excitable medium from layer growth of a biological liquid crystal. *Proceedings of the National Academy of Sciences of the United States of America*, *106*, 10499–10504. doi:10.1073/pnas.0900867106

Chen, G., Liang, X., Zhang, P., Lin, S., Cai, C., Yu, Z., & Liu, J. (2022). Bioinspired 3d printing of functional materials by harnessing enzyme-induced biomineralization. *Advanced Functional Materials*, *32*, 2113262. doi:10.1002/adfm.202113262

Chen, R., an Wang, C., Huang, Y., & Le, H. (2008). An efficient biomimetic process for fabrication of artificial nacre with ordered-nanostructure. *Materials Science and Engineering: C*, *2*, 218–222. doi:10.1016/j.msec.2006.12.008

Cheng, D. C. (1987). Thixotropy. *International Journal of Cosmetic Science*, *9*, 151–191. doi:10.1111/J.1467-2494.1987.TB00472.X

Corni, I., Harvey, T. J., Wharton, J. A., Stokes, K. R., Walsh, F. C., & Wood, R. J. (2012). A review of experimental techniques to produce a nacre-like structure. *Bioinspiration & Biomimetics*, *7*, 031001. doi:10.1088/1748-3182/7/3/031001

Currey, J. D. (1977). Mechanical properties of mother of pearl in tension. *Proceedings of the Royal Society of London B*, *196*, 443–463. doi:10.1098/rspb.1977.0050

Currey, J. D., & Taylor, J. D. (1974). The mechanical behaviour of some molluscan hard tissues. *Journal of Zoology*, *173*, 395–406. doi:10.1111/j.1469-7998.1974.TB04122.x

Davis, K. J., Dove, P. M., & Yoreo, J. J. D. (2000). The role of mg2+ as an impurity in calcite growth. *Science*, *290*, 1134–1137. doi:10.1126/science.290.5494.1134

Decher, G., Hong, J. D., & Schmitt, J. (1992). Buildup of ultrathin multilayer films by a self-assembly process: Iii. consecutively alternating adsorption of anionic and cationic polyelectrolytes on charged surfaces. *Thin Solid Films*, *210-211*, 831–835. doi:10.1016/0040-6090(92)90417-a

DeJong, J. T., Fritzges, M. B., & Nüsslein, K. (2006). Microbially induced cementation to control sand response to undrained shear. *Journal of Geotechnical and Geoenvironmental Engineering*, *132*, 1381–1392. doi:10.1061/(asce)1090-0241(2006)132:11(1381)

DeJong, J. T., Mortensen, B. M., Martinez, B. C., & Nelson, D. C. (2010). Bio-mediated soil improvement. *Ecological Engineering*, *36*, 197–210. doi:10.1016/j.ecoleng.2008.12.029

del-Mazo-Barbara, L., & Ginebra, M. P. (2021). Rheological characterisation of ceramic inks for 3d direct ink writing: A review. *Journal of the European Ceramic Society*, *41*, 18–33. doi:10.1016/j.jeurceramsoc.2021.08.031

Deville, S. (2008). Freeze-casting of porous ceramics: A review of current achievements and issues. *Advanced Engineering Materials*, *10*, 155–169. doi:10.1002/adem.200700270

Deville, S., Saiz, E., Nalla, R. K., & Tomsia, A. P. (2006). Freezing as a path to build complex composites. *Science*, *311*, 515–518. doi:10.1126/science.1120937

Du, G., Mao, A., Yu, J., Hou, J., Zhao, N., Han, J., … Bai, H. (2019). Nacre-mimetic composite with intrinsic self-healing and shape-programming capability. *Nature Communications*, *10*, 1–8. doi:10.1038/s41467-019-08643-x

Dullaert, K., & Mewis, J. (2006). A structural kinetics model for thixotropy. *Journal of Non-Newtonian Fluid Mechanics*, *139*, 21–30. doi:10.1016/j.jnnfm.2006.06.002

Dutto, A., Tervoort, E., Prakash, N., & Studart, A. R. (2025). Microbially controlled colloidal shaping of advanced ceramics. *Journal of the European Ceramic Society*, *45*, 116870. doi:10.1016/j.jeurceramsoc.2024.116870

Ekiz, O. O., Dericioglu, A. F., & Kakisawa, H. (2009). An efficient hybrid conventional method to fabricate nacre-like bulk nano-laminar composites. *Materials Science and Engineering: C*, *29*, 2050–2054. doi:10.1016/j.msec.2009.04.001

Espinal-Ruiz, M., Parada-Alfonso, F., Restrepo-Sánchez, L. P., Narváez-Cuenca, C. E., & McClements, D. J. (2014). Impact of dietary fibers [methyl cellulose, chitosan, and pectin] on digestion of lipids under simulated gastrointestinal conditions. *Food & Function*, *5*, 3083–3095. doi:10.1039/c4fo00615a

Espinosa, H. D., Rim, J. E., Barthelat, F., & Buehler, M. J. (2009). Merger of structure and material in nacre and bone – perspectives on de novo biomimetic materials. *Progress in Materials Science*, *54*, 1059–1100. doi:10.1016/j.pmatsci.2009.05.001

Evans, A. G., Suo, Z., Wang, R. Z., Aksay, I. A., He, M. Y., & Hutchinson, J. W. (2001). Model for the robust mechanical behavior of nacre. *Journal of Materials Research*, *16*, 2475–2482. doi:10.1557/jmr.2001.0339

Feilden, E., Blanca, E. G. T., Giuliani, F., Saiz, E., & Vandeperre, L. (2016). Robocasting of structural ceramic parts with hydrogel inks. *Journal of the European Ceramic Society*, *36*, 2525–2533. doi:10.1016/j.jeurceramsoc.2016.03.001

Feilden, E., Ferraro, C., Zhang, Q., García-Tuñón, E., D'Elia, E., Giuliani, F., … Saiz, E. (2017). 3d printing bioinspired ceramic composites. *Scientific Reports*, *7*, 1–9. doi:10.1038/s41598-017-14236-9

Ferrand, H. L., Bouville, F., Niebel, T. P., & Studart, A. R. (2015). Magnetically assisted slip casting of bioinspired heterogeneous composites. *Nature Materials*, *14*, 1172–1179. doi:10.1038/nmat4419

Franks, G. V., Tallon, C., Studart, A. R., Sesso, M. L., & Leo, S. (2017). Colloidal processing: Enabling complex shaped ceramics with unique multiscale structures. *Volume 100, Issue 2, Pages 458 - 490*, *100*, 458–490. doi:10.1111/jace.14705

Gao, H. L., Chen, S. M., Mao, L. B., Song, Z. Q., Yao, H. B., Cölfen, H., … Yu, S. H. (2017). Mass production of bulk artificial nacre with excellent mechanical properties. *Nature Communications*, *8*, 287. doi:10.1038/s41467-017-00392-z

Geyer, R., Jambeck, J. R., & Law, K. L. (2017). Production, use, and fate of all plastics ever made. *Science Advances*, *3*. doi:10.1126/sciadv.1700782

Ghosh, T., Bhaduri, S., Montemagno, C., & Kumar, A. (2019). Sporosarcina pasteurii can form nanoscale calcium carbonate crystals on cell surface. *PLoS ONE*, *14*, e0210339. doi:10.1371/journal.pone.0210339

Gilbert, C., & Ellis, T. (2019). Biological engineered living materials: Growing functional materials with genetically programmable properties. *ACS Synthetic Biology*, *8*, 1–15. doi:10.1021/acssynbio.8b00423

Glavinchevski, B., & Piggott, M. (1973). Steel disc reinforced polycarbonate. *Journal of Materials Science*, *8*, 1373–1382. doi:10.1007/BF00551660

Grossman, M., Bouville, F., Erni, F., Masania, K., Libanori, R., & Studart, A. R. (2017). Mineral nano-interconnectivity stiffens and toughens nacre-like composite materials. *Advanced Materials*, *29*, 1605039. doi:10.1002/adma.201605039

Grossman, M., Bouville, F., Masania, K., & Studart, A. R. (2018). Quantifying the role of mineral bridges on the fracture resistance of nacre-like composites. *Proceedings of the National Academy of Sciences of the United States of America*, *115*, 12698–12703. doi:10.1073/pnas.1805094115

Grossman, M., Pivovarov, D., Bouville, F., Dransfeld, C., Masania, K., & Studart, A. R. (2019). Hierarchical toughening of nacre-like composites. *Advanced Functional Materials*, *29*, 1806800. doi:10.1002/adfm.201806800

Gu, G. X., Libonati, F., Wettermark, S. D., & Buehler, M. J. (2017). Printing nature: Unraveling the role of nacre's mineral bridges. *Journal of the Mechanical Behavior of Biomedical Materials*, *76*, 135–144. doi:10.1016/j.jmbbm.2017.05.007

Guner, S. N. G., & Dericioglu, A. F. (2016). Nacre-mimetic epoxy matrix composites reinforced by two-dimensional glass reinforcements. *RSC Advances*, *6*, 33184–33196. doi:10.1039/c5ra25049h

Hausmann, M. K., Rühs, P. A., Siqueira, G., Läuger, J., Libanori, R., Zimmermann, T., & Studart, A. R. (2018). Dynamics of cellulose nanocrystal alignment during 3d printing. *ACS Nano*, *12*, 6926–6937. doi:10.1021/acsnano.8b02366

Herschel, W. H., & Bulkley, R. (1926). Konsistenzmessungen von gummi-benzollösungen. *Kolloid-Zeitschrift*, *39*, 291–300. doi:10.1007/BF01432034

Hertwich, E. G. (2021). Increased carbon footprint of materials production driven by rise in investments. *Nature Geoscience*, *14*, 151–155. doi:10.1038/s41561-021-00690-8

Hirsch, M., Lucherini, L., Zhao, R., Saracho, A. C., & Amstad, E. (2023). 3d printing of living structural biocomposites. *Materials Today*, *62*, 21–32. doi:10.1016/j.mattod.2023.02.001

Huang, Z., Li, H., Pan, Z., Wei, Q., Chao, Y. J., & Li, X. (2011). Uncovering high-strain rate protection mechanism in nacre. *Scientific Reports*, *1*, 1–5. doi:10.1038/srep00148

Hurd, A. J., Kelley, R. L., Eggert, R. G., & Lee, M. H. (2012). Energy-critical elements for sustainable development. *MRS Bulletin*, *37*, 405–410. doi:10.1557/mrs.2012.54

Iler, R. K. (1966). Multilayers of colloidal particles. *Journal of Colloid and Interface Science*, *21*, 569–594. doi:10.1016/0095-8522(66)90018-3

IPCC. (2022). *Climate change 2022: Mitigation of climate change. contribution of working group iii to the sixth assessment report of the intergovernmental panel on climate change* (P. Shukla, J. Skea, R. Slade, A. A. Khourdajie, R. van Diemen, D. McCollum, ... J. Malley, Eds.). doi:10.1017/9781009157926

Jackson, A. P., Vincent, J. F. V., & Turner, R. (1988). The mechanical design of nacre. *Proceedings of the Royal Society of London B*, *234*, 415–440. doi:10.1098/rspb.1988.0056

Jang, D., Meza, L. R., Greer, F., & Greer, J. R. (2013). Fabrication and deformation of three-dimensional hollow ceramic nanostructures. *Nature Materials*, *12*, 893–898. doi:10.1038/nmat3738

Jonkers, H. M., Thijssen, A., Muyzer, G., Copuroglu, O., & Schlangen, E. (2010). Application of bacteria as self-healing agent for the development of sustainable concrete. *Ecological Engineering*, *36*, 230–235. doi:10.1016/j.ecoleng.2008.12.036

Kalesaran, O. J., & Lumenta, C. (2021). Analisis scanning electron microscopy pada nacre sinanodonta (anodonta) woodiana (lea, 1834). *Journal of Aquaculture and Fish Health*, *10*, 75–84. doi:10.20473/jafh.v10i1.19567

Kokkinis, D., Schaffner, M., & Studart, A. R. (2015). Multimaterial magnetically assisted 3d printing of composite materials. *Nature Communications*, *6*, 1–10. doi:10.1038/ncomms9643

Krüger, K. (2022). *Shaping living matter: Direct ink writing of cellulose producing bacteria.* [Master's Thesis, Delft University of Technology]. Retrieved from http://resolver.tudelft.nl/uuid:2b43f447-2bbd-4168-836e-4a95847e0d5b

Kumari, N., & Mohan, C. (2021). Basics of clay minerals and their characteristic properties. *Clay and Clay Minerals*. doi:10.5772/intechopen.97672

Launey, M. E., Munch, E., Alsem, D. H., Barth, H. B., Saiz, E., Tomsia, A. P., & Ritchie, R. O. (2009). Designing highly toughened hybrid composites through nature-inspired hierarchical complexity. *Acta Materialia*, *57*, 2919–2932. doi:10.1016/j.actamat.2009.03.003

Lewis, J. A. (2000). Colloidal processing of ceramics. *Journal of the American Ceramic Society*, *83*, 2341–2359. doi:10.1111/j.1151-2916.2000.tb01560.x

Lewis, J. A. (2006). Direct ink writing of 3d functional materials. *Advanced Functional Materials*, *16*, 2193–2204. doi:10.1002/adfm.200600434

Lewis, J. A., Smay, J. E., Stuecker, J., & Cesarano, J. (2006). Direct ink writing of three-dimensional ceramic structures. *Journal of the American Ceramic Society*, *89*, 3599–3609. doi:10.1111/j.1551-2916.2006.01382.x

Li, X., Xu, Z. H., & Wang, R. (2006). In situ observation of nanograin rotation and deformation in nacre. *Nano Letters*, *6*, 2301–2304. doi:10.1021/nl061775u

Libonati, F., & Buehler, M. J. (2017). Advanced structural materials by bioinspiration. *Advanced Engineering Materials*, *19*, 1600787. doi:10.1002/adem.201600787

M'Barki, A., Bocquet, L., & Stevenson, A. (2017). Linking rheology and printability for dense and strong ceramics by direct ink writing. *Scientific Reports*, *7*, 6017. doi:10.1038/s41598-017-06115-0

Martin, J. J., Fiore, B. E., & Erb, R. M. (2015). Designing bioinspired composite reinforcement architectures via 3d magnetic printing. *Nature Communications*, *6*, 1–7. doi:10.1038/ncomms9641

Mautner, A., Lucenius, J., Österberg, M., & Bismarck, A. (2017). Multi-layer nanopaper based composites. *Cellulose*, *24*, 1759–1773. doi:10.1007/s10570-017-1220-2

Merck KGaA. (2019). Banish the Microplastics. Brochure. Retrieved from https://www.merckgroup.com/content/dam/web/digital-brochures/non-images/global/Merck_BtM_brochure.pdf

Meyers, M. A., McKittrick, J., & Chen, P. Y. (2013). Structural biological materials: Critical mechanics-materials connections. *Science*, *339*, 773–779. doi:10.1126/science.1220854

Mezi, D., Ausias, G., Grohens, Y., & Férec, J. (2019). Numerical simulation and modeling of the die swell for fiber suspension flows. *Journal of Non-Newtonian Fluid Mechanics*, *274*, 104205. doi:10.1016/j.jnnfm.2019.104205

Mortensen, B. M., Haber, M. J., Dejong, J. T., Caslake, L. F., & Nelson, D. C. (2011). Effects of environmental factors on microbial induced calcium carbonate precipitation. *Journal of Applied Microbiology*, *111*, 338–349. doi:10.1111/j.1365-2672.2011.05065.x

Munch, E., Launey, M. E., Alsem, D. H., Saiz, E., Tomsia, A. P., & Ritchie, R. O. (2008). Tough, bio-inspired hybrid materials. *Science*, *322*, 1516–1520. doi:10.1126/science.1164865

Myśliwiec, D., Chylińska, M., Szymańska-Chargot, M., Chibowski, S., & Zdunek, A. (2016). Revision of adsorption models of xyloglucan on microcrystalline cellulose. *Cellulose*, *23*, 2819–2829. doi:10.1007/s10570-016-0995-x

Naglieri, V., Gludovatz, B., Tomsia, A. P., & Ritchie, R. O. (2015). Developing strength and toughness in bioinspired silicon carbide hybrid materials containing a compliant phase. *Acta Materialia*, *98*, 141–151. doi:10.1016/j.actamat.2015.07.022

Nettersheim, I. H. M. S. (2022). *The additive manufacturing of biomineralized bacterial cellulose*. [Unpublished Master's Thesis, Delft University of Technology].

Novak, S., & Kalin, M. (2004). The effect of ph on the wear of water-lubricated alumina and zirconia ceramics. *Tribology Letters*, *17*, 727–732. doi:10.1007/s11249-004-8080-2

Oaki, Y., & Imai, H. (2005). The hierarchical architecture of nacre and its mimetic material. *Angewandte Chemie International Edition*, *44*, 6571–6575. doi:10.1002/anie.200500338

Okwadha, G. D., & Li, J. (2010). Optimum conditions for microbial carbonate precipitation. *Chemosphere*, *81*, 1143–1148. doi:10.1016/j.chemosphere.2010.09.066

Peker, S. M., & Helvaci, S. S. (2008). *Solid-liquid two phase flow* (1st ed.). Elsevier.

Podsiadlo, P., Kaushik, A. K., Arruda, E. M., Waas, A. M., Shim, B. S., Xu, J., … Kotov, N. A. (2007). Ultrastrong and stiff layered polymer nanocomposites. *Science*, *318*, 80–83. doi:10.1126/science.1143176

Rahmanian, N., Naderi, S., Supuk, E., Abbas, R., & Hassanpour, A. (2015). Urea finishing process: Prilling versus granulation. *Procedia Engineering*, *102*, 174–181. doi:10.1016/j.proeng.2015.01.122

Rissman, J., Bataille, C., Masanet, E., Aden, N., Morrow, W. R., Zhou, N., … Helseth, J. (2020). Technologies and policies to decarbonize global industry: Review and assessment of mitigation drivers through 2070. *Applied Energy*, *266*, 114848. doi:10.1016/j.apenergy.2020.114848

Ritchie, H., Samborska, V., & Roser, M. (2023). Plastic pollution. *Our World in Data*. Retrieved from https://ourworldindata.org/plastic-pollution

Ritchie, R. O. (2011). The conflicts between strength and toughness. *Nature Materials*, *10*, 817–822. doi:10.1038/nmat3115

Rodrigo-Navarro, A., Sankaran, S., Dalby, M. J., del Campo, A., & Salmeron-Sanchez, M. (2021). Engineered living biomaterials. *Nature Reviews Materials*, *6*, 1175–1190. doi:10.1038/s41578-021-00350-8

Saracho, A. C., Haigh, S. K., Hata, T., Soga, K., Farsang, S., Redfern, S. A., & Marek, E. (2020). Characterisation of caco3 phases during strain-specific ureolytic precipitation. *Scientific Reports*, *10*, 1–12. doi:10.1038/s41598-020-66831-y

Sarikaya, M., & Aksay, I. A. (Eds.). (1995). *Biomimetics: Design and processing of materials*. American Institute of Physics.

Schmieden, D. (2019). *Imitating nature to produce nacre-inspired composite materials with bacteria*. [Doctoral Thesis, Delft University of Technology]. doi:10.4233/uuid:d165937b-4e6d-459d-acfb-5d45e46d4edf

Seifan, M., & Berenjian, A. (2018). Application of microbially induced calcium carbonate precipitation in designing bio self-healing concrete. *World Journal of Microbiology and Biotechnology*, *34*, 1–15. doi:10.1007/s11274-018-2552-2

Shao, G., Hanaor, D. A., Shen, X., & Gurlo, A. (2020). Freeze casting: From low-dimensional building blocks to aligned porous structures—a review of novel materials, methods, and applications. *Advanced Materials*, *32*, 1907176. doi:10.1002/adma.201907176

Siqueira, G., Kokkinis, D., Libanori, R., Hausmann, M. K., Gladman, A. S., Neels, A., … Studart, A. R. (2017). Cellulose nanocrystal inks for 3d printing of textured cellular architectures. *Advanced Functional Materials*, *27*, 1604619. doi:10.1002/adfm.201604619

Smay, J. E., Cesarano, J., & Lewis, J. A. (2002). Colloidal inks for directed assembly of 3-d periodic structures. *Langmuir*, *18*, 5429–5437. doi:10.1021/la0257135

Smith, B. L., Schäffer, T. E., Vlani, M., Thompson, J. B., Frederick, N. A., Klndt, J., … Hansma, P. K. (1999). Molecular mechanistic origin of the toughness of natural adhesives, fibres and composites. *Nature*, *399*, 761–763. doi:10.1038/21607

Spiesz, E. M., Schmieden, D. T., Grande, A. M., Liang, K., Schwiedrzik, J., Natalio, F., … Meyer, A. S. (2019). Bacterially produced, nacre-inspired composite materials. *Small*, *15*. doi:10.1002/smll.201805312

Stocks-Fischer, S., Galinat, J. K., & Bang, S. S. (1999). Microbiological precipitation of caco3. *Soil Biology and Biochemistry*, *31*, 1563–1571. doi:10.1016/s0038-0717(99)00082-6

Studart, A. R. (2016). Additive manufacturing of biologically-inspired materials. *Chemical Society Reviews*, *45*, 359–376. doi:10.1039/c5cs00836k

Tang, C. S., yang Yin, L., jun Jiang, N., Zhu, C., Zeng, H., Li, H., & Shi, B. (2020). Factors affecting the performance of microbial-induced carbonate precipitation (micp) treated soil: A review. *Environmental Earth Sciences*, *79*, 1–23. doi:10.1007/s12665-020-8840-9

Tang, Z., Kotov, N. A., Magonov, S., & Ozturk, B. (2003). Nanostructured artificial nacre. *Nature Materials*, *2*, 413–418. doi:10.1038/nmat906

Tao, Z., Yuan, H., Liu, M., Liu, Q., Zhang, S., Liu, H., … Wang, T. (2023). Yeast extract: Characteristics, production, applications and future perspectives. *J. Microbiol. Biotechnol. 33*, 151–166. doi:10.4014/jmb.2207.07057

Tsortos, A., & Nancollas, G. H. (2002). The role of polycarboxylic acids in calcium phosphate mineralization. *Journal of Colloid and Interface Science*, *250*, 159–167. doi:10.1006/jcis.2002.8323

Walther, A., Bjurhager, I., Malho, J. M., Pere, J., Ruokolainen, J., Berglund, L. A., & Ikkala, O. (2010a). Large-area, lightweight and thick biomimetic composites with superior material properties via fast, economic, and green pathways. *Nano Letters*, *10*, 2742–2748. doi:10.1021/nl1003224

Walther, A., Bjurhager, I., Malho, J.-M., Ruokolainen, J., Berglund, L., Ikkala, O., … Berglund, L. (2010b). Supramolecular control of stiffness and strength in lightweight high-performance nacre-mimetic paper with fire-shielding properties. *Angewandte Chemie International Edition*, *49*, 6448–6453. doi:10.1002/anie.201001577

Wang, C.-a., Huang, Y., Zan, Q., Guo, H., & Cai, S. (2000). Biomimetic structure design — a possible approach to change the brittleness of ceramics in nature. *Materials Science and Engineering: C*, *11*, 9–12. doi:10.1016/S0928-4931(00)00133-8

Wang, J., Cheng, Q., & Tang, Z. (2012). Layered nanocomposites inspired by the structure and mechanical properties of nacre. *Chemical Society Reviews*, *41*, 1111–1129. doi:10.1039/c1cs15106a

Wang, R. Z., Suo, Z., Evans, A. G., Yao, N., & Aksay, I. A. (2001). Deformation mechanisms in nacre. *Journal of Materials Research*, *16*, 2485–2493. doi:10.1557/jmr.2001.0340

Wang, R., & Gupta, H. S. (2011). Deformation and fracture mechanisms of bone and nacre. *Annual Review of Materials Research*, *41*, 41–73. doi:10.1146/annurev-matsci-062910-095806

Wang, W., Bo, S., Li, S., & Qin, W. (1991). Determination of the mark-houwink equation for chitosans with different degrees of deacetylation. *International Journal of Biological Macromolecules*, *13*, 281–285. doi:10.1016/0141-8130(91)90027-r

Wegst, U. G., Bai, H., Saiz, E., Tomsia, A. P., & Ritchie, R. O. (2015). Bioinspired structural materials. *Nature Materials*, *14*, 23–36. doi:10.1038/nmat4089

Wilms, P., Wieringa, J., Blijdenstein, T., van Malssen, K., & Kohlus, R. (2021). Quantification of shear viscosity and wall slip velocity of highly concentrated suspensions with non-newtonian matrices in pressure driven flows. *Rheologica Acta*, *60*, 423–437. doi:10.1007/s00397-021-01281-5

Xie, L., Wang, X. X., & Li, J. (2010). The sem and tem study on the laminated structure of individual aragonitic nacre tablet in freshwater bivalve h. cumingii lea shell. *Journal of Structural Biology*, *169*, 89–94. doi:10.1016/J.JSB.2009.09.002

Xin, A., Su, Y., Feng, S., Yan, M., Yu, K., Feng, Z., … Sun, L. (2021). Growing living composites with ordered microstructures and exceptional mechanical properties. *Advanced Materials*, *33*, 2006946. doi:10.1002/adma.202006946

Yang, X., Sun, Z., Wang, D., & Forsling, W. (2007). Surface acid–base properties and hydration/dehydration mechanisms of aluminum (hydr)oxides. *Journal of Colloid and Interface Science*, *308*, 395–404. doi:10.1016/J.JCIS.2006.12.023

Yang, Y., Song, X., Li, X., Chen, Z., Zhou, C., Zhou, Q., … Zhou, C. (2018). Recent progress in biomimetic additive manufacturing technology: From materials to functional structures. *Advanced Materials*, *30*, 1706539. doi:10.1002/adma.201706539

Yu, K., Spiesz, E. M., Balasubramanian, S., Schmieden, D. T., Meyer, A. S., & Aubin-Tam, M. E. (2021). Scalable bacterial production of moldable and recyclable biomineralized cellulose with tunable mechanical properties. *Cell Reports Physical Science*, *2*, 100464. doi:10.1016/j.xcrp.2021.100464

Zelenková, G., & Slovák, V. (2022). Decomposition of ammonium salts by quantitative tg-ms. *Journal of Thermal Analysis and Calorimetry*, *147*, 15059–15068. doi:10.1007/S10973-022-11747-0

Zhang, N., Li, S., Xiong, L., Hong, Y., & Chen, Y. (2015). Cellulose-hemicellulose interaction in wood secondary cell-wall. *Modelling and Simulation in Materials Science and Engineering*, *23*, 085010. doi:10.1088/0965-0393/23/8/085010

Zhao, C., Zhang, P., Zhou, J., Qi, S., Yamauchi, Y., Shi, R., … Liu, M. (2020). Layered nanocomposites by shear-flow-induced alignment of nanosheets. *Nature*, *580*, 210–215. doi:10.1038/s41586-020-2161-8

Zhu, C., & Smay, J. E. (2011). Thixotropic rheology of concentrated alumina colloidal gels for solid freeform fabrication. *Journal of Rheology*, *55*, 655–672. doi:10.1122/1.3573828

A

Project & resource management

This appendix provides a detailed overview of the project and resource management aspects of the thesis, including a work breakdown structure, an initial Gantt chart depicting the project timeline, a reflection on deviations from the projected schedule, and the data management practices.

A.1. Work breakdown structure

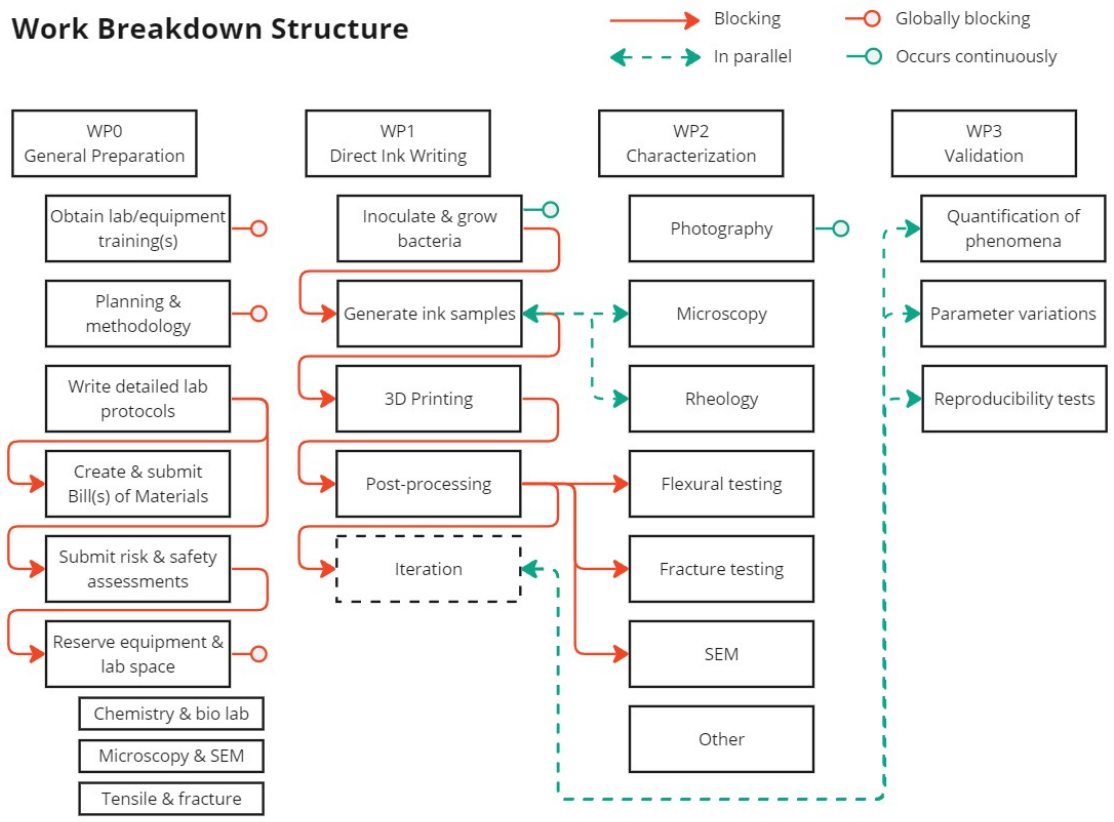

Figure A.1: Work breakdown structure for the thesis project. Dependencies and parallel tasks are identified using orange and green arrows, respectively.

A.2. Gantt chart

Figure A.2: Initially projected timeline for thesis project. A total of 3 weeks of overhead is left.

A.3. Reflection on timeline execution

The true thesis timeline deviates somewhat from the timeline provided in fig. A.2. In particular, as discussed and agreed upon with the responsible supervisor, the literature review, research proposal, and midterm milestones were combined so that lab work could begin immediately, allowing a better balance between practical and office work. At first, holidays were included in 'working' time as stated in the 100% FTE timeline, but this proved problematic especially due to the interruption of continuity in experimental campaigns. Additional leaves spanning 3 weeks total were also not included in the initial planning. As a result, the exclusion of holidays from working time was discussed and agreed upon with the thesis supervisors. The resulting deadline shifts were approved by the study programme administration.

Crucially, mitigation strategies for certain unforeseen risks were not in place, including:

1. Difficulties in troubleshooting ink formulation after hitting a major roadblock,
2. Multiple occasions of extended unavailability (2+ weeks) of critical lab staff leading to non-trainability or non-usability of equipment,
3. Generally highly defective equipment, leading to learning curves on almost all measurement techniques with associated repetitions and delays,
4. Generally high unavailability of lab equipment, either due to malfunctions and/or extensively booked reservation systems (1+ month fully booked), being especially problematic for experiments where the time of start cannot be predicted until a few days in advance.

The consequences of these risks resulted in full use of the 3-week overhead in addition to the abandonment of three experimental campaigns, namely the assessment of self-healing properties, quantification of fracture toughness, and, most importantly, the iteration of the final ink so that biomineralisation could be observed. In summary, deadlines were shifted to include personal leaves but the project work was performed within the agreed working time despite difficulties.

A.4. Data management

The data collected in this project has been stored in a traceable manner using non-proprietary formats. Here, an overview is provided of the data storage methods and access. Further or unintentionally inaccessible data can be provided upon request.

Table A.1: Data storage locations and access. All data is submitted to project drive (U:/) upon thesis submission.

Type	Format	How collected	Purpose	Storage location	Users with access
Lab journal & notes	Handwritten, .pdf, Notion environment	Digitised, web-based	Report conditions and details of methodology	Physical notebook digitized	Author, mentor, and supervisor
Images and videos	.jpeg & .mp4	Phone camera and USB microscope	Documentation and assessment of printability	Laptop, backup on SURFdrive.	Author, mentor, and supervisor.
SEM images	.TIFF	SEM, DASML	Characterize material microstructure and bacterial content	Laptop, backup on SURFdrive.	Author, mentor, and supervisor
Rheology data	.txt	Rheometer	Characterization of ink	Laptop, backup on thesis SURFdrive.	Author, mentor, and supervisor.
Flexure data	.zs2 and .csv	Zwick 10kN	Characterization of mechanical properties.	Laptop, backup on SURFdrive.	Author, mentor, and supervisor.
Profile data	.csv	3D optical microscopy	Coupon geometry	Laptop, SURFdrive.	Author, mentor, supervisor.

Multiple backups of the data have been maintained. These can be found at the following locations.

- Personal storage
- SURFdrive
- Project (U:/) drive
- Viewer access to Notion workspace can be provided upon request

B

Literature search queries

This appendix describes the search queries used to find the main relevant literature for this thesis. The general process followed was to formulate and submit queries in Web of Science and Scopus, then identifying relevant articles and reviews and via abstracts, sorting by citation count. (Reference lists of) recent articles were scanned to find new or influential articles and to probe the level of understanding of the field at hand. In some instances, connectedpapers.com was used to find an initial overview of relevant literature, although this was found to not always include the most recent literature.

B.1. Background

B.1.1. Bio-inspired hierarchical materials

Concept

Bio-inspired Hierarchical Materials

Keywords

Keyword	Bio-inspired	Hierarchical	Materials
Synonyms	Biologically-inspired; Biomimetic; Bioinspired.	Multi-scale; Architectured; Composite.	Composites; Architectures.

Query

("bioinspired" OR "bio-inspired" OR "biologically-inspired" OR "biologically inspired" OR "biomimetic") AND ("hierarchical" OR "multi-scale" OR "architectured" OR "composite") AND ("materials" OR "composites" OR "architectures")

Results

Date	Database	Filter(s)	Amount
19/01/24	Web of Science		630,077
19/01/24	Web of Science	Review articles, 2019+	15,758

B.1.2. Nacre

Concept

Nacre

Query

"nacre"

Results

Date	Database	Filter(s)	Amount
19/01/24	Web of Science		8,709
19/01/24	Web of Science	Review articles	532
19/01/24	Web of Science	Review articles, 2019+	199

B.2. Related

Concept

Nacre-mimetic material

Keywords

Keyword	Nacre	Mimetic	Material
Synonyms		Inspired; Mimicking; Like	Composite; Architecture.

Query

"nacre" AND ("mimetic" OR "inspired" OR "mimicking" OR "like") AND ("material*" OR "composite*" OR "architecture*")

Results

Date	Database	Filter(s)	Amount
19/01/24	Web of Science		1,777
19/01/24	Web of Science	Review articles	92

B.3. Specific

B.3.1. Additive manufacturing of nacre-mimetic materials

Concept

Additive manufacturing of nacre-mimetic materials

Keywords

Keyword	Additive manufacturing	Nacre	Mimetic	Materials
Synonyms	3D(-)Printing; Robocasting; Direct ink writing.		Inspired; Mimicking; Like	Composite; Architecture.

Query

("additive manufacturing" OR "3D printing" OR "robocasting" OR "direct ink writing") AND "nacre" AND ("mimetic" OR "inspired" OR "mimic*" OR "like") AND ("material*" OR "composite*" OR "architecture")

Results

Date	Database	Filter(s)	Amount
19/01/24	Web of Science		17

B.3.2. Microbially-induced calcite precipitation

Concept

Microbially-induced calcite precipitation

Keywords

Keyword	Microbially	Induced	Calcite	Precipitation
Synonyms	Microbe; Microbiologically.	-	Calcium carbonate.	-

Query

("microb*" AND "induced" AND (calcite OR "calcium carbonate") AND "precipitation") OR "MICP"

Results

Date	Database	Filter(s)	Amount
19/01/24	Scopus		4,054
20/01/24	Scopus	Review articles	168

C

Practical details and remarks

C.1. Laboratory protocols

C.1.1. Preparation of *S. pasteurii* Growth Medium

Note: Nickel(II) chloride is acutely toxic, causes skin irritation, may cause cancer when inhaled, and is highly toxic to aquatic life with long-lasting effects. Handle in a fume hood using nitrile rubber gloves and eye protection. Dispose of gloves immediately after handling and equip new ones. Avoid dust formation - carefully weigh powder. Use the balance already placed inside the fume hood in the biolab, do not move any balances in and out of the fume hoods. Clean contaminated areas thoroughly: remove bulk powder mechanically into appropriate disposal container, pre-rinse remainder with running water, wash with mild detergent, rinse thoroughly, dry using clean paper towel. Label solutions and store with correct ADR class (ADR 6). Label and discard disposal container at solid chemical storage.

Note: Sodium hydroxide can cause severe skin burns and eye damage and can be corrosive to metals. Use nitrile rubber gloves and wear eye protection when handling. Handle and open container with care, avoid dust formation. Clear contaminated areas thoroughly: remove bulk powder mechanically into appropriate disposal container, neutralize remainder using excess weak acid solution (e.g. vinegar) - avoiding splashing, pre-rinse remainder with running water, wash with mild detergent, rinse thoroughly, dry using clean paper towel. Label and discard disposal container at solid chemical storage. Never add water to solid sodium hydroxide. The reaction is highly exothermic, and can lead to violent boiling of the solution and potential burns. Instead, add the solid slowly to sufficient water.

1. Prepare 10 ml of 0.1 $\mathrm{mol\,l^{-1}}$ nickel(II) chloride solution in demineralized water.
2. Prepare 100 ml of SP medium by combining 20 $\mathrm{g\,l^{-1}}$ yeast extract, 10 $\mathrm{g\,l^{-1}}$ ammonium chloride, and 100 $\mathrm{\mu l\,l^{-1}}$ of 0.1 $\mathrm{mol\,l^{-1}}$ nickel(II) chloride solution.
3. Adjust the pH to 8.5 with sodium hydroxide pellets using electrodes.
4. Autoclave to sterilize.

Note: To limit exposure and contamination of the working space, the SP medium should be prepared and autoclaved in the (Erlenmeyer) flask used for fermentation, preventing additional transfer steps. To prevent contamination of the autoclave and spillage in subsequent steps, the Erlenmeyer flask is sealed with a cellulose stopper (allowing equalisation of pressure) covered with aluminium foil.

Note: The nickel(II) chloride concentration in the SP medium is approximately 1.3 $\mathrm{\mu g\,l^{-1}}$ which is lower than the toxicity exposure values indicated on the MSDS. Unused 0.1 $\mathrm{mol\,l^{-1}}$ solution is disposed of as category 2 alkaline waste.

C.1.2. Preparation of *S. pasteurii* Glycerol Stock

S. pasteurii can be stored for long periods at −80 °C in a glycerol stock. To make more of this stock the following procedure can be used:

1. Prepare 100 ml of *S. pasteurii* growth medium (see appendix C.1.1)
2. Add 20 µl of stored *S. pasteurii* stock
3. Incubate for 48 h at 28 °C and 125 RPM
4. Centrifuge for 5 min at 6000 rcf in 50 ml tubes
5. Carefull decant supernatant, dispose of as ML-I waste.
6. Resuspend each precipitate in 5 ml of fresh SP medium, add 5 ml of 80 vol% sterile glycerol in demineralised water solution
7. Store glycerol stock at −80 °C in 1.5 ml cryo-tubes

C.1.3. Preparation of phyllosilicate/powdered chitosan ink

Note: Ammonium chloride is irritating to the skin and eyes and harmful when ingested. Use nitrile rubber gloves when handling and avoid dust formation.

Note: Do not autoclave or heat ammonium or urea solutions, including the ink at any stage, without appropriate safety measures; hazardous ammonia gases are formed. To sterilise use vacuum filtration. Note that ammonium chloride is a stable salt and does not produce ammonia gas upon heating in solution. However, in dehydrated form, upon heating it decomposes into ammonia and hydrogen chloride gas. Boiling of ammonium chloride solutions should therefore be carried out in a fume hood in the event that full evaporation of the solvent occurs by accident.

Note: Fine crystalline silica particles of 'respirable size' (<10 µm) can cause eye and respiratory irritation. Repeated inhalation can lead to silicosis, increasing the risk of lung cancer. Verify the particle size before handling. Handle preferrably in a fume hood using nitrile rubber gloves, avoid dust formation.

Note: Acetic acid solutions of high concentrations (>25%) cause severe skin burns and eye damage. Handle using gloves and eye protection. Label using ADR 8. Large amounts that cannot be practically or safely diluted should be disposed as category III organic waste.

The following procedure results in approximately 50 g of ink (~35 ml):

1. Perform steps 1-3 of appendix C.1.2 in advance.
2. In a plastic container, prepare a 25 ml solution containing 1 wt% acetic acid and 3 wt% chitosan. Homogenize using a stirring rod or spatula.
3. Add 20 g phyllosilicate platelets, resulting in 40 wt% in the final ink.
4. Add 1.5 ml of 8× biomineralization (BM) medium consisting of 80 $g l^{-1}$ tryptone/peptone, 40 $g l^{-1}$ yeast extract, and 80 $g l^{-1}$ ammonium chloride.
5. Homogenise in a planetary speed mixer at 3500 RPM for 5 min.
6. Prepare a 50 ml solution containing 22.05 g of calcium chloride dihydrate and 30.0 g of urea. Adding 1 ml of this solution to the ink (assuming 30 ml of ink) results in calcium chloride dihydrate and urea concentrations of 100 $mmol l^{-1}$ and 333 $mmol l^{-1}$, respectively.
7. Add 1 ml of the salt/urea solution into the (now gelled) BM solution.
8. Homogenise gel in a planetary speed mixer at 3500 RPM for 5 min.
9. Perform steps 4 and 5 of appendix C.1.2 on the inoculate prepared in step 1. The amount of supernatant decanted can be varied to modulate the amount of bacteria added to the ink.
10. Resuspend the precipitate in the remaining supernatant by gently shaking the container. Add 1 ml of the suspension to the ink and homogenise *gently* (e.g. by hand using a stirring rod or spatula)
11. Distribute across 12 ml syringes.
12. With a luer cap on each syringe, centrifuge the inks for 25 s at 1000 rcf to remove air bubbles and push the ink towards the bottom.
13. Using a long needle to bypass the plunger seal, press the plunger down against the ink.

14. Replace the syringe cap with the desired nozzle (standard is 18 gauge, green color). Purge the nozzle with ink. The ink is now ready to be printed.

C.2. Ink drying rate

During preparation, inks were observed to dry on the sides of the beaker quickly. To obtain an quantitative indication of how quickly the inks can dry in ambient conditions, the initial ink was left in its mixing beaker, with the lid open, on a scale and the change in mass measured. The result is shown in fig. C.1.

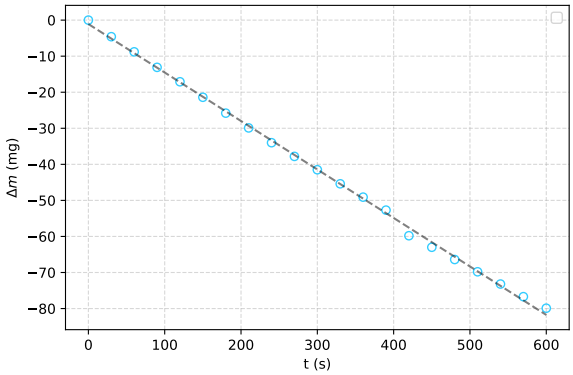

Figure C.1: Drying rate shown by open container mass change over time. Normalizing to container diameter yields a drying rate of $0.6\,\mathrm{mg\,cm^{-2}\,min^{-1}}$ (~2 wt% water per hour for a batch).

During the first rheological measurements, upon sample removal samples were noted to be very dry near the circumference and wet in the middle despite the relatively slow drying rates measured for the open beaker. Since in parallel plate rheology the outer ring of material has the largest effect on the measurement (since the shear stress is highest there), the effect is believed to be significant. To limit this, for all subsequent measurements silicone oil was dripped over the circumference of the top plate and allowed to flow down, sealing the sample. A constant displacement amplitude time sweep was performed on two equal samples to measure the difference, shown in fig. C.2.

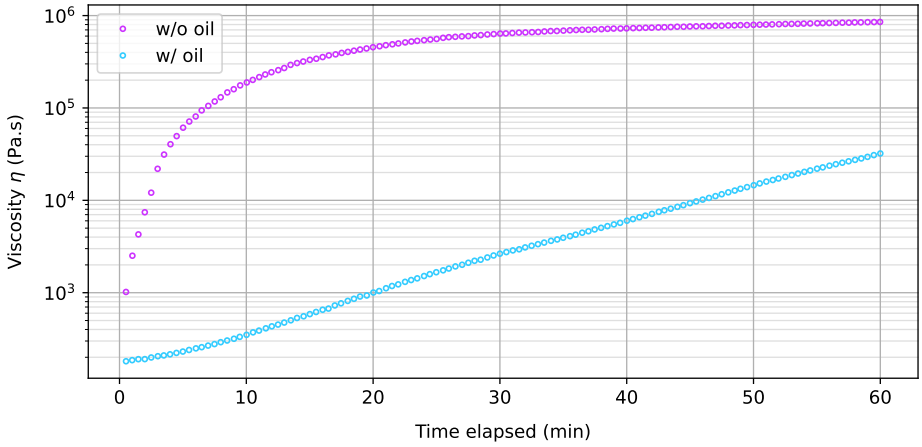

Figure C.2: Constant strain time evolution of initial ink sample showing large difference between bare sample and sample coated with silicone oil. $|\epsilon| = 0.1\%$, gap size 0.5 mm, no normal force zeroing.

In addition, to see how this influences perceived yield stress and stiffness, oscillatory stress amplitude sweeps were conducted, shown in fig. C.3.

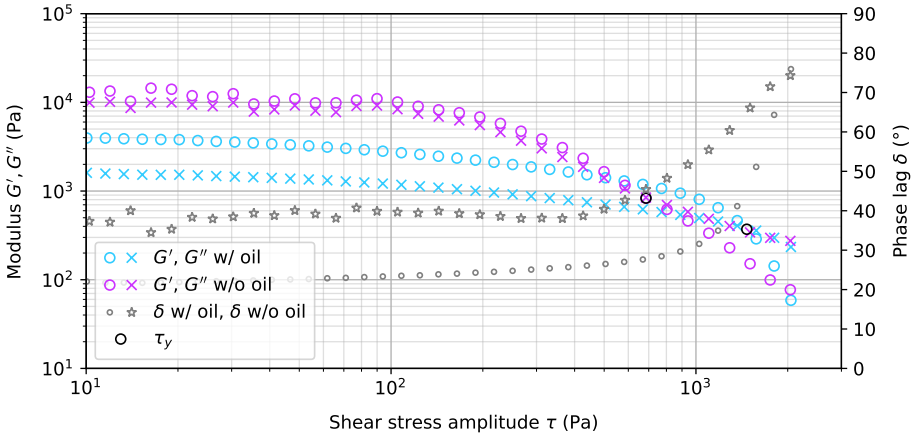

Figure C.3: Oscillatory stress amplitude sweeps for initial ink samples with and without silicone oil coating. Note the increase in perceived yield stress and decrease in stiffness.

C.3. Preparation of 1 mm length nozzles

Since 1" (25.4 mm) length nozzles were not available for the given diameter (0.51 mm), 1.5" (38.1 mm) nozzles were cut at about 1.2" with pliers and manually sanded with P400 sandpaper down to 1", followed by smoothing with P1000 paper and deburring under USB microscope with the sharp edge of a hypodermic needle tip. To verify that the cross-section remains the same, images were taken with the USB microscope, shown in fig. C.4.

(a) Tip of untrimmed 1.5" nozzle

(b) Tip of trimmed 1" nozzle.

Figure C.4: Comparison of untrimmed (1.5") versus trimmed (1") 21ga nozzles.

C.4. Materials used

Table C.1: List of substances used.

Substance	Type	Supplier
Sporosarcina pasteurii	DSM-33, ATCC 11859	DSMZ, Germany
Silicate (mica/kaolin) platelets	RonaFlair® Satin	Merck
Alumina platelets	RonaFlair® White Sapphire	Merck
Chitosan (Powdered)	-	Shanghai Macklin Biochemical Co.,Ltd.
Chitosan (High MW)	-	Sigma Aldrich
Acetic acid 99,8%	-	Honeywell
Cellulose Nanofibers	-	Nanografi Nano Technology
Tryptone/peptone	Peptone from milk solids	Sigma Aldrich
Yeast extract	-	Sigma Aldrich/Oxoid
Ammonium chloride	-	Thermo Scientific
Calcium chloride dihydrate	-	Sigma Aldrich
Urea	-	Sigma Aldrich

Table C.2: List of equipment used. Standard equipment such as containers or metalware has not been included.

Equipment	Brand
Planetary speed mixer	SpeedMixer™ DAC 150.1 FVZ
Incubator	Fisherbrand 194L Incubator
Sputter coater	Quorum Technologies Q300T D
Scanning electron microscope	JEOL JSM-7500F
Rheometer	Thermo Scientific HAAKE Mars III
Serrated parallel plates	Thermo Scientific
Thermogravimetric analyser	PerkinElmer TGA 4000
Flexural test bench	ZwickRoell 10kN Universal Test Machine
Load cell	ZwickRoell 1kN Loadcell (Plate Mounted)
3D Printer	Ultimaker UM2+ (Custom Modifications)/Creality Ender-3 V2 (Custom Modifications)
Biosafety cabinet	Thermo Fisher Scientific MSC Advantage

This page has been intentionally left blank.

D

Raw rheology data

D.1. Variation of platelet content

D.1.1. 19.9 vol%

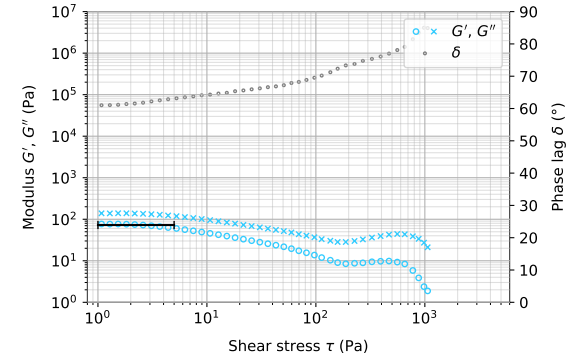

(a) Set 1

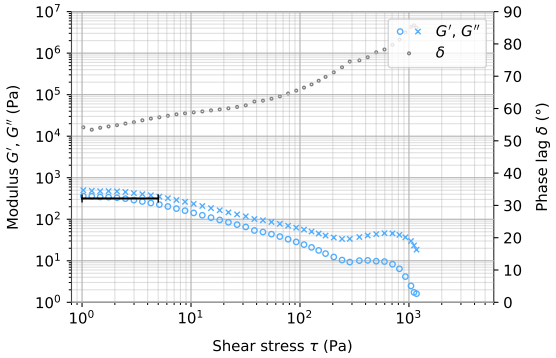

(b) Set 2

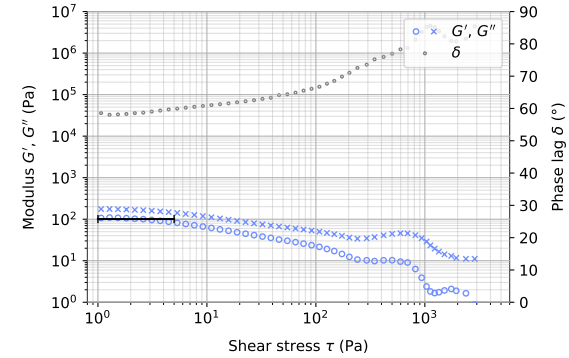

(c) Set 3

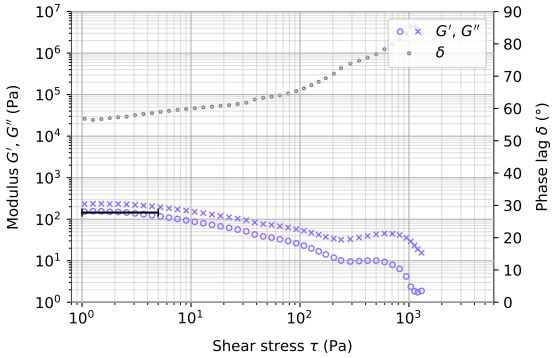

(d) Set 4

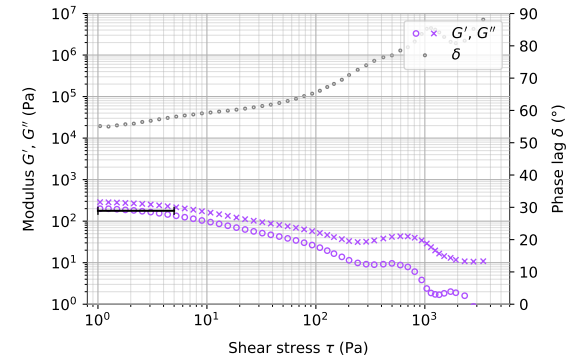

(e) Set 5

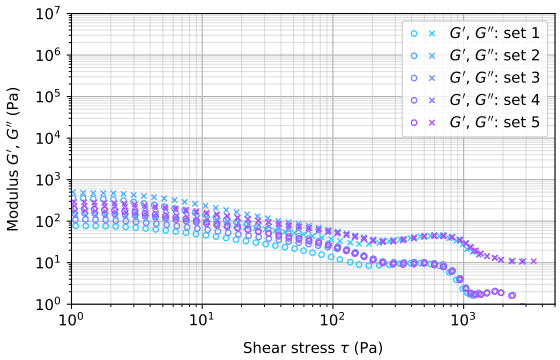

(f) Combined

Figure D.1: Repetitions of stress amplitude sweeps for 19.9 vol% (49.7 wt%) platelet content. Evaluation intervals and values for $\overline{G'}$ are denoted by the black lines.

D.1.2. 22.5 vol%

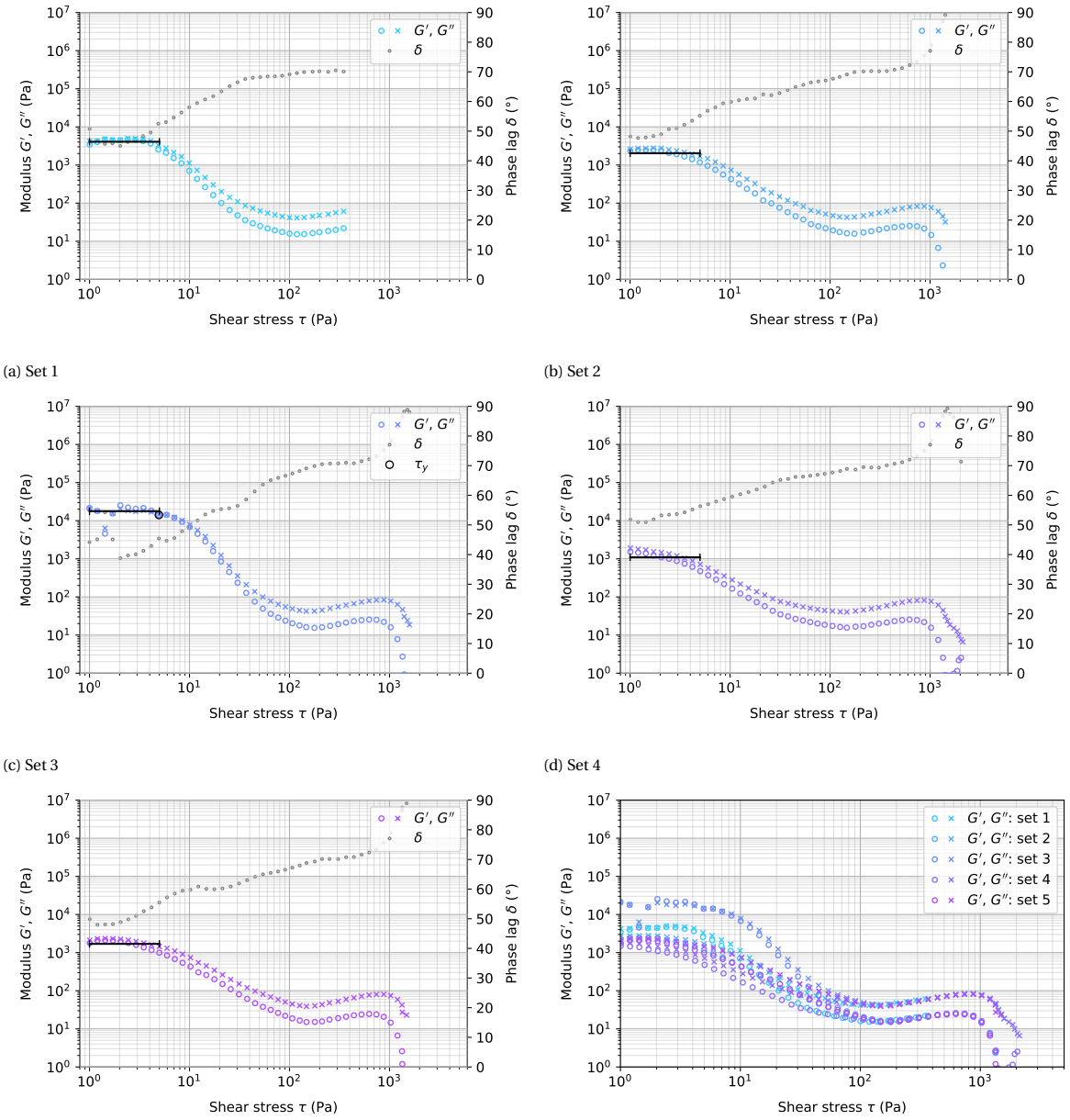

(a) Set 1

(b) Set 2

(c) Set 3

(d) Set 4

(e) Set 5

(f) Combined

Figure D.2: Repetitions of stress amplitude sweeps for 22.5 vol% (53.6 wt%) platelet content.

D.1.3. 24.9 vol%

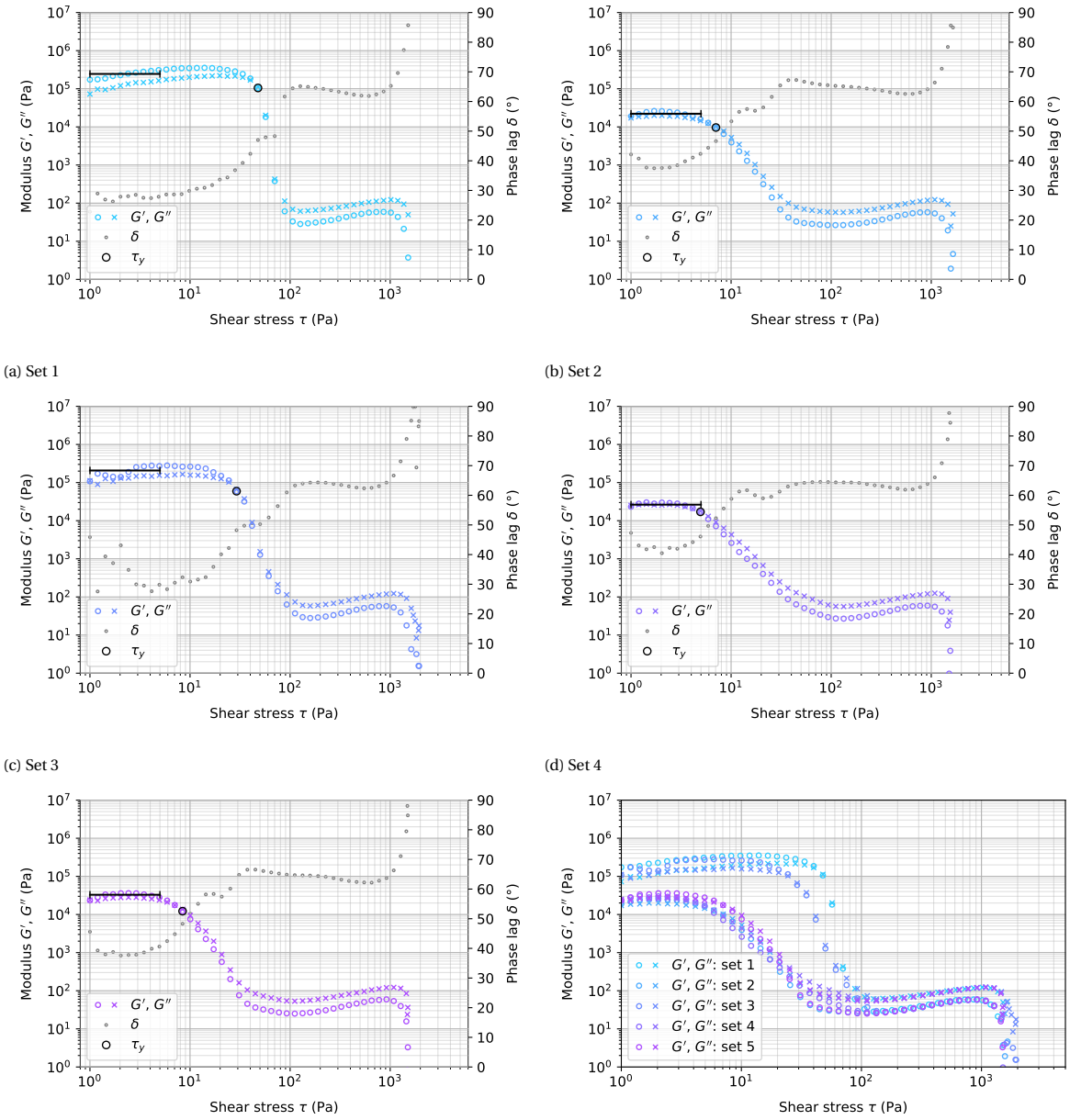

(a) Set 1

(b) Set 2

(c) Set 3

(d) Set 4

(e) Set 5

(f) Combined

Figure D.3: Repetitions of stress amplitude sweeps for 24.9 vol% (56.9 wt%) platelet content.

D.1.4. 26.0 vol%

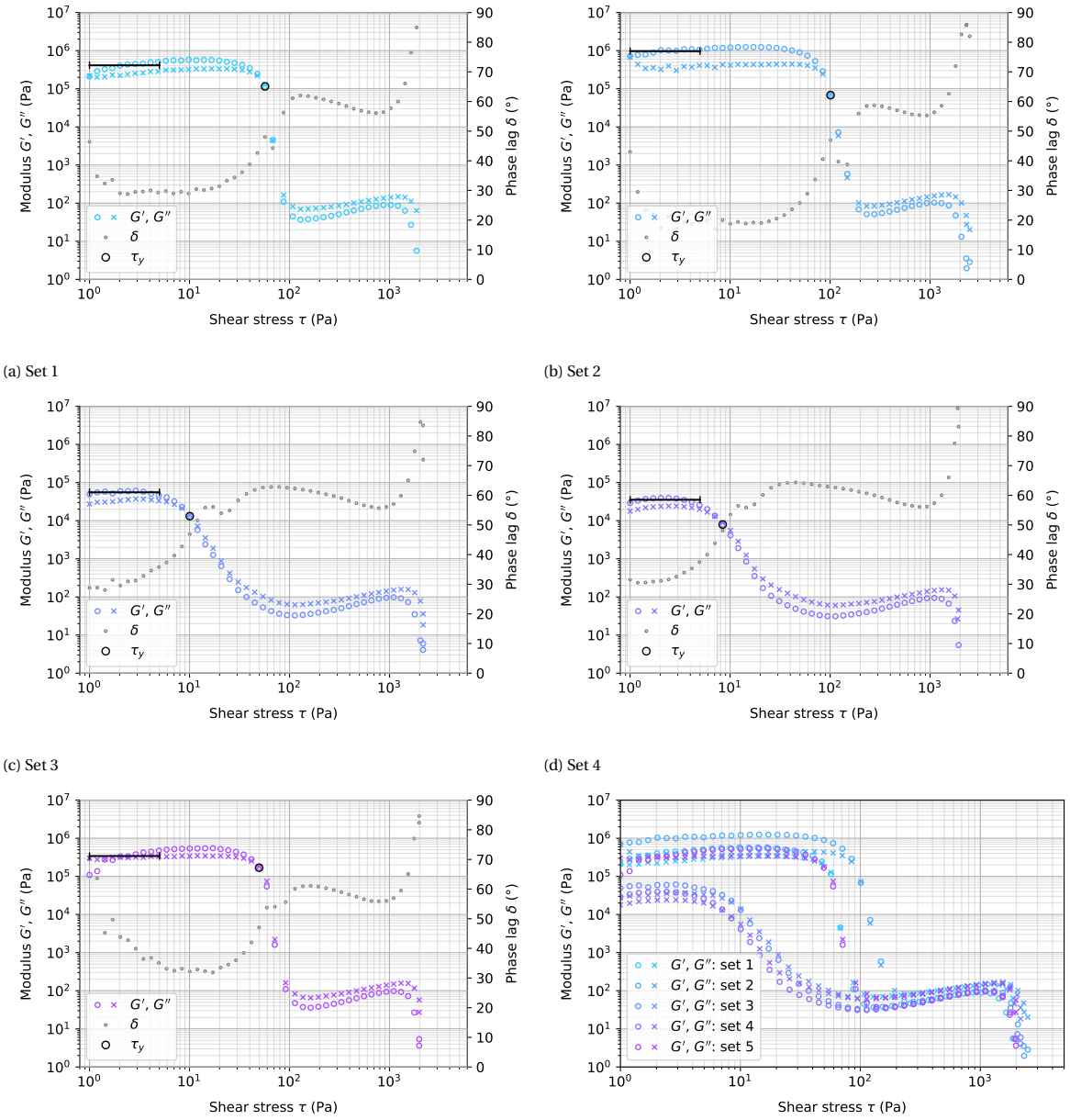

(a) Set 1

(b) Set 2

(c) Set 3

(d) Set 4

(e) Set 5

(f) Combined

Figure D.4: Repetitions of stress amplitude sweeps for 26.0 vol% (58.4 wt%) platelet content.

D.1.5. 27.1 vol%

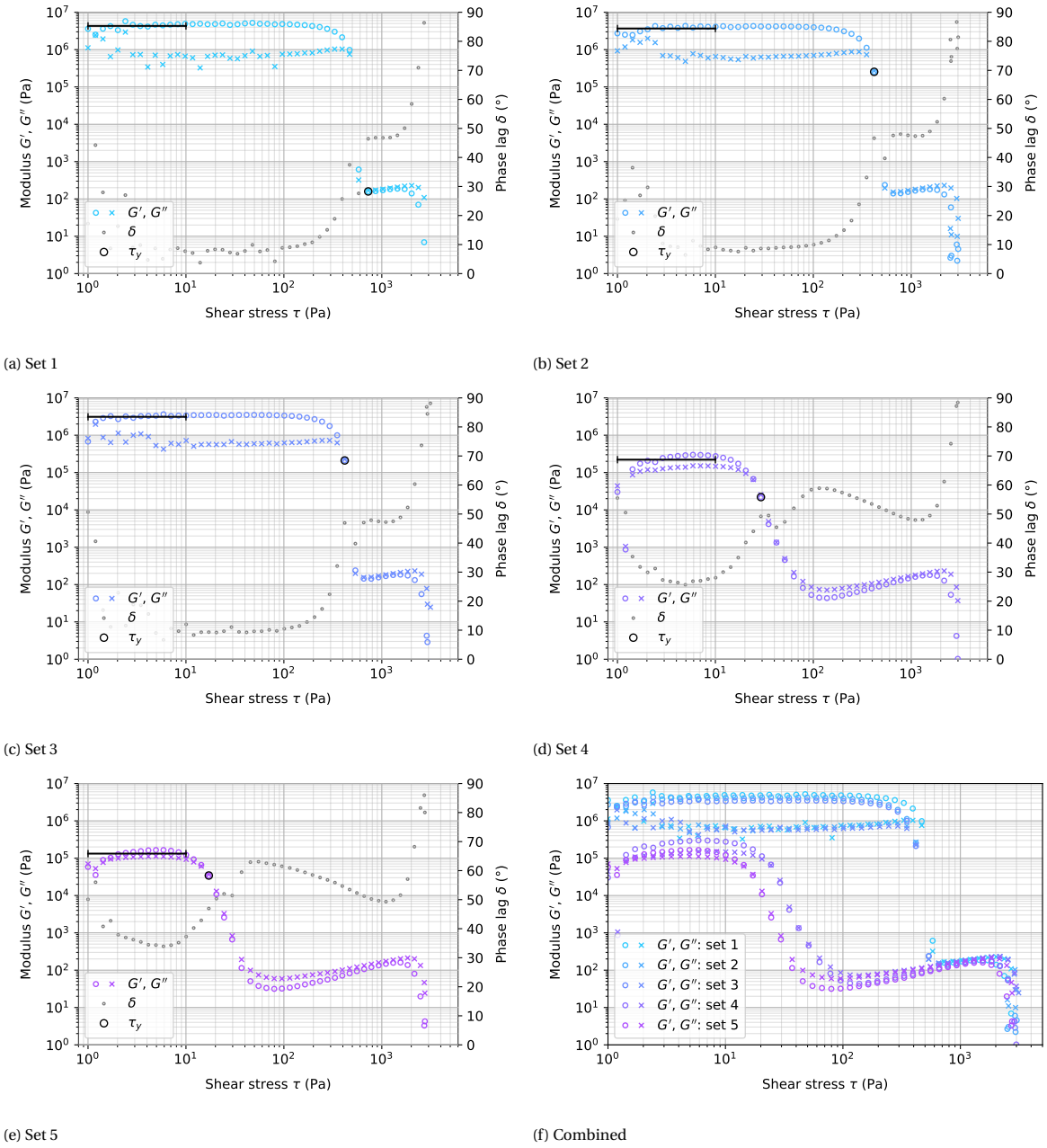

(a) Set 1

(b) Set 2

(c) Set 3

(d) Set 4

(e) Set 5

(f) Combined

Figure D.5: Repetitions of stress amplitude sweeps for 27.1 vol% (59.8 wt%) platelet content.

D.1.6. 28.2 vol%

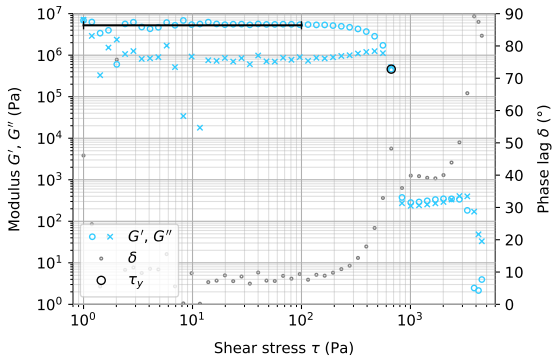

(a) Set 1

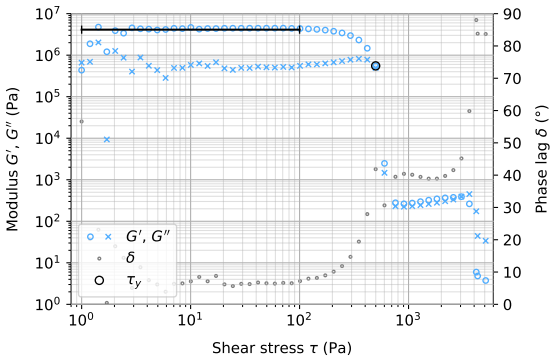

(b) Set 2

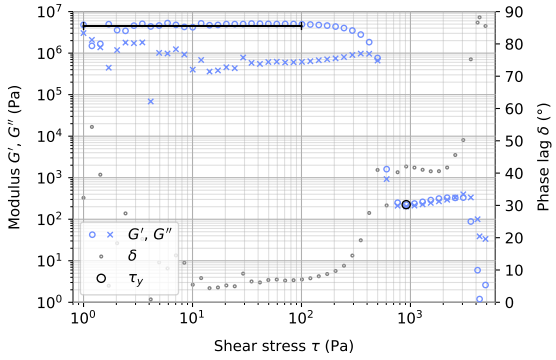

(c) Set 3

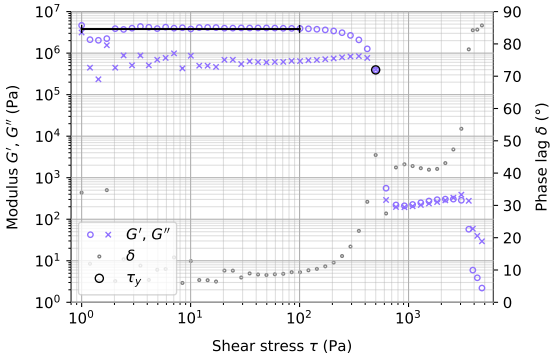

(d) Set 4

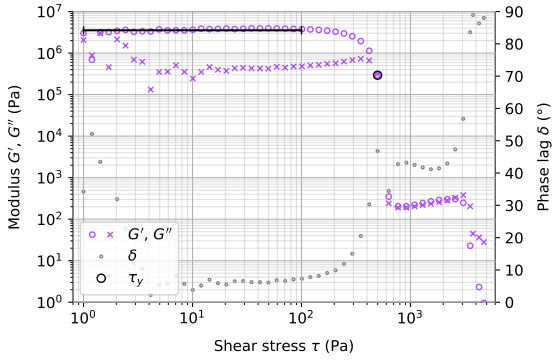

(e) Set 5

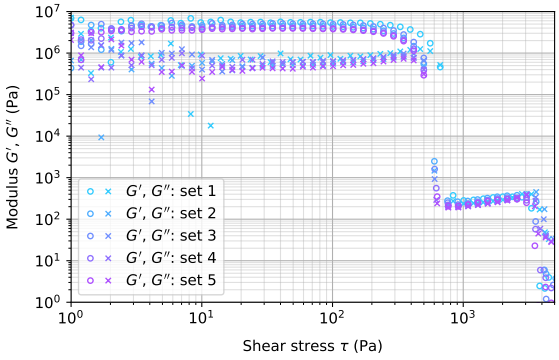

(f) Combined

Figure D.6: Repetitions of stress amplitude sweeps for 28.2 vol% (61.1 wt%) platelet content.

D.2. Variation of chitosan content

D.2.1. 1.87 vol%

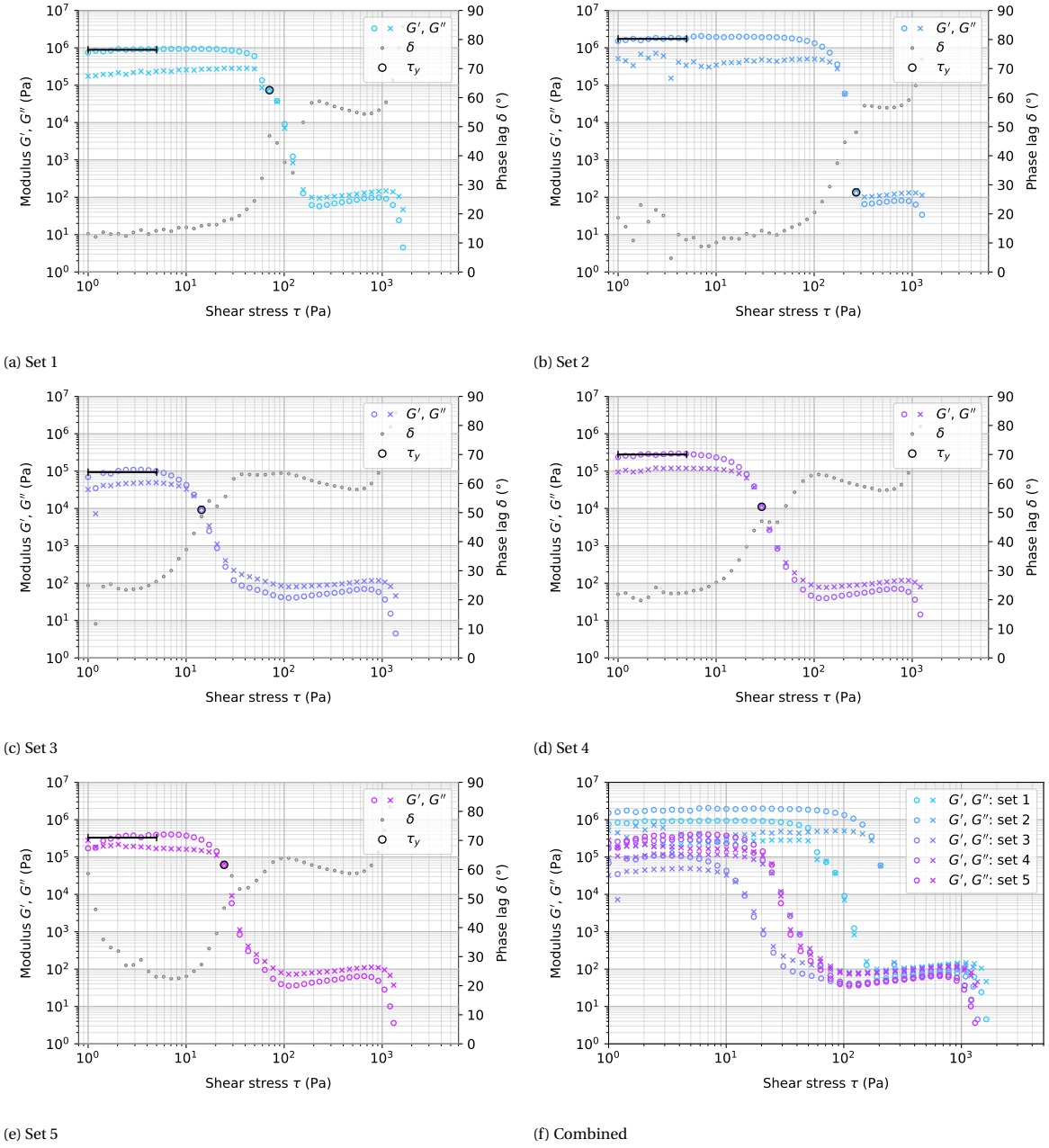

(a) Set 1

(b) Set 2

(c) Set 3

(d) Set 4

(e) Set 5

(f) Combined

Figure D.7: Repetitions of stress amplitude sweeps for 1.87 vol% (1.07 wt%) chitosan content. Platelet content is 25.9 vol%.

D.2.2. 1.93 vol%

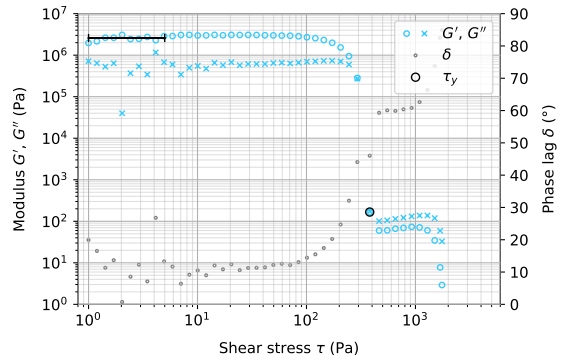

(a) Set 1

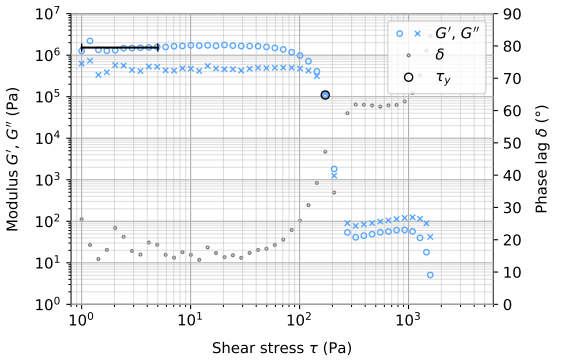

(b) Set 2

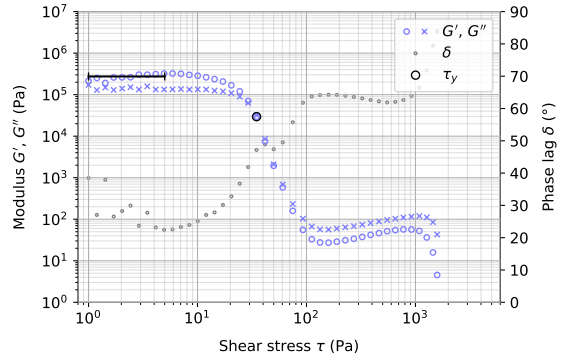

(c) Set 3

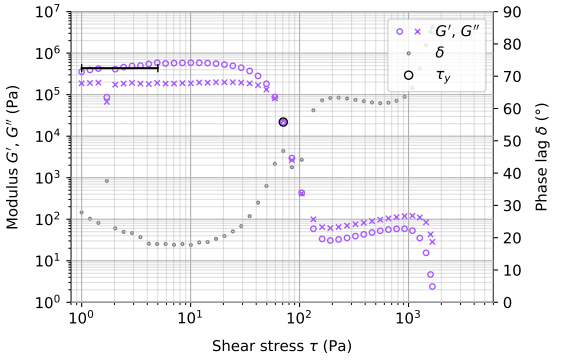

(d) Set 4

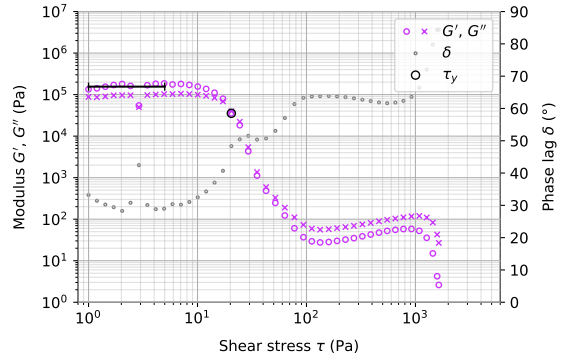

(e) Set 5

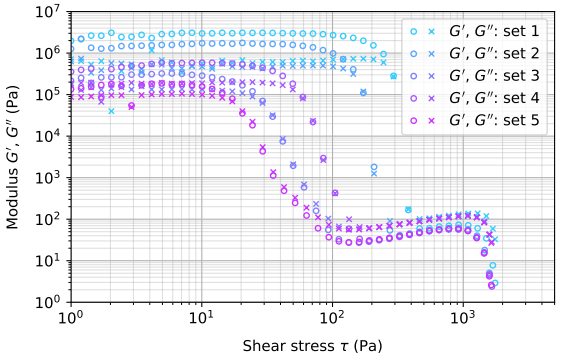

(f) Combined

Figure D.8: Repetitions of stress amplitude sweeps for 1.93 vol% chitosan content. Platelet content is 25.7 vol%.

D.2.3. 2.40 vol%

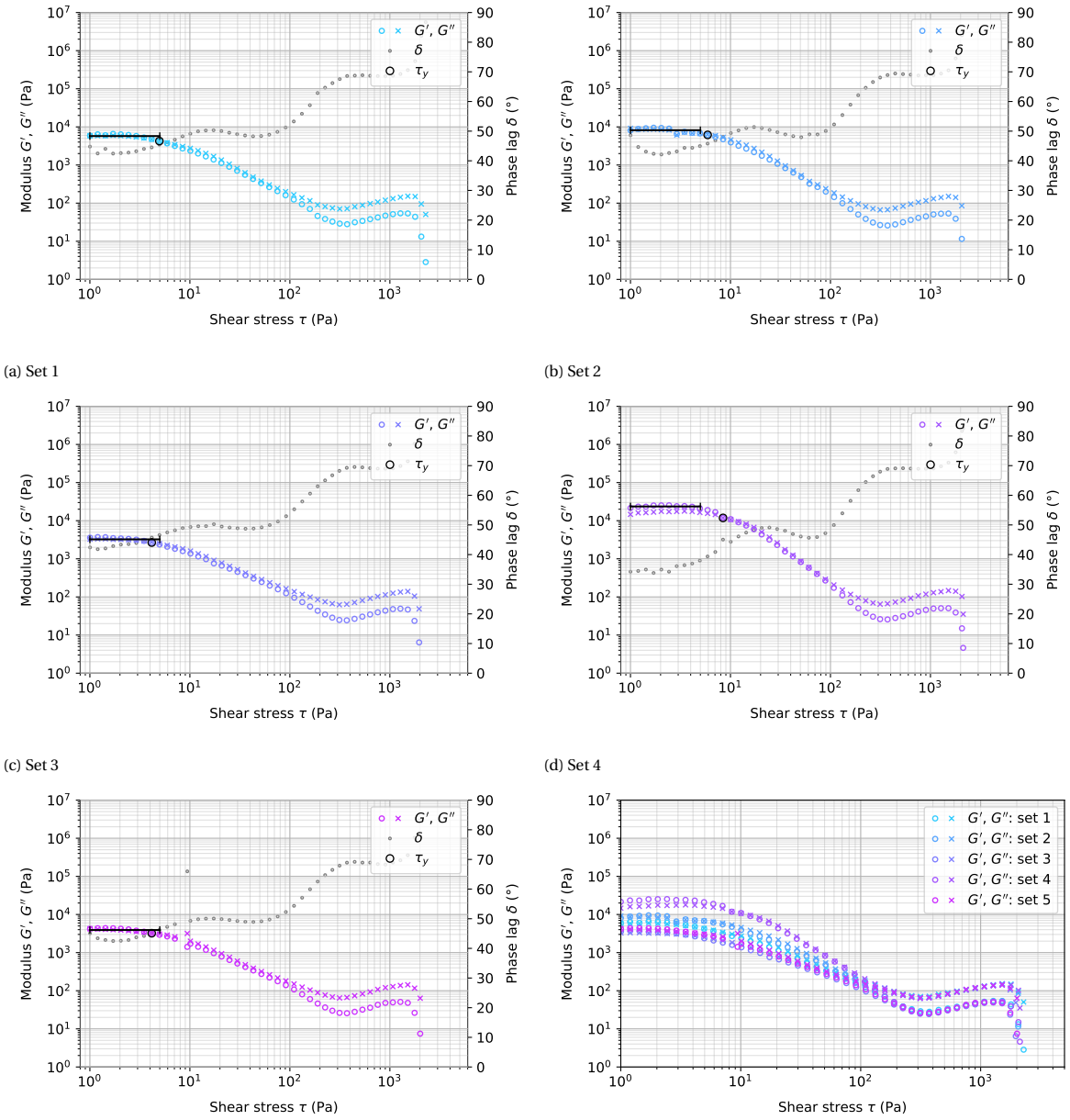

(a) Set 1

(b) Set 2

(c) Set 3

(d) Set 4

(e) Set 5

(f) Combined

Figure D.9: Repetitions of stress amplitude sweeps for 2.40 vol% chitosan content. Platelet content is 25.6 wt%.

D.2.4. 2.86 vol%

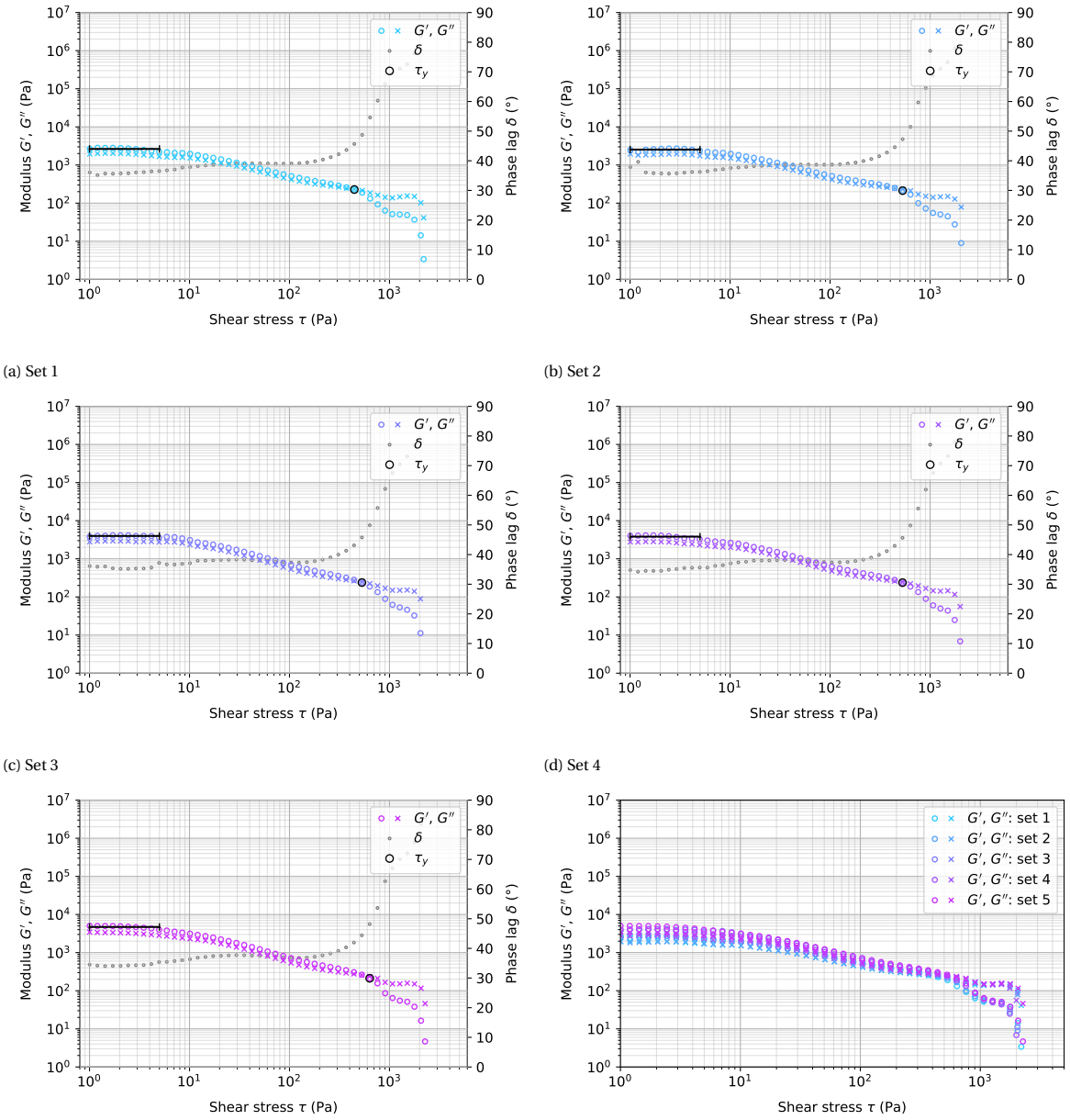

(a) Set 1

(b) Set 2

(c) Set 3

(d) Set 4

(e) Set 5

(f) Combined

Figure D.10: Repetitions of stress amplitude sweeps for 2.86 vol% chitosan content. Platelet content is 25.4 vol%.

D.2.5. 3.31 vol%

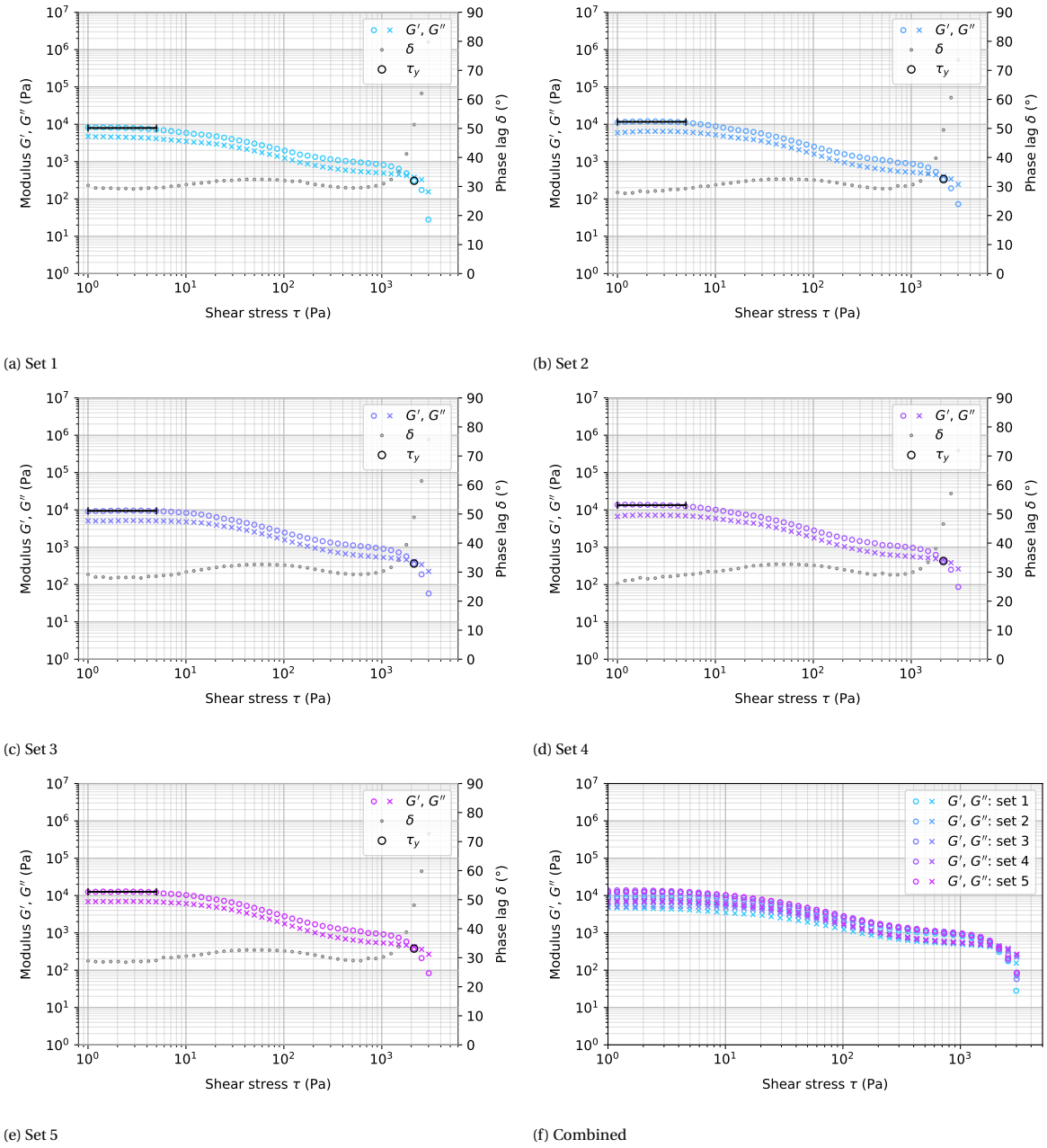

(a) Set 1

(b) Set 2

(c) Set 3

(d) Set 4

(e) Set 5

(f) Combined

Figure D.11: Repetitions of stress amplitude sweeps for 3.31 vol% chitosan content. Platelet content is 25.3 wt%.

D.3. Gap analysis

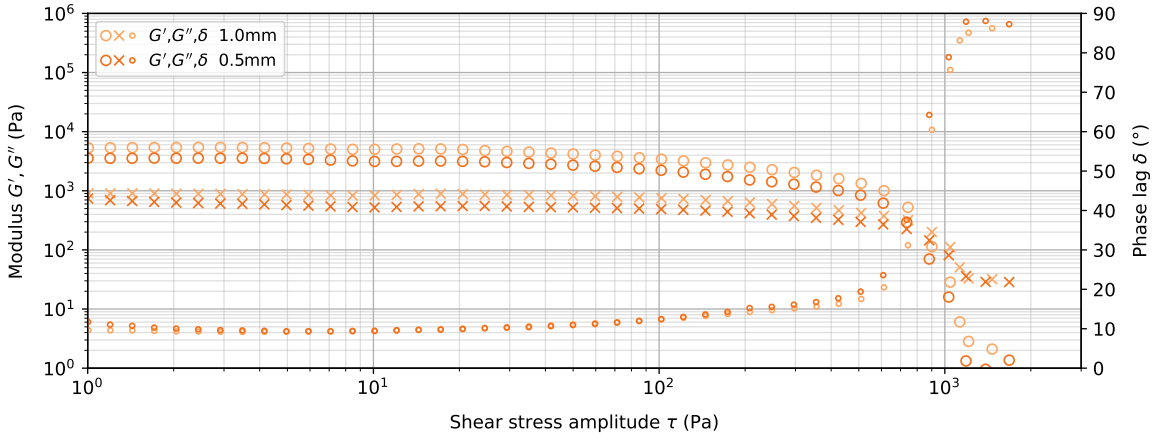

Figure D.12: Gap size analysis for amplitude sweep tests using Al_2O_3/CNF ink.

D.4. Thixotropy

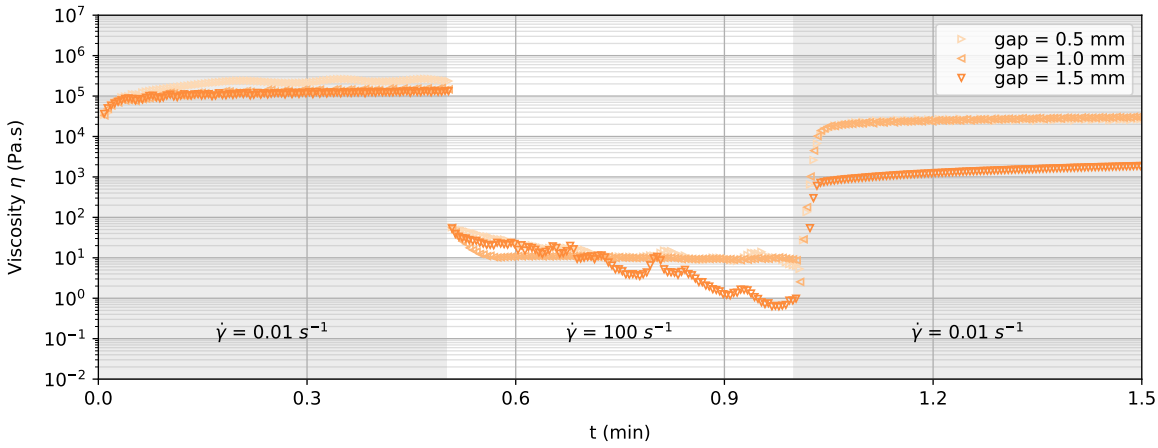

Figure D.13: 3ITT tests performed on Al_2O_3/CNF ink including a gap size variation. Note the permanent reduction in viscosity.

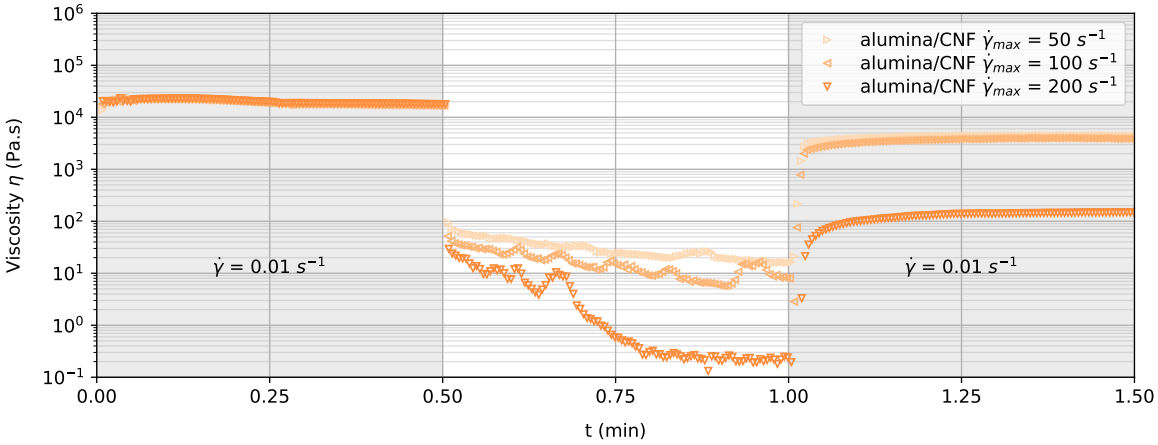

Figure D.14: 3ITT tests performed on Al_2O_3/CNF ink for varying peak flow rates. Note the permanent reduction in viscosity after high shearing.

E

Flexural testing

E.1. Force-displacement data

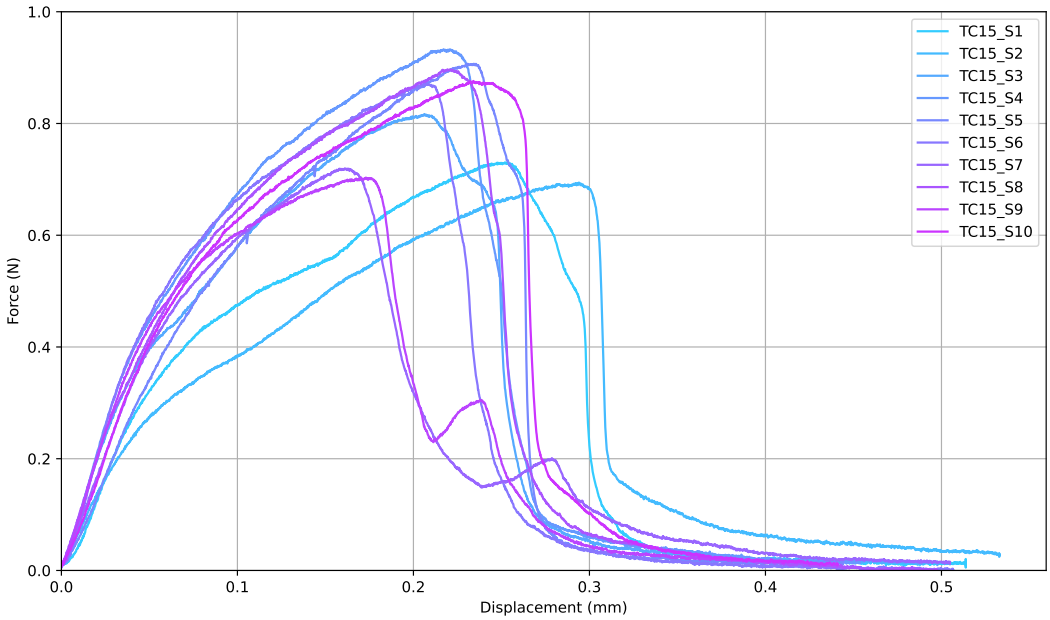

Figure E.1: Origin-adjusted force-displacement data for TC15 coupons

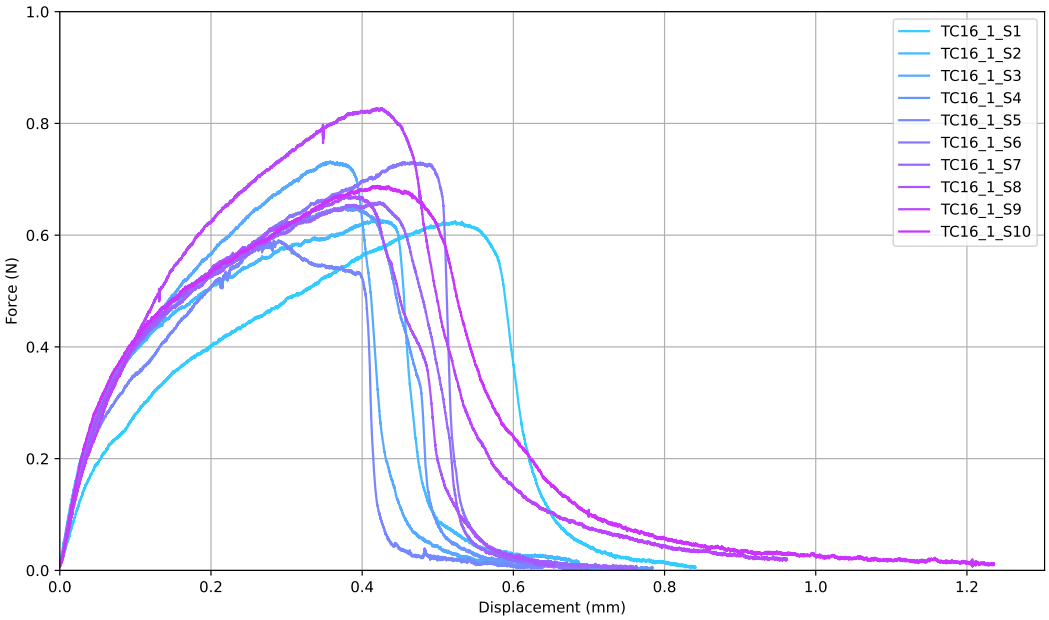

Figure E.2: Origin-adjusted force-displacement data for TC16_1 coupons

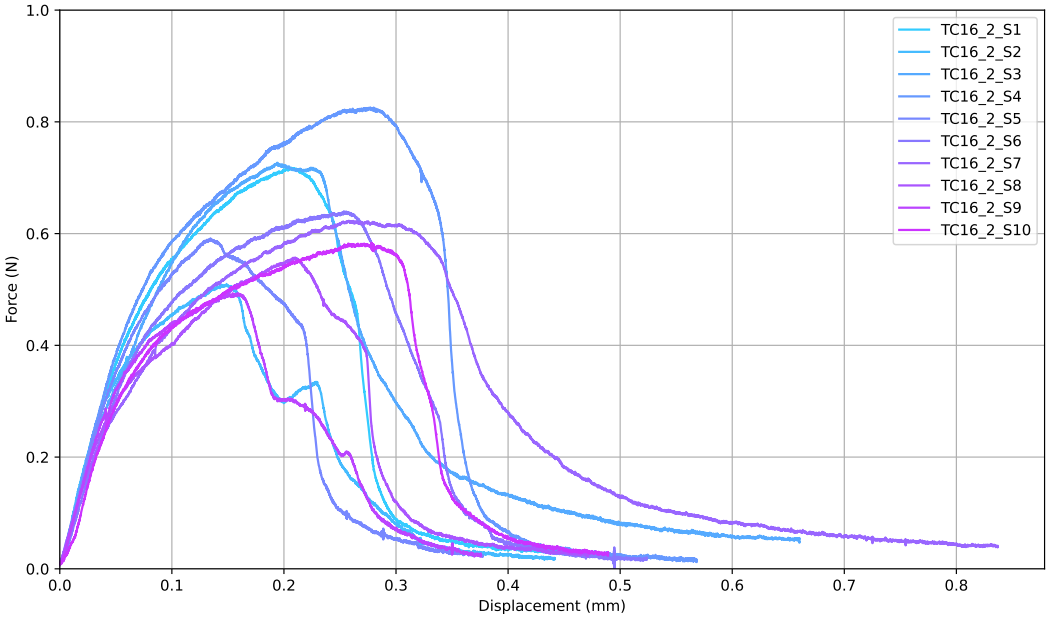

Figure E.3: Origin-adjusted force-displacement data for TC16_2 coupons

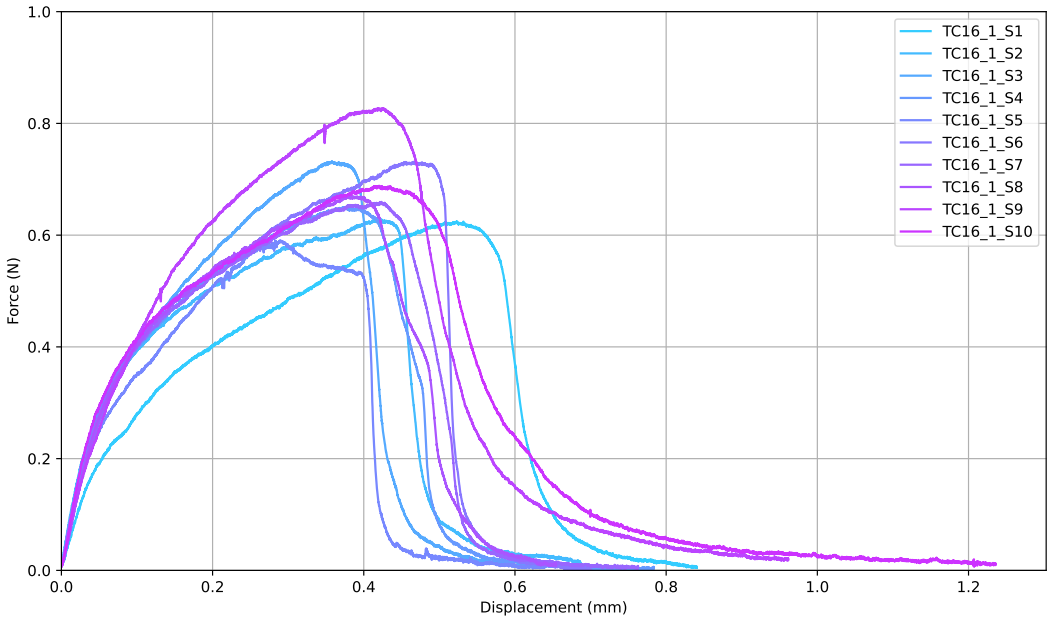

Figure E.4: Origin-adjusted force-displacement data for TC16_3 coupons

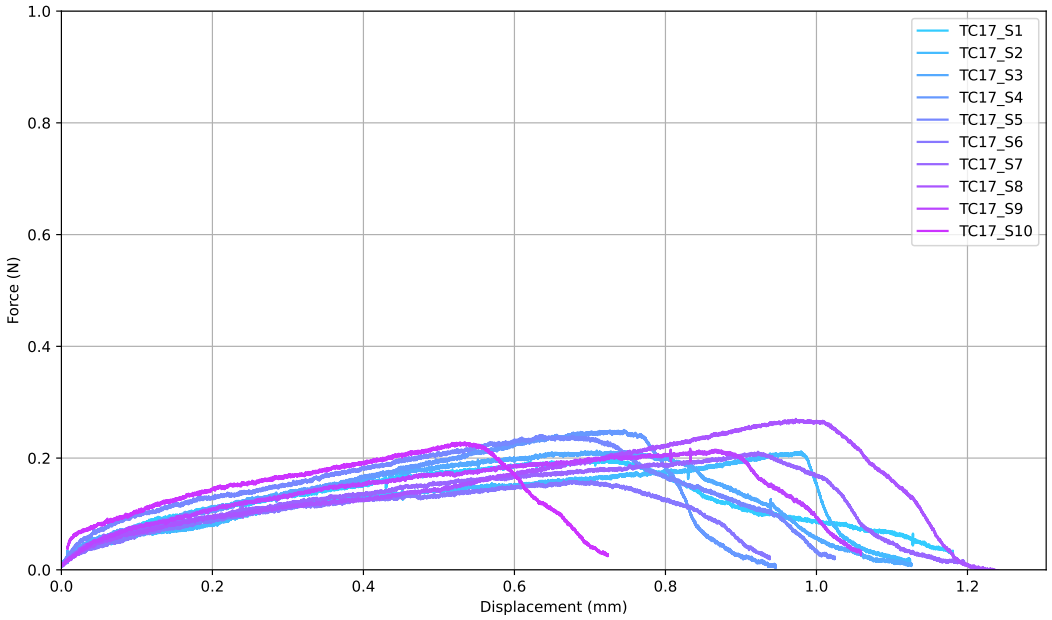

Figure E.5: Origin-adjusted force-displacement data for TC17 coupons